Design and Measurements of Millimeter-Wave MIMO Antennas

Erendira Merlos Garza

A thesis presented for the degree of
Doctor of Philosophy in Engineering

The University of Sheffield
Faculty of Engineering

Department of Electronic and Electrical Engineering
June 2024

Acknowledgements

I would like to express my gratitude to Dr. Salam Khamas, my research supervisor, for his support during my PhD journey.

I wish to thank the National Council of Humanities, Science and Technology (CONACHyT) for funding my PhD studies.

I also want to extent my special gratitude to Dr. Elizabeth J Petticrew and Sideqee Askre for their kindness and constant support with measurements at the UKVI National Millimetre Wave facility, and also to the Multidisciplinary Engineering Education (MEE) department.

Special thanks to Dr. Saeed Mohammadzadeh and Dr.Zia Ullah Khan for their mentoring and collaboration.

I wish to also thank all my colleagues in the communications research group at the University of Sheffield. Thanks for your continuous support.

Dedications

To the **soul** of my beloved mother, **Mélida**, for teaching me the importance of education, discipline, and hard work. Her wisdom remains in my heart and mind.

To the **soul** of my grandmother, **Estela**, for teaching me to have a positive attitude to life and be proud of my culture.

To the **soul** of my father, **Armando** who empirically taught me what engineering was about since I was a little girl.

To my sisters, especially to **Erika**, and my family for standing next to me and being in the toughest times unconditionally for me.

To my **friends**, who were always supporting me in so many ways, in the happiest and toughest moments of this journey: "¡Se los agradezco de todo corazón!".

"Believe in yourself, keep dreaming no matter how the circumstances or bad times are, there is always a new sunrise, a new beginning, keep fighting".

Erendira

Abstract

In response to the growing demand for connectivity among end users, the fifth generation (5G) of communication systems emerged as a promising solution, employing Multiple-Input Multiple-Output (MIMO) technology for maximizing and shielding the generation resources for the same purpose. As a fundamental part of the technology, the design of wireless channels, for this case, has been evolving each time on the improving element of its performance resulting, at the same time, in complex and expensive RF prototypes. Specifically for an end user Multi-user MIMO (MU-MIMO) environment.

This thesis contributes to the design and understanding of open loop antenna arrays and rectangular dielectric resonator antennas (RDRA) as main elements for MIMO with common Ground Plane (GP) scenarios as different design approaches for achieving high gain, wide bandwidth, and high radiation efficiencies with the simplest design methodology.

A comprehensive iterative open loop antenna array and RDRA design methodology started demonstrated, encompassing the design of 1, 2, and 4 antenna elements and examining the impact of their positioning on the MIMO system performance carried at the C-band and mmWave frequencies as part of the 5G/5GNR technology. An open loop antenna array at the mmWave with high gain and circular polarisation was initially considered, followed by an RDRA at the C-band with a similar design target as the initial case. Next, mmWave designs were considered with linear and circular polarisation. Furthermore, mutual coupling simple reduction techniques were applied to the 4 antenna element systems to determine the most adequate to preserve the single antenna capabilities for the MIMO system and maintain at the same time an inter element power reflection lower than -20 dB. The single and four RDRA element designs were fabricated and measured. The open loop antenna array demonstrated a gain of $\sim$14dBi sacrificing complexity and enhancing the coupling between MIMO elements. The proposed RDRA designs achieve simplicity and a potential antenna system overall size reduction showing at the same time a maximum gain of $\sim$7 dBi with a 4 splitted beams radiation pattern. Circular polarisation was not preserved for simulations for the mmWave case.

Acronyms

AiP	Antenna in Package
AUT	Antenna Under Test
CBCPW	Conductor Backed Coplanar Waveguide
CP	Circular Polarisation
DG	Diversity Gain
DR	Dielectric Resonator
DRA	Dielectric Resonator Antenna
DSPSL	Double Sided Parallel Strip Line Transition
DWM	Dielectric Wave Model
ECC	Envelope Correlation Coefficient
GP	Ground Plane
LHCP	Left Hand Circular Polarisation
LOS	Line Of Sight
LP	Linear Polarisation
MIMO	Multiple-Input Multiple-Output
ML	Microstrip Line
mmWave	millimetre Wave
MU-MIMO	Multiple-User MIMO
PCB	Printed Circuit Board
PEC	Perfect Electric Conductor
PMC	Perfect Magnetic Conductor
PTFE	Polytetrafluoroethylene

RDRA	Rectangular Dielectric Resonator Antenna
RHCP	Right Hand Circular Polarisation
SGH	Standard Gain Horn
SISO	Single-Input Single-Output
SMA	SubMiniature version A
SU-MIMO	Single-User MIMO
TE	Transverse Electric
TEM	Transverse Electromagnetic
TM	Transverse Magnetic
UE	User Equipment
VNA	Vector Network Analyser

Contents

List of Figures

List of Tables

- (Published) E. Merlos-Garza, R. Saad and S. K. Khamas, ”A 2x2 Dual-Band Open Loop Array With Circular Polarisation,” 2024 18th European Conference on Antennas and Propagation (EuCAP), Glasgow, United Kingdom, 2024, pp. 1-4, doi: 10.23919/EuCAP60739.2024.10501172.

- (Published) Merlos-Garza, Erendira, Zia U. Khan, and Salam K. Khamas. 2024. ”A Compact MIMO Rectangular Dielectric Resonator Antenna for Millimeter-Wave Communication” Electronics 13, no. 16: 3280. https://doi.org/10.3390/electronics13163280

Chapter 1

Introduction

1.1 5G communication systems

The past five years have seen increasing growth in the global population's internet use of around 1.3 billion users, as reported on the annual digital development forecast of the International Telecommunication Union (ITU) [1]. When quantifying these phenomena, sixty-seven per cent of the population worldwide is connected to the Internet. This fact reveals the necessity of a solid infrastructure communications network capable enough to ensure, as initial considerations, high speed, high resolution, and availability to end users. The fifth generation emerged as the one that promises a paradigm change in the network orchestration for tackling such continuous user growth. As a general technology overview, 5G considers eight key principles illustrated in Fig. 1.1.

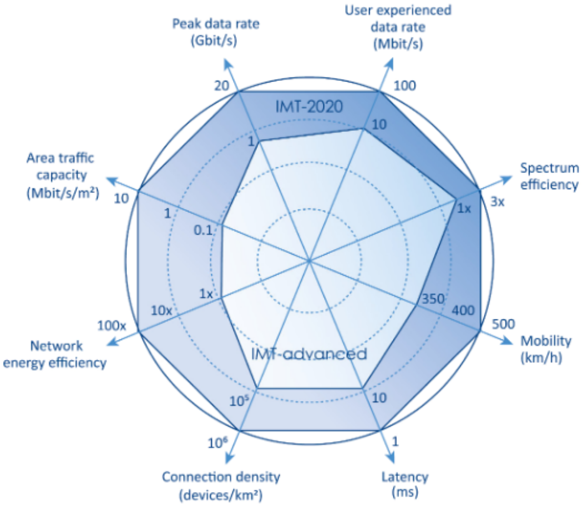

Figure 1.1: IMT-2020 ITU standard key principles [1]

A generic 5G wireless communication system link, illustrated in Fig. 1.2, is constituted by a sequence of reciprocal stages. It initially samples the input signal of interest through an Analog-to-Digital Conversion (ADC), passing through mixing, filtering, power amplification, ending with the Radio Frequency (RF) signal transmission via the antenna. The complexity and electronics accuracy will depend on the application of interest.

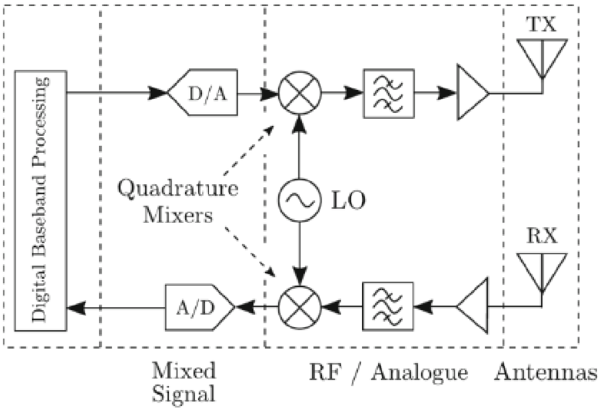

Figure 1.2: Generic mmWave communication system [2]

When delving into the intricacies of a 5G network, the layer of main interest within this work refers to the physical stage. 5G communication systems according to ITU will require to fulfill the defined 8 crucial pillars of the new generation; peak data rate, user experience data rate, spectrum efficiency, mobility, latency, connection density, network energy efficiency, area traffic capacity.
From an application perspective, the antenna element plays a critical role in ensuring effective communication at both the transmitter and receiver ends.

1.2 mmWave communications

IEEE defines the Designations for Radar-Frequency Bands which states globally the range of frequencies where specific service band will operate [3]. As the antenna communication process operates within a confined frequency band inherently linked to the antenna's dimensions. A comprehensive overview of wireless communication frequency bands for clarity is illustrated in Fig. 1.3.
The millimetre Wave (mmWave) frequency band was first investigated in the 1890's [4] by J.C.Bose evolving within the years into one of the main technologies for the fifth generation. By definition, the mmWave consists of frequencies ranging from 30 to 300 GHz.
The researcher's interest in this frequency band is due to its capability for supporting applications demanding a high speed data transmission, e.g. video distribution. Additionally,

this technology permits more dense packed communication links by providing an efficient spectrum utilization.

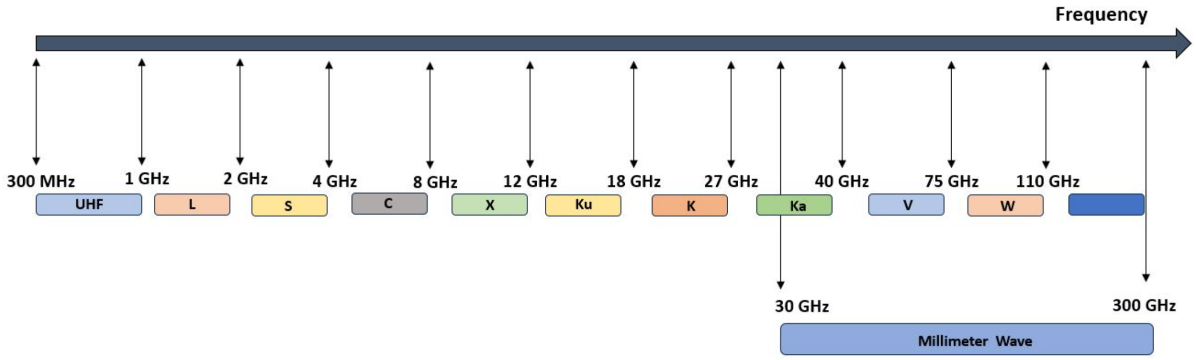

Figure 1.3: mmWave in the Spectrum band according to IEEE

1.3 MIMO communication systems overview

Since the 1920's, Beverage and Peterson [5] identified key disadvantages happening when a single user radio communication link was established. Path loss, shadowing, and multi-path fading events occurred during the transmission/reception time due to the varied environmental atmosphere. However, multi-path fading mainly affected the channel quality regarding the delivered information at the receiver. The first attempts to address this behaviour started in 1941 when a suggested second antenna was added to the system and operated by an alternating switch to provide spatial diversity to the communication link. Furthermore, in 1959, a signal processing oriented analysis was employed because of the sophistication of circuitry system levels. In 1996, Foschini [6] incorporated the conception of communications capacity in a system, in conjunction with this fact, Raleigh and Cioffi [7] contributed to this study on space-time coding, determining larger channel capacities. Alamouti [8] work focused on the transmission diversity by integrating the pre-coding analysis contributing to a predefined channel estimation. In consequence, 3G started utilising MIMO as a technology for addressing efficient data transmission, improving data transfer speeds, and providing diversity on the channel [9], evolving at the same time to 4G and then 5G on its traditional and massive cases. A clear distinction according to the number of these systems is mentioned in the literature. [10] defines a traditional MIMO as a system containing < 8 antennas, complementary, massive MIMO (mMIMO) considers the use of more than 16 elements on the system. Traditional MIMO wireless communication systems are pivotal for the successful deployment and operation of 5G applications. These systems find application in diverse domains such as in the communication of smart cities, home-based communication systems, mobile communication links, tracking of autonomous vehicles, deployment of Internet of Things (IoT) devices [11]. Another strong area is referred to the IoT-based healthcare monitoring, in body, on-body communications, [12] where MIMO architectures, with circular polarisation, ensure robust wireless communication within the challenging human body environment. Multi-satellite systems represent another application area for MIMO systems [13].

1.4 MIMO as a 5G/5GNR key antenna technology

5G/5GNR technology considers MIMO as a fundamental technology for achieving high data rates with improved signal quality in a context where some of the main customer applications are e.g. user-centric computing, smart transportation, multimedia streaming, telemedicine. [14]. MIMO technology is characterized by bringing diversity, spatial multiplexing, and beamforming enhancement to the wireless channel. It is classified into 4 principal architectures: Single-Input Single-Output (SISO), Single-Input Multiple-Output (SIMO), Multiple-Input Single-Output (MISO), and the second one as a Multiple-Input to Multiple-Output architecture Multiple-Input Single-Output (MIMO) [15]. MIMO, architecture of main interest through this thesis, gathers several Single-Input Single-Output (SISO) channels in a single architecture where M, the transmitter antennas, send the data streams to each one of the N receiver antennas on the system, assuming that the MIMO total size is given by $M \times N$ elements. The main benefit of the architecture resides in a multiplexed gain, and a linear increase in capacity per pair of antennas. MIMO architecture is illustrated in Fig. 1.4 [16].

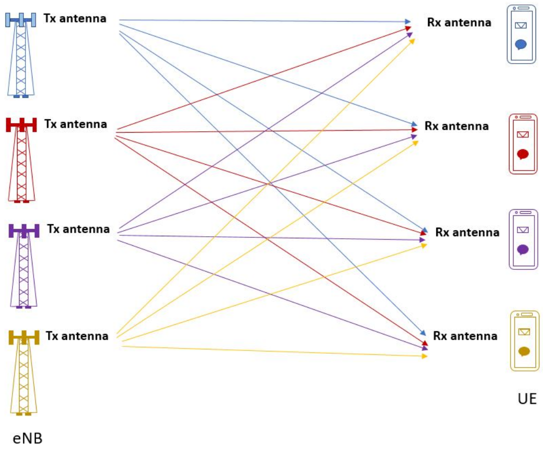

Figure 1.4: MIMO topology

Moving on to MIMO link applications at the user level, it is relevant to mention that the technology can operate either as a Single-User MIMO (SU-MIMO) or a Multiple-User

MIMO (MU-MIMO). SU-MIMO contemplates assigning all MIMO layers to the same user resulting in a higher theoretical peak data rate for the User Equipment (UE). In contrast, Multiple-User MIMO (MU-MIMO) can provide all MIMO layers to different UE within the architecture. It results in a higher throughput per cell/sector than Single-User MIMO (SU-MIMO) [17]. It is relevant to mention that a cell can switch between its modes dynamically.

After referring to the basic operating modes of MIMO, Table. 1.1 summarises the operating standards for the defined frequency range of the technology of interest.

Table 1.1: 5G/5GNR Frequency ranges [18]

Band name	Frequency band	NR bands	Channel bandwidth (MHz)
FR1	450 MHz–7.125 GHz	n77(3.3–4.2 GHz) n78 (3.3–3.8 GHz) n79 (4.4–5.0 GHz)	5, 10, 15,20, 25, 30, 40, 50, 60, 80, 90, 100
FR2	24.25 GHz–52.6 GHz	n257 (26.5–29.5 GHz) n258 (24.25–27.5 GHz) n260 (37.0–40.0 GHz) n261 (27.5–28.35 GHz)	50, 100,200, 400

1.5 Project overview

1.5.1 Problem definition

Despite the growing interest in RDRA MIMO systems, a comprehensive investigation into the impact of circular polarisation on their performance remains limited. Additionally, existing designs in the literature exhibit a high design and fabrication complexity.

This research investigates the feasibility of achieving high gain, circular polarization, and wide bandwidth in millimetre-wave multiple-input multiple-output (MIMO) through a couple of potential antenna architecture with simple, cost-effective design techniques. Moreover, the presence of a simultaneous petal beam splitting based on existing antenna design techniques.

1.5.2 Thesis aims and objectives

The main objectives that this thesis is designed to achieve are:

1. Design, and simulate a single microstrip antenna array with high gain, CP at mmWave. Iterate the design, creating a MIMO system with 2 and 4 elements, respectively.
2. Design, and simulate a single RDRA antenna with high gain at C-band and mmWave. Iterate the design, creating a MIMO system with 2 and 4 elements respectively.
3. Design, and simulate a single RDRA antenna design with high gain and CP at mmWave. Iterate the design, creating a MIMO system with 2 and 4 elements, respectively.
4. Investigate the MIMO antenna system by positioning as an isolation technique for the created designs.
5. Integrate and investigate slot etched on the Ground Plane (GP) to preserve CP and reduce mutual coupling at C-band and mmWave.
6. Investigate MIMO antenna systems by positioning as a natural controller for beam steering at C-band, mmWave for the 4 element designs.
7. Assemble and measure the designed prototypes.

An open-loop microstrip antenna array was initially selected for its design simplicity. This configuration offers a high gain, wide impedance bandwidth, and a high circular polarization axial ratio while maintaining a relatively simple geometry, particularly advantageous at mmWave frequencies. Moreover, there was no need for any additional assembling to achieve the antenna matching. Next, to address the non-favorable results encountered with MIMO simulations, an alternative antenna structure was proposed. An RDRA was selected due to its design simplicity to achieve high gain, high efficiency, and capability for achieving wide bandwidths, at C-band frequencies. Subsequently, similar structures either with linear or circular polarisations on the RDRA were proposed and investigated at the mmWave frequencies. Fig.1.5 summarises the general design methodology throughout the present thesis.

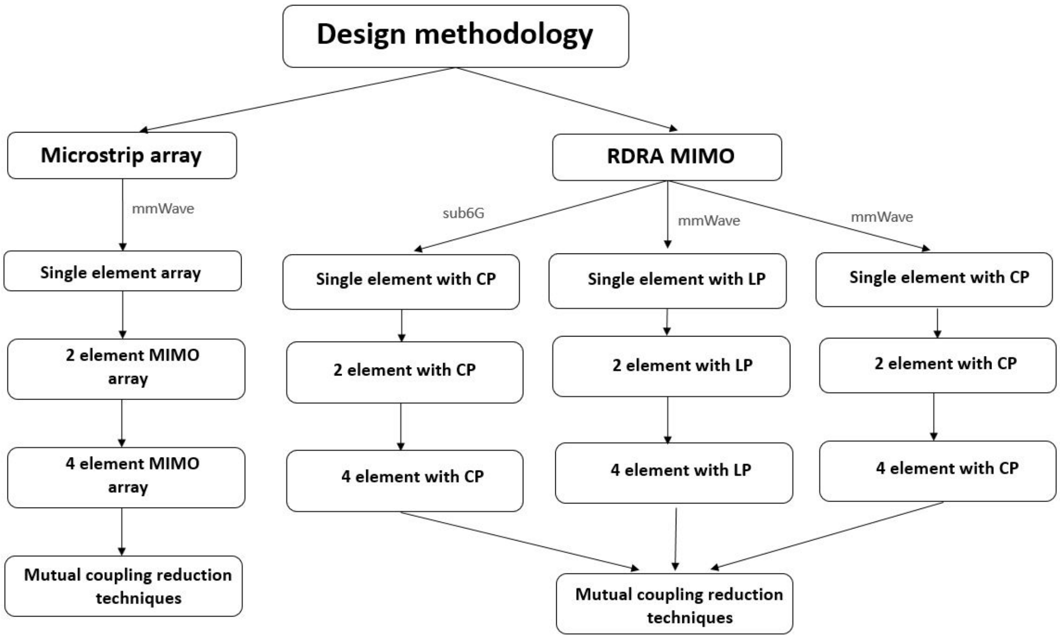

Figure 1.5: Thesis design methodology overview based on the objectives

1.5.3 Novelty of the work

The novelty of the present work relies on proposing four different prototypes with a compact design, smaller than $2\lambda_0$. A minimum gain of not smaller than 5 dBi, an impedance bandwidth of at least 6%, and a <3dB axial ratio for each individual and MIMO design. Moreover, simple combined techniques such as antenna element staggering and slot etching on the common Ground Plane layer between elements of the system were employed for each case resulting in an important reflection coefficient smaller than <-20 dB translated into a mutual coupling reduction. This thesis proposes a novel beamforming technique for MIMO antennas based on element staggering, creating four main radiation petals at the four antenna radiation directions. Simultaneous testing and analysis of these patterns reveal a new testing scenario for this type of system at the mmWave spectrum when referring to the existing literature. The aforementioned contributions were successfully evaluated and reported in accordance with the MIMO metrics ECC and DG.

1.5.4 Thesis structure

The present thesis consists of six chapters structured as:

Chapter 1 sets the scene by introducing the reader to the topic, providing the needed literature review, setting the research question, explaining the project contribution, and defining the thesis aims and objectives.

Chapter 2 presents the design, investigation, manufacture, and measurements of a microstrip open loop antenna array as the main antenna element for the MIMO system working at mmWave with CP. Furthermore, it presents the simulated MIMO antenna array design with a progressive iteration for 2 and the manufacture and measurement of the 4 MIMO elements system.

Chapter 3 presents the design, investigation, manufacture, and measurements of a Rectangular Dielectric Resonator Antenna (RDRA) as the main antenna element for the MIMO system working at C-band with CP. It also presents the simulated MIMO antenna design with a progressive iteration for 2 elements and the manufacturing and measurements of the 4 elements MIMO system.

Chapter 4 presents the design, investigation, manufacture, and measurements of a RDRA as the main antenna element for the MIMO system working at mmWave. Additionally, it presents the simulated MIMO antenna design with a progressive iteration for 2 elements and the manufacture and measurement of 4 elements MIMO system.

Chapter 5 presents the design, investigation, manufacture, and measurements of a RDRA as the main antenna element for the MIMO system working at mmWave with CP. Moreover, it presents the simulated MIMO antenna design with a progressive iteration for 2 manufactured and measured elements and the 4 MIMO elements system.

Chapter 6 Presents conclusions and future work.

Chapter 2

Theoretical background

This thesis is centered on designing one of the key elements of a wireless communication system, antennas. Some key theoretical antenna conceptions are presented throughout this chapter to provide an adequate understanding of the following chapters. Furthermore, essential antenna parameters for MIMO systems are presented for a comprehensive understanding of the prototypes.

2.1 Antenna polarisations

When locating the transition stage of the most simple case of an antenna, exactly where the input waveguide is converted into a wireless signal, it is imperative to contemplate the physical propagation of these waves. The literature presents different types of propagation: linear, circular, and elliptical [19]. The polarisations of our interest for this investigation are Linear polarisation (LP) and Circular polarisation (CP).

Antenna polarisation is determined by the propagation behaviour of the Electric field, E-field, and must be considered in the far-field region of the device. Hence, linear polarisation is constituted by E_θ and E_ϕ components, which define the propagated wave in a linear direction started the propagating wave. E_θ vector should be orthogonal to E_ϕ when propagating linearly from a transmitter to a receiver as shown in Fig. 2.1.

When referring to circular polarisation, the antenna radiation pattern can be described as E which can be decomposed in vectors E_R and E_L refer to the right and left components within the polarisation ellipse shown in Fig. 2.2. The decomposition of the Electric field elements constitute a circular propagation throughout time as illustrated in Fig. 2.3. The polarization ellipse is a fundamental theoretical parameter for determining the propagation behaviour of the electromagnetic waves which are propagated form a transmitter. The Axial Ratio (AR), defined as the ratio of the minor to the major axis of the polarisation ellipse, determines the polarisation state. An AR less than 3 dB indicates the presence of circular

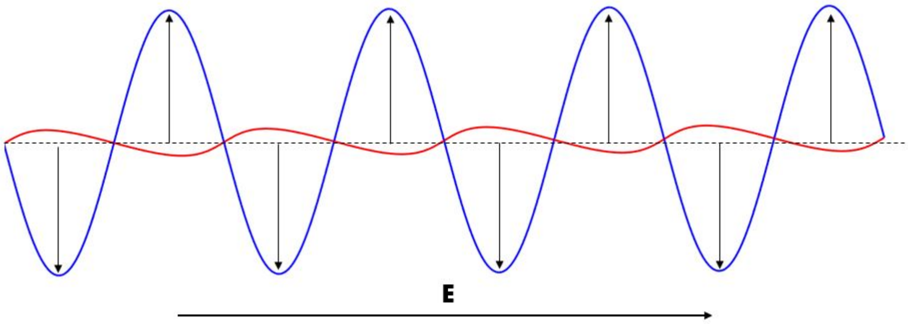

Figure 2.1: [20] Linear polarisation propagation principle

polarisation of the E-field.

A couple of circular polarisation propagation directions are defined. The first one is named Right Hand Circular Polarisation (RHCP) which means the electric field is rotating as shown in Fig. 2.3a. The second one named Left Hand Circular Polarisation (LHCP) works in the opposite direction as illustrated in Fig.2.3b.

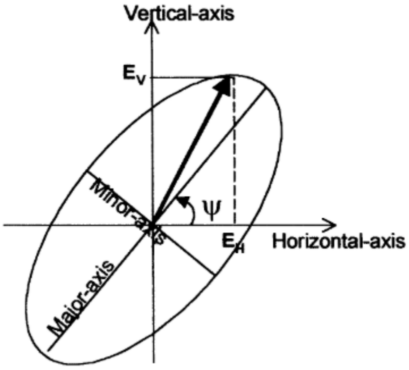

Figure 2.2: [20] Polarisation ellipse

Assuming the most straightforward experimental scan for the E-field and the H-field components,axial ratio can be determined as the following:

$$E_H = E_{H_r} + jE_{H_i} \tag{2.1}$$

where
H_A is the horizontal amplitude
V_A is the vertical amplitude

$E_{H_r} = H_A cos(Hp)$
$E_{H_r} = H_A sin(Hp)$

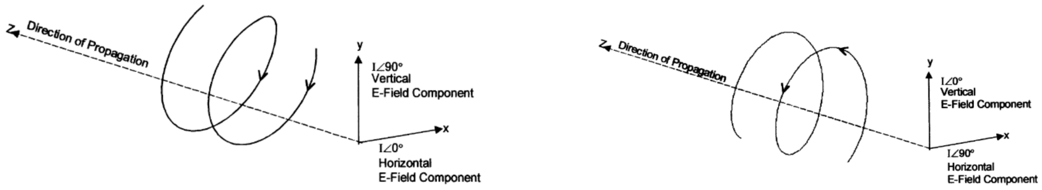

(a) RHCP (b) LHCP

Figure 2.3: [20] Types of circular polarisation

For determining the vertical components of the antenna:

$$E_V = E_{V_r} + jE_{V_i} \tag{2.2}$$

$E_{V_r} = V_A cos(Vp)$
$E_{V_r} = V_A sin(Vp)$
The E_{RHCP} and E_{LHCP} are defined as:

$$E_{RHCP} = \frac{1}{\sqrt{2}}(E_H + jE_V) \tag{2.3}$$

$$E_{LHCP} = \frac{1}{\sqrt{2}}(E_H - jE_V) \tag{2.4}$$

After substituting:

$$E_{LHCP} = \frac{1}{\sqrt{2}}[H_A cos(H_P) + V_A sin(V_P)] + j[H_A sin(H_P) - V_A cos(V_P)] \tag{2.5}$$

$$E_{RHCP} = \frac{1}{\sqrt{2}}[H_A cos(H_P) - V_A sin(V_P)] + j[H_A sin(H_P) + V_A cos(V_P)] \tag{2.6}$$

The axial ratio can be calculated with the E_{RHCP} and E_{LHCP} components in linear scale respectively as:

$$AR = 20log_{10}\frac{|E_R| + |E_L|}{|E_R| - |E_L|} \tag{2.7}$$

2.2 Microstrip planar antennas

Microstrip planar antennas can be designed in a variety of geometrical shapes, implying the enhancement of dedicated features regarding each case of study. A wide variety of geometrical radiators constitutes this type of antenna. Loop antennas, which are the antennas of interest for this case, invented by Hertz [21] were initially researched because of their simplicity at low frequencies and for Linear Polarisation (LP) scenarios, which were later modified for becoming stronger candidates for achieving CP by adding an inner gap through the radiator. Some of the most common available shapes for loop antennas are circular, square, triangular, rectangular, and elliptical. In the presented work, the antenna of interest is the circular open loop antenna as illustrated in Fig. 2.4.

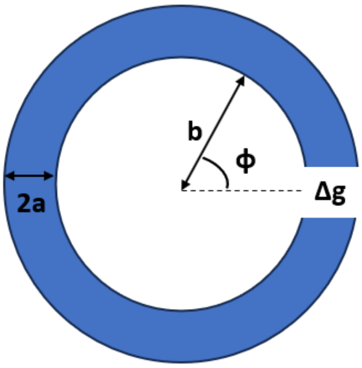

Figure 2.4: Geometry of the open loop

Open loop antennas are classified according to their electrical size. The open loop electrical length is a key consideration for determining circular polarization, as explained in reference [22]. Their impedance is theoretically defined in [23] as:

$$Z = R + jX \tag{2.8}$$

where
R refers to the resistance
X refers to the reactance

For obtaining the open loop resistance, the electrical size is calculated as:

$$\beta = \frac{2\pi b}{\lambda} \tag{2.9}$$

where
b defines the loop radius
λ defines the antenna wavelength

By referring to the estimation of the resistance and reactance with respect to its electrical size in [23], the antenna impedance can be estimated.

Additionally, the thickness parameter is determined as:

$$\Omega = 2 \cdot ln\ 2\pi \frac{b}{a} \tag{2.10}$$

where

a refers to the thickness of the loop.

b refers to the radius.

Open loop antennas are potential candidates for achieving circular polarisation with considerably simple changes on the original design. A gap within the open loop is the technique considered for this case. According to [24], the disruption of the travelling wave propagation when encountering the added gap will generate a change of phase within the antenna creating as a result CP.

2.2.1 Microstrip antenna arrays

After considering the open loop single radiators, it is possible to have an overview of the case of multiple antennas working with a feeding network, named as arrays. They emerged as a design solution for taking advantage of constructive interference through the propagation of waves, enhancing the radiating structure's overall gain. By assuming the simplest scenario of multiple antennas receiving at the same time, considering an equidistant location Fig. 2.5 illustrates the scenario extracted from [19].

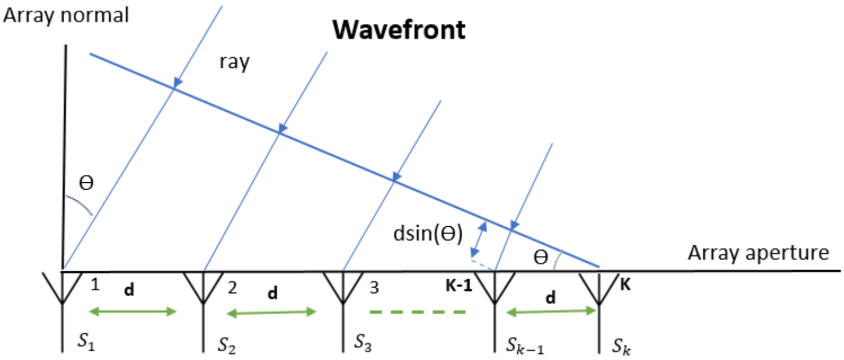

Figure 2.5: Linear array antenna

K represents the number of radiators in the array

d the distance between antennas

θ represents the incident angle of the plane wave.

The starting point reference for the mathematical analysis is defined on the receiver antenna side. An equidistant position in addition to the antenna reciprocity is assumed. The array's feeding network is a summing network that will consider the components involved in the reception. Assuming an existing phase during reception

$$\Phi_i = k_0(K-i)dsin(\theta) \text{ for } i = 1,2,..,K \tag{2.11}$$

where ***dsin(θ)*** is the travelling distance of the wave.
Φ_i is derived the phase signal equation after suppressing e^{jwt} from:

$$\Phi_i' = wt \pm kl \tag{2.12}$$

λ_0, the wavelength in free space, is given by

$$k_0 = \frac{2\pi}{\lambda_0} \tag{2.13}$$

The complex signals received by the existing elements $S_i(\theta)$ is expressed as:

$$S_i(\theta) = S_e(\theta)a_i e^{jk_0(K-i)dsin(\theta)} \text{ for } i = 1,2,...,K, \; a_i = 1 \text{ for } i = 1,2,..,K. \tag{2.14}$$

a_i represents the received amplitude by the *ith* element. $S_e(\theta)$ represents the complex radiation pattern of one individual radiator. All amplitudes are assumed to be equal and normalized at one point, defined as a uniform aperture distribution. $S_i(\theta)$ will denote the complex signals received by the elements of the array antenna.

Considering the combination of the received signals without additional phase differences, the total received signal $S(\theta)$ can be expressed as:

$$S(\theta) = \sum_{i=1}^{K} S_i(\theta) = S_e(\theta)\sum_{i=1}^{K} e^{(jk_0(K-i)dsin(\theta))} \tag{2.15}$$

The element factor $S_e(\theta)$ is defined as :

$$S(\theta) = S_e(\theta)S_a(\theta) \tag{2.16}$$

Substituting Eq. 2.11:

$$S_a(\theta) = \sum_{i=1}^{K} e^{(jk_0(K-i)dsin(\theta))} \tag{2.17}$$

where $S_a(\theta)$ refers to the radiation pattern array factor of an array of K isotropic radiators.

2.3 Dielectric Resonator Antennas

The Dielectric Resonators (RDRs) were theoretically demonstrated by R.D. Richtmyer in 1939 [25] and formally studied as a fundamental part of a novel antenna design in 1983 [26]. Long. McAllister and Shen [27] investigated and published the first DRA design of its kind, consisting of a cylindrical shape with a probe feeding mechanism, thus marking the beginning of a new research era for DRA's. DRA's are considered as potential solutions for enhancing antenna characteristics due to their capability for delivering wide bandwidths and high radiation efficiencies. Many of the most common dielectric shapes that can be found within the literature, working fundamentally as radiators, are cylindrical, rectangular, triangular, spherical, and hemispherical, among others which are illustrated in Fig. 2.6

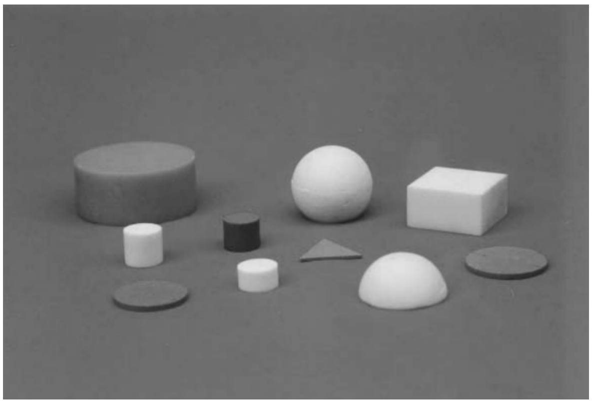

Figure 2.6: [28] Examples of Dielectric resonators.

2.3.1 Rectangular Dielectric Resonators

The RDR's were studied as antenna elements because of their ease of design, fabrication, and integration, in addition to their low-profile characteristics suitable for enhancing antenna performance. DRA's are usually fabricated, for research purposes, of materials with high permittivities: for example, ϵ_r=10 is commonly achieved using Alumina. The natural behaviour of the ceramic radiator enhances the overall radiated power efficiency of the antenna. This inherent characteristic contributes to the notable high gain observed in these structures, making them promising candidates for this application. [29], has demonstrated the potential to achieve comparable array gains through the implementation of double-coating techniques. Furthermore, their simple complementary design, capable of propagating both linear and circularly polarized signals, makes them well-suited for integration into MIMO systems.

2.3.2 Rectangular Dielectric Resonator Antennas resonance modes

From the perspective of utilising DR's as radiating elements, propagation within the rectangular material is expected to happen once excitation occurs. Waveguide propagation is expressed in terms of the generated modes in the direction of the longest axis inside the material. DRA modes are defined as the theoretical expressions for the electromagnetic fields inside the DRA; they can be classified as Transverse Electric (TE), Transverse Magnetic (TM) and Transverse Electromagnetic (TEM). Once the DRA is excited, the magnetic field, will experience constructive or destructive interference depending on the ceramic material characteristics, e.g. size, permittivity. The resonator generates TE modes, denoted as m and n, which are defined by the number of short magnetic dipoles generated inside the resonator and propagated on each x,y,z plane. According to [30], there is an increment in gain for higher-order modes and a bandwidth reduction as a result of the increase in the TE modes order. Fig. 2.7 illustrates the short magnetic dipole propagation in z direction.

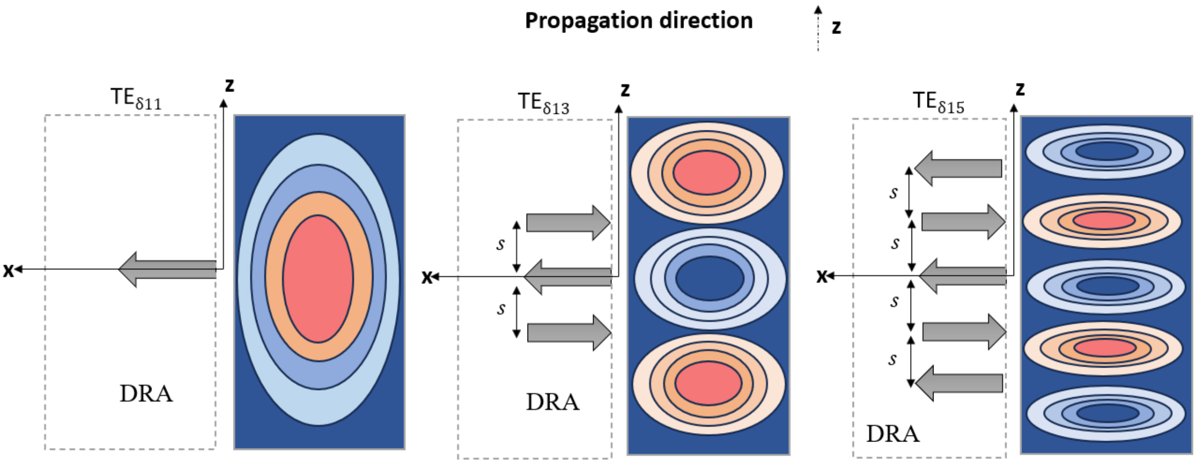

Figure 2.7: Short magnetic dipoles for 1,3 and 5 propagation modes

RDR waveguides mainly propagate TE modes due to the rectangular ceramic radiator material properties, at the same time perpendicularly, the TM modes will be present reaching the outline of the radiating structure. Fig. 2.8 initially shows a resonator, where w, h, and l represent the width, height, and length of the rectangular dielectric guide. In addition, the waveguide outer surfaces are expected to behave as Perfect Magnetic Conductor (PMC), simplifying the mathematical analysis presented below.

Dielectric Wave Model (DWM) [31] mathematically models the magnetic field extrema inside the RDRA, which can be expressed as [31]:

$$H_x = \frac{k_y^2 + k_z^2}{j\omega\mu_0} A cos(k_x x) cos(k_y y) cos(k_z z) \tag{2.18}$$

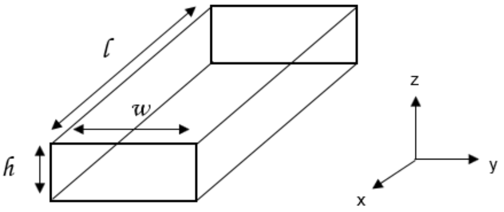

Figure 2.8: Rectangular Dielectric Resonator

$$H_y = \frac{k_y k_x}{j\omega\mu_0} Asin(k_x x)sin(k_y y)cos(k_z z) \tag{2.19}$$

$$H_z = \frac{k_z k_x}{j\omega\mu_0} Asin(k_x x)cos(k_y y)sin(k_z z) \tag{2.20}$$

The Electric field propagation inside the RDRA can be expressed as [31]:

$$E_y = Ak_z cos(k_x x)cos(k_y y)sin(k_z z) \tag{2.21}$$

$$E_z = -Ak_y cos(k_x x)sin(k_y y)sin(k_z z) \tag{2.22}$$

$$E_x = 0 \tag{2.23}$$

where A represents a constant and k_x, k_y and k_z the wavenumbers inside the Dielectric Resonator (DR). After considering the following boundary condition on the RDRA surface, $E \cdot n$ =0, which means that the electric field is zero normal to the surfaces of the resonators due to the perfect magnetic conducting wall (PMC) of the DRA's, for the wavenumbers:

$$k_x = \frac{\pi}{w}; k_y = \frac{\pi}{l} \tag{2.24}$$

and for k_z:

$$k_z tan(k_z \frac{d}{2}) = \sqrt{(\epsilon_r - 1)k_0^2 - k_z^2} \tag{2.25}$$

solving the equation:

$$k_x^2 + k_y^2 + k_z^2 = \epsilon_r k_0^2 \tag{2.26}$$

The resonant frequency of the antenna is key to understand the DR behaviour, mathematically and in free space, their relationship is expressed as:

$$k_0 = \frac{2\pi}{\lambda_0} = \frac{2\pi f_0}{c} \tag{2.27}$$

where k_0 refers to the free space wavenumber.

After substituting Eq. (3.10) in (3.8);

$$f_0 = \frac{c}{2\pi\epsilon_r}\sqrt{k_x^2 + k_y^2 + k_z^2} \tag{2.28}$$

From Eq. (3.11), it is assumed that c represents the speed of light 3x10^8 $\frac{m}{s}$, λ_0 which refers to the free space wavelength and ϵ_r the relative permittivity of the dielectric.

2.4 Antenna feeding mechanisms

2.4.1 Antenna element feed for RDRAs at C-band

In the context of DRAs, some of the most common feeding mechanisms in the literature refer to coaxial probe fed [32], aperture coupled fed [33], microstrip feedline [34], co-planar waveguide fed [35], conformal stripline [36]. However, the microstrip feedline is one of the most frequently utilized feeding mechanisms at the C-band due to its effective power usage at lower frequencies.

The microstrip line feeding mechanism consists of a Perfect Electric Conductor (PEC)/Copper material named as ground plane GP, a substrate, and a microstrip transmission line made of a conductive material, placed at the top as shown in Fig.2.9.

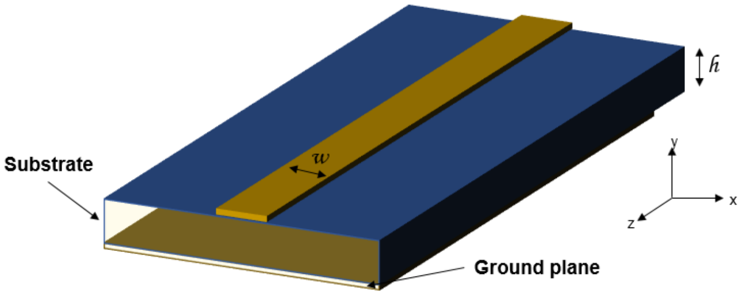

Figure 2.9: Microstrip feeding line for the RDRA.

2.4.2 Antenna element feed for RDRAs at mmWave

At mmWave, reduced size and increased accuracy are expected when working with antenna prototypes due to the nature of its frequency. Coaxial probe, CPW, aperture, and microstrip were compared by their performance in lower reflection coefficient losses resulting in wide impedance bandwidths for the design. In [37], the authors investigate the effect on the antenna performance with the aperture coupled slot and coaxial probe feeding mechanisms, concluding that the aperture slot feeding mechanism is the most suitable candidate for mmWave RDRA's because of its capability for achieving high isolation and impedance match.

Slot aperture variables can be calculated as [25]:

$$\epsilon_e = \frac{\epsilon_r + \epsilon_s}{2} \tag{2.29}$$

ϵ_r is the substrate permittivity.
ϵ_s is the DR substrate permittivity.

Derived from the wavelength propagation mathematical definition in the dielectric substrate:

$$\lambda_d = \frac{\lambda_0}{\sqrt{\epsilon_e}} \tag{2.30}$$

After considering $0.4\lambda_0$ [38]

$$ls = \frac{0.4 \cdot \lambda_0}{\sqrt{\epsilon_e}} \tag{2.31}$$

The slot aperture is designed to achieve coupling between the feedline and the RDRA; its size must be large enough to have sufficient efficiency and small enough to avoid resonance within the operating band.

$$w_s = 0.2 \cdot l_s \tag{2.32}$$

where l_s is the slot length and w_s is the slot width.

$$s = \frac{\lambda_g}{4} \quad \lambda_g = \frac{2\pi}{\beta} \tag{2.33}$$

s is the slot position.
λ_g is the guided wavelength.
β is the propagation constant.

The slot aperture design is presented in Fig. 2.10a. Additionally, Fig. 2.10b illustrates a lateral 3D view for a better understanding.

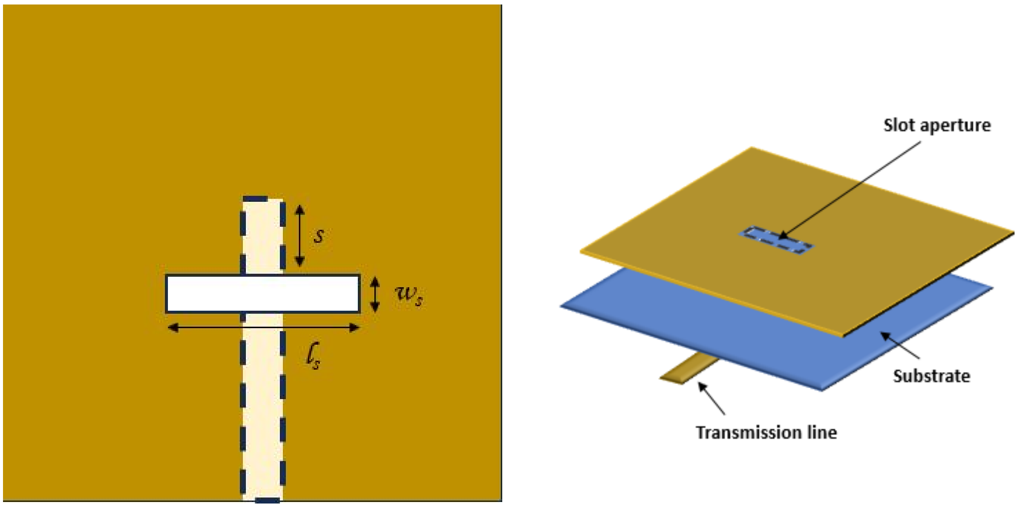

(a) 2D slot aperture view (b) 3D slot aperture view

Figure 2.10: DRA feeding mechanism parts

2.4.3 Antenna array T-junctions

Since the microstrip open loop design contemplates a summing network, the basic working principles of a T-junction illustrated in Fig.2.11 of a feeding network are presented below. This strategy can be repeated the amount times the number of radiators in the antenna requires them.

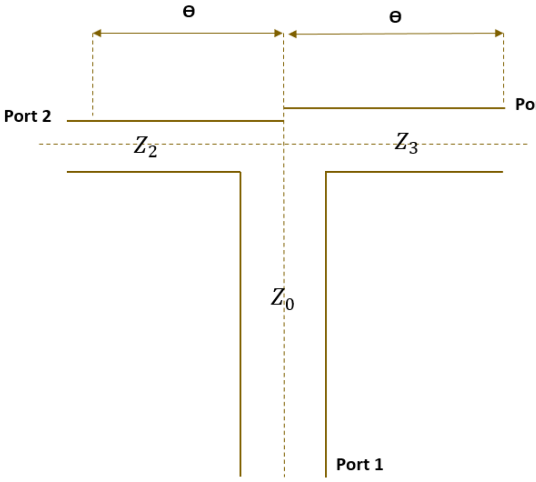

Figure 2.11: T-junction [19]

Assuming there is a single feeding port and a couple of radiators in the antenna, as mentioned before, input power in the T-junction terminals is taken into account by each port number labelled as P_1, P_2 and P_3 represents the power division expressed as:

$$P_3 = K^2 P_2 \tag{2.34}$$

where K is a constant provided by the designer assumed to be 1 for an equal splitting. Considering that $P_1 = P_2 + P_3$,

$$P_2 = \frac{1}{1+K^2} P_1 \tag{2.35}$$

$$P_3 = \frac{K^2}{1+K^2} P_1 \tag{2.36}$$

In terms of the voltage going through the transmission line, the position of Port 1 is denoted as V_0^+, which in the case of the junction voltages will be negative: V_2^- and V_3^- , input and output powers may be written as:

$$P_1 = \frac{|V_0^+|^2}{Z_0},\ P_2 = \frac{|V_2^-|^2}{Z_2},\ P_3 = \frac{|V_3^-|^2}{Z_3} \tag{2.37}$$

At the junction, $V_0^+ = V_2^- = V_3^-$, hence the characteristic impedance in relationship with the power levels are

$$\frac{Z_2}{Z_3} = \frac{P_3}{P_2} = K^2 \tag{2.38}$$

$$\frac{Z_2}{Z_0} = \frac{P_1}{P_2} = 1 + K^2 \tag{2.39}$$

After rearranging the impedances expression,

$$Z_2 = (1 + K^2) Z_0 \tag{2.40}$$

$$Z_3 = \frac{(1+K^2)}{K^2} Z_0 \tag{2.41}$$

Therefore, assuming a lossless transmission line, and two antenna elements, the Maximum Power Transfer Theorem [39] states an input impedance of $Z_0 = 50\ \Omega$. Consequently and after substituting Eq. 2.40 and Eq. 2.41, $Z_2 = 100\ \Omega$ and $Z_3 = 100\ \Omega$ ideally.

Assuming two more branches to the summing network and without considering any additional strategy for modifying the input impedance, $Z_2 = 100\ \Omega$, and $Z_3 = 100\ \Omega$. By replacing Z_2 as Z_4 and Z_6 from Eq. 2.40 and Z_3 as Z_5 and Z_7 from Eq. 2.41 as illustrated in Fig. 2.12 the following respective transmission line input impedance's will result in 200Ω. Some employed strategies in the literature are considered for tackling this dramatic change of impedance from junction to junction. A quarter wavelength transformer for reducing line impedance, line tapering, and parasitic elements.

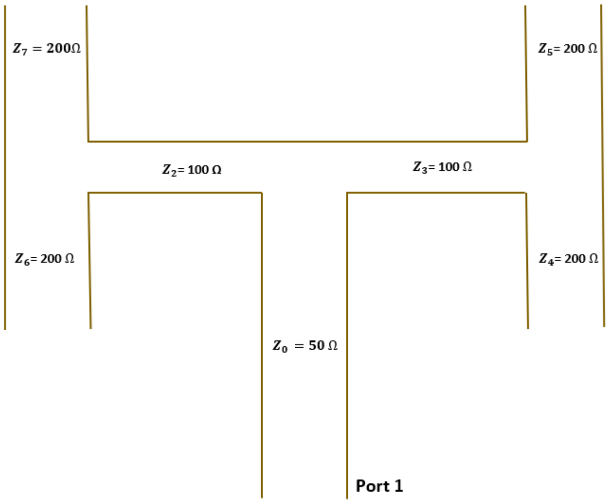

Figure 2.12: Two transmission line T-junction

2.5 MIMO principles

The MIMO system architecture emerged as a solution for the need to increase the end user bandwidth demands, providing spatial diversity for the several RF channels interacting through a communication system at the same time. According to [40] the performance of the MIMO can be evaluated using the Envelope Correlation Coefficient (ECC), Diversity Gain (DG).

2.5.1 Mutual coupling

Due to the high demand for robust communications systems, the necessity of increasing the number of antennas in the same spatial area emerged with the requirements of minimum coupling between the antennas to avoid channel interference. Researchers have been exploring the idea of designing different architecture scenarios for tackling this challenge: multiple antennas working on the same propagation structure with a common GP and multiple antennas working on the same propagation structure with an independent GP. The interaction of several antennas working using the same ground plane will likely generate unwanted coupling. This coupling is named in the literature as mutual coupling, [41] as the energy absorbed by a nearby antenna when at least one of the components is operating. The antenna radiation directions are illustrated in Fig.2.13. Once driven, the antenna is expected to radiate in different directions. From the antenna adjacent point of view, it is expected to receive radiation from its neighbours as well as generate its own. From the receiver point of view, both antennas will experience the wavefront upcoming radiation from the transmitter side. Also, radiation is expected from the receiving and adjacent directions as shown in Fig.2.13.

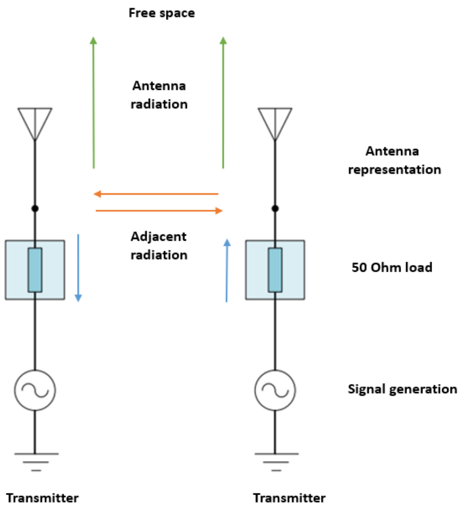

Figure 2.13: Mutual coupling mechanism [41]

The mutual coupling is expected to be present with $m \times n$ elements referring to the number of antennas interacting with the same conditions, radiating conceptually with a similar mechanism based on the antenna's particular design conditions.

2.5.2 Envelope Correlation Coefficient

As a result of the mutual coupling, researchers developed mathematical metrics for determining the performance of a MIMO system due to the previously mentioned phenomena present when more than one antenna is radiating at the same time with a common GP structure. ECC [40] determines the degree of independence between two adjacent antennas. For example, considering that one antenna is horizontally polarised and the second one is vertically polarised, the ECC is expected to be zero for the ideal case. The ECC for a lossless environment can be determined by considering the S-parameters of the antennas on the system:

$$\rho_e(ECC) = \frac{|\iint_{4\pi}[E_1(\theta,\phi) * E_2(\theta,\phi)d\Omega|^2}{\iint_{4\pi}|E_1(\theta,\phi)|^2 d\Omega \iint_{4\pi}|E_2(\theta,\phi)|^2 d\Omega} \tag{2.42}$$

2.5.3 Diversity Gain

The diversity gain DG measures the effect of the system diversity in a communication system. It is complementary to the ECC. When high isolation is achieved in between the antenna system, the DG value should ideally be 10. It can be calculated as:

$$DG = 10 \cdot \sqrt{1 - |\rho_e|^2} \tag{2.43}$$

Chapter 3

Literature Review

3.1 mmWave antenna arrays

Throughout the literature, work with high gain and a variety of polarisations has been published in [42], with a 2 × 2 subarray structure achieving ∼12dBic, a couple of multilayered stacked designs in [43]- [44] with ∼6 dBi gain and no CP, even though the authors show a complex design structure, the gain can be improvable with simpler design techniques and reduced size. An antenna array with dual-polarisation and a realized gain of 11.1 dBi has been reported by utilising an Antenna in Package (AiP) stacked structure [45]. Another 2 × 2 C-band antenna array was proposed with a sequential rotation and unidirectional radiation pattern achieving a peak gain of ∼13.5 dBi [46]. The reported studies in [47] and [48] demonstrate a gain of 12dBi and 10.84 dBi respectively, the second with a CP bandwidth of 54.28 %. In another study, a patch antenna array with a peak gain of 4.83 dBi was proposed [49].

Although the literature contains a wide variety of 2 × 2 antenna array microstrip designs [42]- [44], [45]- [49] mainly achieving CP and particularly [42]- [45] operating at the mmWave spectrum, they involve relatively complex designs for achieving high gain results.

3.1.1 Rectangular DRA MIMO

In recent years, RDRA's designed at the C-band, has been studied not only as individual elements which can provide a wide impedance bandwidth, high gain, and CP but also because they are potential candidates for being integrated in MIMO structures. Throughout the literature, some recent designs reported work in [50] , [51], [52] presents four element DRA MIMO, shared a GP. Despite the resonators contemplate a variety of geometric shapes, they expose a LP, with gains less than 6.5 dBi. Literature also reports a variety of ceramic DRA such as cylindrical [53], [54], H-shaped [55], [56], [57], Z-shaped resonator [58], hemispherical [50], also considering non-conventional shapes such as ring [59], S [60], cross [61] and rectangular [52], [62], [63] which is of the main interest within the present study. In the case of DRA's, some of the designs working with CP are reported in [64], [65] highlighting an efficiency of ~ 95 %.

In terms of MIMO performance metrics, [62] shows a maximum isolation of 30 dB. [50] and [57] systems demonstrate an ECC<0.002, additionally [57] shows a DG of almost 10. At this point, it is important to point out that [64] belongs to the limited studies demonstrating four elements architecture, achieving CP, with a maximum gain of 5.5 dB, an ECC of 0.03 and a DG > 9.8 at the C-band, ranging from 4 to 8 GHz, [66].

Referring to the MIMO testing available methodologies in the literature, it is important to mention the port excitation differs throughout the designs. In a general way, the system analysis is based on the feeding of each antenna individually, terminating at 50 Ω the non-connected ports of the structure. Despite the design being designed for the 8.5-12.5 GHz frequency band, [60] reports a single feeding point for all of the design testing.

3.1.2 RDRA MIMO at mmWave with Linear Polarisation

The mmWave spectrum started to popularise between MIMO DRA designs as a potential solution to maximise both technologies capabilities. Literature discusses predominantly RDRA in [67–71] since the geometrical shape is manageable for fabrication, and alignment because of the millimeter size of the component. Some other published MIMO non-rectangular resonators are [72–75] which consist of cylindrical ceramics. According to MU-MIMO for last mille applications, literature reports studies with a prototype design either two element setup presented in [70–73], [76], [77] or four element architecture [67,68] , [74] , [78,79], which most of the times is not complemented with design iterations unit the final results. The average of four portMIMO architecture reported realized gain ranges between 7.5 dBi to 12 dBi, considering efficiencies not smaller than 86 % due to design modifications such as bending of the transmission line, utilising alternative grounding techniques, and multi-layer designs. Additionally, there is a prevalence between the reported MIMO systems of unidirectional radiation patterns, whose radiation strength is proportional to the number of elements of the design. Referring to the experimental methodology throughout the presented work, the radiation patterns of the four element RDRA's before mentioned are usually obtained by exciting one antenna port at a time, terminating at the same time at 50 Ω the non-utilised ports. Few publications expose the simultaneous feeding of the system as [74] which has an integrated four-way power divider on the PCB, belonging to the multiple antennas. Referring to the MIMO system performance metrics, ECC through the published work is < 0.15, obtaining as a result a DG not smaller than < 9.9 demonstrating a degree of independence as well as system diversity within the stated thresholds of the technology. An important aspect to mention is the feeding mechanisms of the MIMO 4 element designs.

3.1.3 RDRA MIMO at mmWave with Circular Polarisation

The design of DRA's with CP at the mmWave in MIMO systems results in an interesting challenge for researchers due to the number of variables that need to be addressed to obtain a good antenna system performance. Due to this fact, there is a limited number of reported designs in the literature. In [80], a 2 element RDRA design is reported with a peak gain of 5.84 dBi at the mmWave spectrum. It employs a Complementary Split Ring (CSRR) for addressing the inter port isolation and obtaining a maximum 25 dB reduction. The design presents an Axial ratio <3 dB of 11.6 % and an antenna size of 27.5 mm × 30 mm. Moreover, [81] reported a Hemispherical Dielectric Resonator Antenna (HDRA) working at mmWave. The main highlights of this design refer to a maximum gain of 10.3 dBi attributed to the use of a Ridge Gap Feed Line. The design reports an Axial ratio <3 dB of 1 GHz.

3.1.4 MIMO isolation techniques

When designing MIMO antenna systems, a crucial consideration is the isolation between antenna elements due to the positioning, radiation, and GP interaction. Simplicity and a low-loss/ high inter element isolation designs will be preferred for achieving a high quality performance system. Some of the most common utilised isolation techniques for Dielectric Resonator Antenna (DRA) presented in the literature are classified as diversity techniques, Electromagnetic band-gap structures (EBG's), metamaterials, metasurfaces, frequency selective surfaces (FSS), dielectric superstrates, conformal metal strips, metallic vias, defected ground structures [82].

A high level of design complexity and fabrication at mmWave can be observed for EBG's, some illustrative cases for microstrip antennas are presented in [83] where there is an isolation of about $\sim$ 65 dB attributed to the EBG located at the centre of the design. In [84], an improvement is reported in terms of a 1.9 dBi increment in gain. Moreover, the effectiveness of this technique is applied to DRA's presented in [85] and [86] where the effects of the EBG are focused on a size reduction in combination with an isolation of 15 dB and an Impedance Bandwidth improvement for about 11.5 % attributed to mushroom type unit-cells. In addition, the EBG technique affects the antenna radiation beam when designing a multibeam MIMO system. Metamaterials are present in the literature in MIMO systems for mmWave microstrip designs such as [87, 88] demonstrating a maximum isolation of 5 dB and 18.5 dB respectively. Research has been made to investigate DRA's at mmWave with metamaterials in [78, 89] demonstrating an inter element mutual coupling reduction of 16 dB on average. In addition, metasurface designs are reported in [90, 91] demonstrating isolation ranging from

5 to 26 dB on the designs as an advantage of the implemented technique. The use of FSS is present in planar MIMO antenna systems [92], [93] where the surface effect is directly observed on an antenna gain of 8.6 dBi and 5.3 dBi. In [94], the VSWR ≤ 3.5 improvement is observed. A DRA MIMO system is presented in [95] with an improvement of the antenna gain to 8.1 dB. Next, dielectric superstrates work is reported in [96–98], with a good isolation reduction of $\sim$ 17 dB, 25 dB, and a 3 dB gain increment respectively. The presence of simpler design techniques as the addition of conformal strips on the ceramic material walls is identified. The literature lacks the presence of MIMO systems designed at mmWave frequencies. Some of the presented work at the C and X frequency bands, with a maximum reduction in inter-element mutual coupling of 28 dB [99, 100] Metallic strips applied on the DRA designs are illustrated in [101–104] having a clear effect on the isolation between inter elements of 12 dB, 25 dB, and 33 dB. Finally, Defected Ground Structure (DGS) presented in [105, 106] shows a mutual coupling reduction of 10 dB and 18 dB respectively.

Chapter 4

Microstrip planar Double Sided Parallel Line open loop array

This chapter proposes initially a simple microstrip open loop antenna which promises a high gain attributed to an array design based on its multiple double-sided radiators [107]. A wide circular polarisation bandwidth, which reduces the chances for polarisation mismatch losses under the antenna transmitter and receiver orientation. The feasibility of utilising the antenna design in a MIMO system is investigated throughout this section. The chapter highlights two main sections of the design: radiator and feeding mechanism, ending with its findings. Antenna simulations are presented and their validity is discussed. Subsequently, experimental measurements are performed to corroborate promising simulation outcomes.

4.1 Double-Sided Parallel Strip Line transition structure

The antenna array is designed using a microstrip line located on both sides of the substrate; the general feeding mechanism based on [108] and has three stages, starting from the edge of the substrate in the direction of the array radiators. The feeding transition ensures an input impedance of 50Ω right before the T-junction so that it can excite two layers of the substrate at the same time as shown in Fig. 4.1 based on the conformal mapping of the dielectric boundary [109].

The first stage of the feeding mechanisms, illustrated in Fig. 4.2a, consists of a Conductor Backed Coplanar Waveguide (CBCPW) with a positive pole, located at the top, and its corresponding negative pole, located a the bottom, in blue. The electric field is propagated from the central to the lateral pads and in the direction of the ground plane. Copper vias also connect the upper and lower negative rails to continue a common ground plane. For the

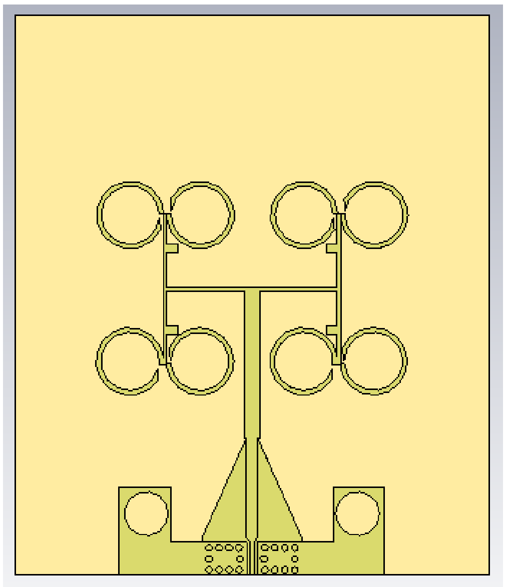

Figure 4.1: Two transmission line T-junction

second stage, illustrated in Fig. 4.2b, lateral pads turn into an unbalanced Microstrip Line (ML). The third stage, illustrated in Fig. 4.2c, will finalise with a Double Sided Parallel Strip Line Transition (DSPSL) which equally distributes the area on both sides of the substrate. The middle dash line across the three cases of substrate represents the GP of the design.

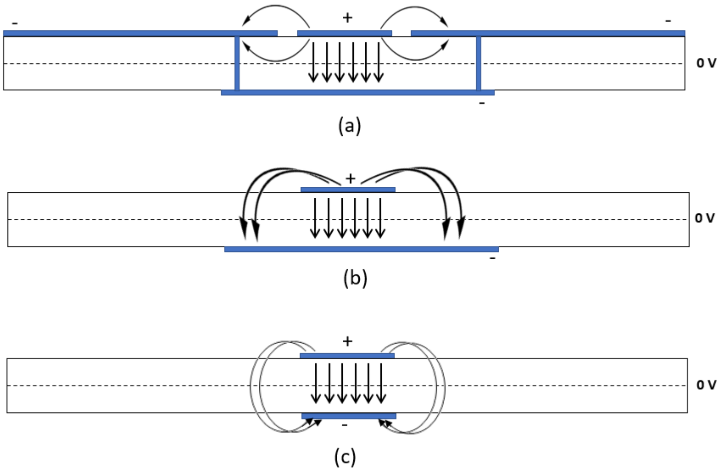

Figure 4.2: (a) First stage (b) Second stage (c) Third stage of the feeding transition mechanism

4.2 Polarisation considerations

In a communication system, antennas work in a pair dynamic, meaning that one of them will work as the transmitter and the reciprocal as a receiver, depending on the nature. The antenna alignment will be positioned carefully so that the Line Of Sight (LOS) can be placed in a range not bigger than $\frac{\lambda_0}{3}$ apart from the exact linear alignment of the two antennas [110]. As the higher accuracy will lead to maximum power transfer in between both ends. In daily life, several working scenarios are not necessarily suitable for a strictly linear positioning between the transmitter and the receiver, as a result of the misalignment, multi-path reflections, and power losses. Circular polarisation represents the capability of the antenna to propagate EM waves as a circular pattern, preserving the maximum power transmission. Power losses are described as part of Faraday's effect [111] due to the relationship between light and electromagnetic waves which will affect the orientation in the transmitting/receiving propagation. If the EM waves will propagate i.e. the z-axis for simplifying the mathematical analysis, circular polarisation can be illustrated with the polarisation ellipse shown in Fig. 2.2.

4.3 Experimental methodology

The experimental scenarios for the open loop antenna consisted of three different setups which will be detailed in this section. Measurements were taken inside the UKRI National Millimetre Wave Facility at The University of Sheffield.

As a basic initial test, the continuity of the feeding network with the connector was tested for its acknowledgment.

The first experimental setup refers to the Scattering parameters measurement, S-parameters. The antenna was assembled with the Polytetrafluoroethylene (PTFE) rail and the SubMiniature version A (SMA) connector was inserted. For testing the antenna impedance matching with their corresponding resonant frequencies, the prototype was connected to the Vector Network Analyser (VNA) PNA-X Network Analyzer N5245B running the Scattering parameters test shown in Fig. 4.3. The VNA was previously calibrated according to the frequency range and testing port previous to the evaluation.

The second one for measuring the antenna radiation pattern, involves the scan, with the aid of a rotational arm mechanism, of the antenna array for determining its radiation pattern inside the mmwave anechoic chamber. The antenna setup consisted of a horn antenna working as a transmitter of the model illustrated in Fig. 4.4. The presented antenna throughout this chapter was used as a receiver, working as the Antenna Under Test (AUT) in the system.

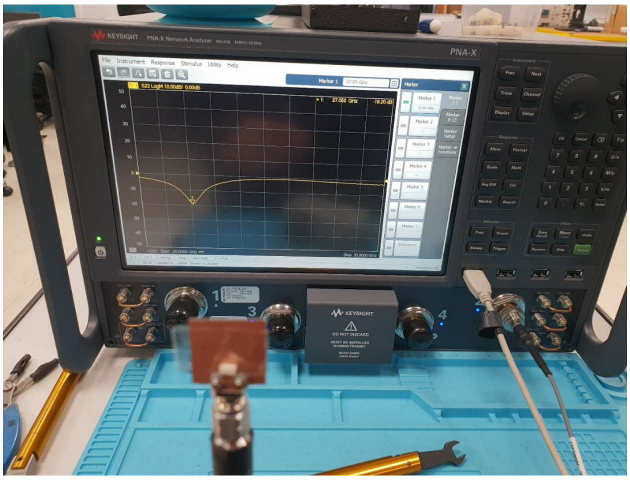

Figure 4.3: VNA analyzer test setup

Figure 4.4: Radiation pattern measurement setup

The transmitter side was rotated from ϕ= -90 ° to ϕ= 90 ° across the AUT and resulting in a 3D pattern of its radiation pattern.

In the third scenario, a reference measurement inside the mmwave anechoic chamber was taken into account to obtain the antenna gain. The generalities of this radiation pattern test will be explained below. As the initial measurement, a couple of horn antennas were located as transmitters and receivers to determine the received power in one of them so that reference power values could be defined. Afterwards, the AUT horn antenna was replaced with the presented design, and the received power was measured. Fig. 4.5 illustrates the test setup. The open loop antenna was replaced with a horn antenna for the first case.

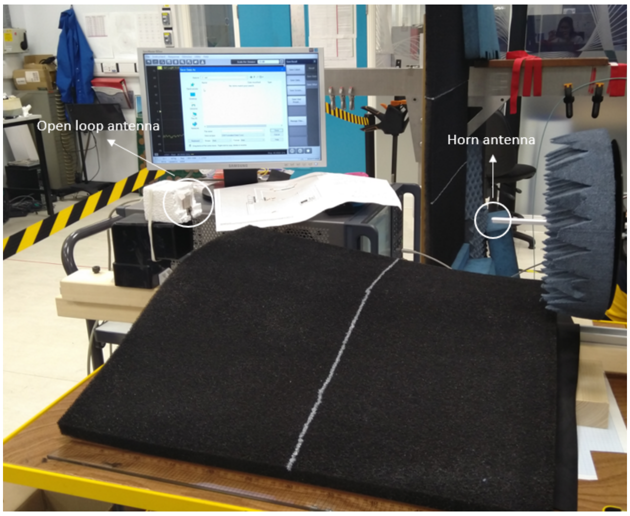

Figure 4.5: Antenna gain setup

4.4 Open loop antenna design stages

In this section, the design iterations of the open loop antenna array will be explained in detail as simulated until the final fabricated design is reached. Fig. 4.6 illustrates the iteration stages of the open loop antenna array. The relevant parameters to be presented in each iteration stage are: S-parameters, Antenna radiation pattern, gain, and Axial Ratio.

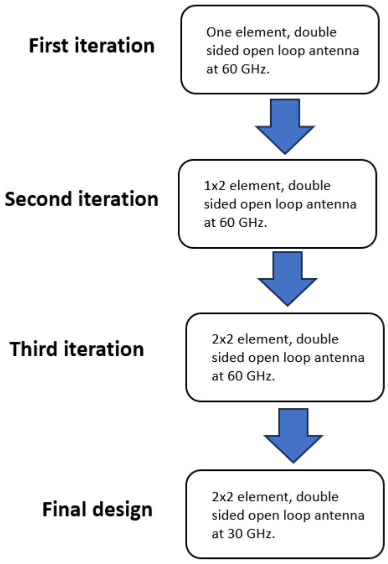

Figure 4.6: S-parameters 1x2 open loop design

4.5 A Open loop at 60 GHz

4.5.1 Antenna design considerations

As the starting point, a single, double sided open loop antenna was designed based on [112]. It was contemplated to work at the mmWave/ WiGig standard considering a resonant frequency of 50 GHz. The relationship between the antenna frequency with its wavelength is defined as:

$$f = \frac{c}{\lambda_0} \tag{4.1}$$

f is frequency in Hz
c is the velocity of light, 3x10^8 $\frac{m}{s}$
λ_0 is wavelength on free space

For the first case, $\lambda_0 = 5$ mm when substituting in Eq. 4.1 at 28 GHz. The antenna substrate dimensions were defined as approximately $2\lambda_0$. The substrate permittivity considered for this first iteration was $\epsilon_r = 2.17$ with a thickness of 0.127 mm. The proposed antenna has a three-layer structure [107]. The top layer consists of an open loop antenna double-sided array which mirrors the design on the bottom. A polyurethane foam layer is inserted in the middle to provide the required physical support. A copper reflector was incorporated at the bottom of the structure as illustrated in Fig. 4.7a

The open loop utilised dimensions were $d = 0.178\lambda_0$ as the external diameter with a 0.12 mm of width in direction to inwards the loop. A transmission line length of $ly = 0.94\lambda_0$. Fig. 4.7 illustrates the design.

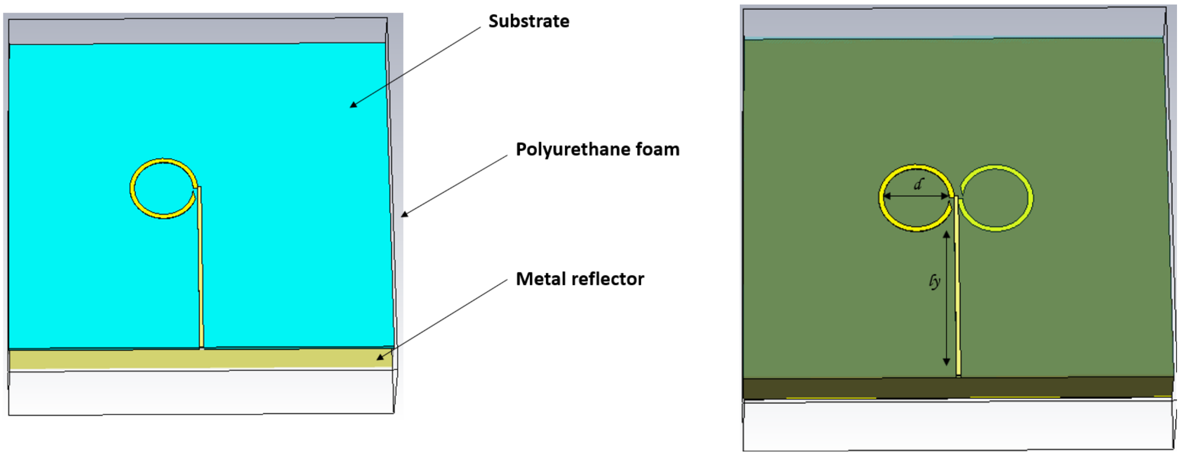

(a) Upper loop view (b) Antenna double side view

Figure 4.7: Open loop initial design

4.5.2 S-parameters

The S-parameters expose an impedance bandwidth of 3.73 % at a resonant frequency of 55.4 GHz as shown in Fig. 4.8.

4.5.3 Antenna radiation pattern

Moving on to the resonant frequency, Fig. 4.9 shows the simulated result of a unidirectional radiation pattern in z-axis direction with a maximum gain of 8.54 dBi.

4.5.4 Axial ratio

The triangular gap on the antenna design, in addition to the diagonal cut throughout the loop allows the generation of CP which is represented in Fig. 4.10. The Axial ratio <3 dB

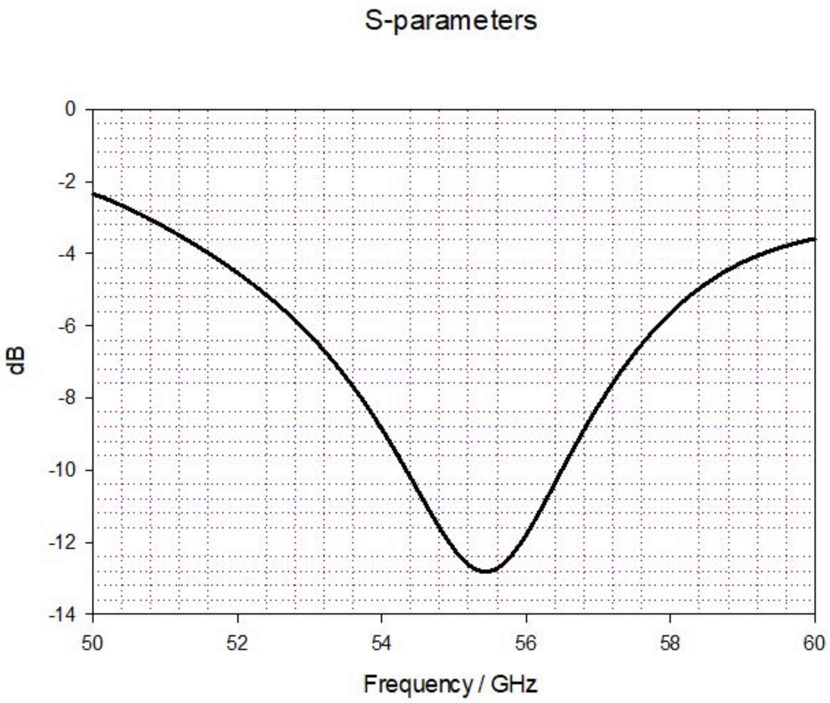

Figure 4.8: S-parameters one loop design

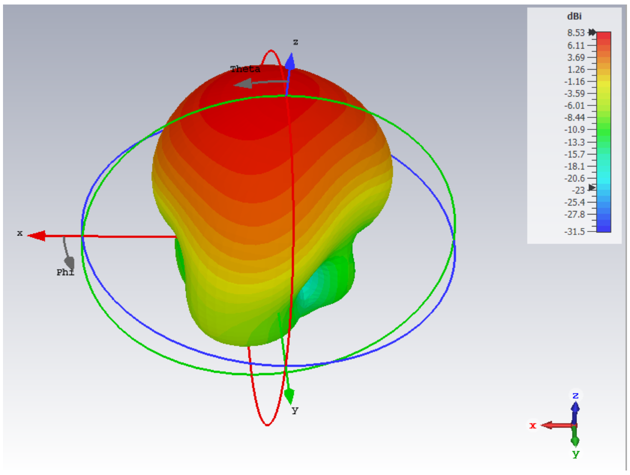

Figure 4.9: Simulated radiation pattern double sided loop element

shows a 11% bandwidth which overlaps with the corresponding impedance bandwidth of the first iteration.

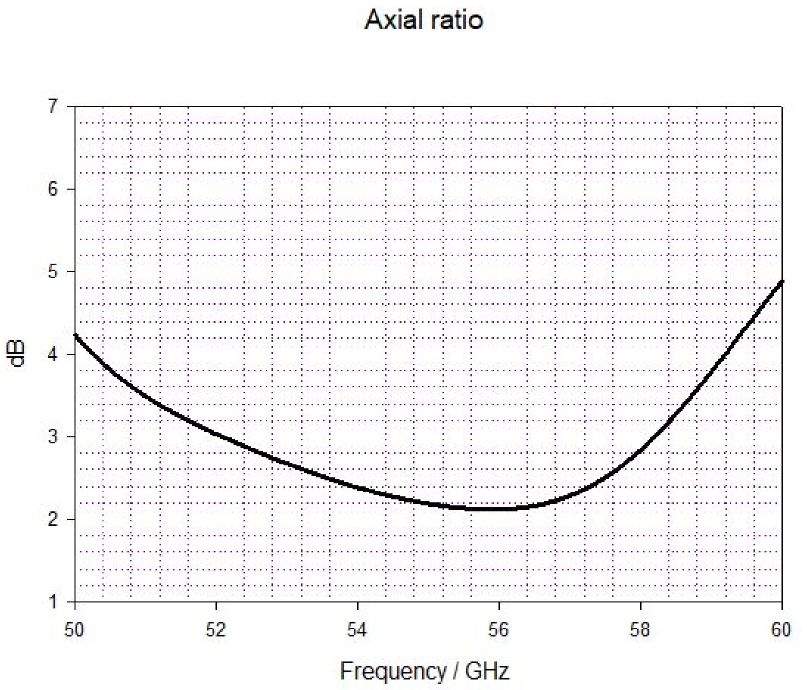

Figure 4.10: S-parameters one loop design

4.6 1 × 2 Open loop array at 60 GHz

4.6.1 Antenna design considerations

Following Fig. 4.6, the second iteration refers to the 1 × 2 antenna open loop design which by adding two more elements to the array, modifies the transmission line impedance when adding the T-line feeding. The design considerations are similar to the previously explained antenna, the T-line dimensions are $lx = 4.20$ mm and are illustrated in Fig. 4.11b.

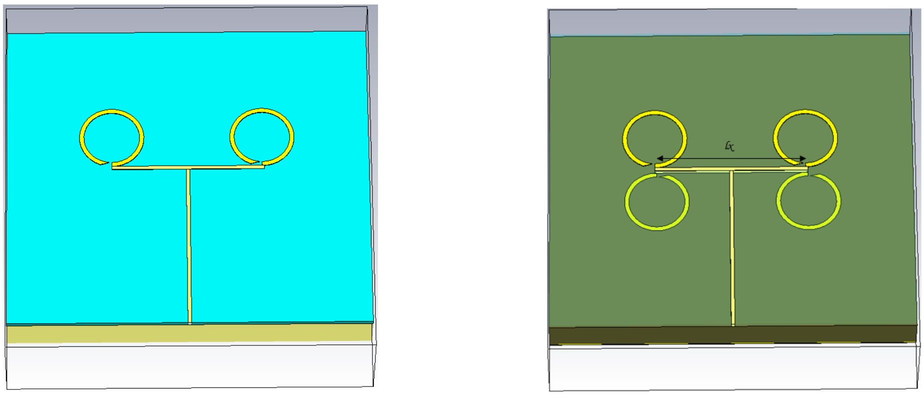

(a) Upper loop view

(b) Antenna double side view

Figure 4.11: 1 × 2 Open loop design

4.6.2 S-parameters

The S-parameters expose an impedance bandwidth of 4.61 % at a resonant frequency of 53.27 GHz as shown in Fig. 4.12. Compared with the first iteration, its impedance bandwidth remains the with the same value.

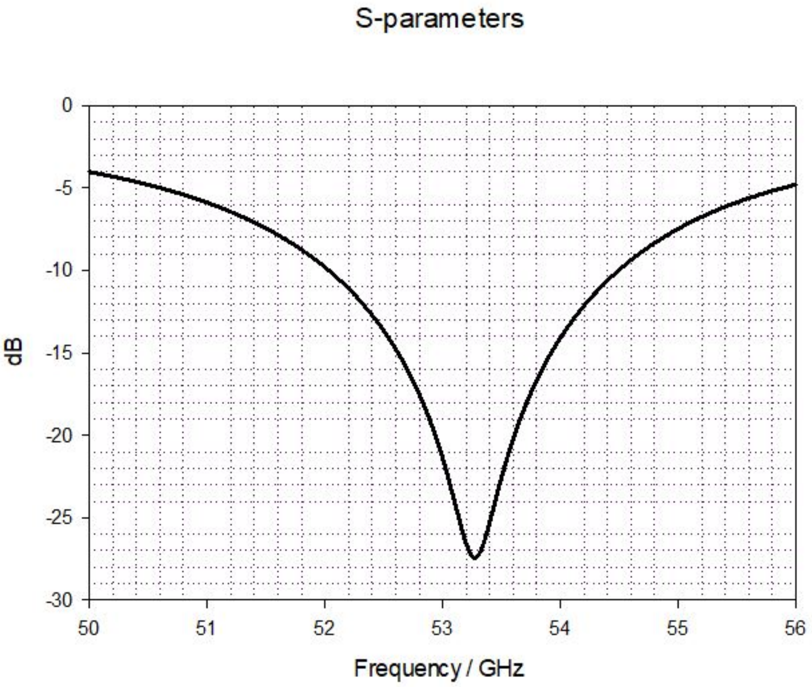

Figure 4.12: S-parameters 1 × 2 loop design

4.6.3 Antenna radiation pattern

Moving on to the resonant frequency, Fig. 4.13 shows the simulated result of a unidirectional radiation pattern in z-axis direction with a maximum gain of 11.4 dBi. The addition of two loops provides an increment of 2.86 dBi to the array.

4.6.4 Axial ratio

Fig. 4.14 shows the antenna design with the two additional double-sided loops. The axial ratio <3dB represents 10.80% bandwidth which overlaps with the corresponding Impedance bandwidth for this case. Comparing results, the <3 dB axial ratio bandwidth remains the same.

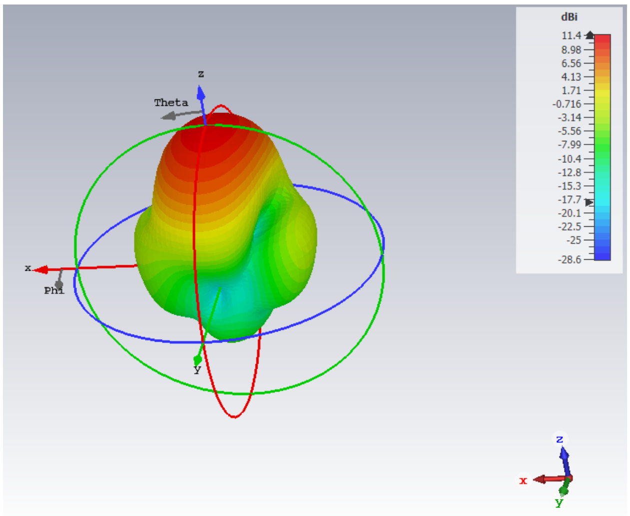

Figure 4.13: Simulated radiation pattern 1 × 2 double-sided loop element

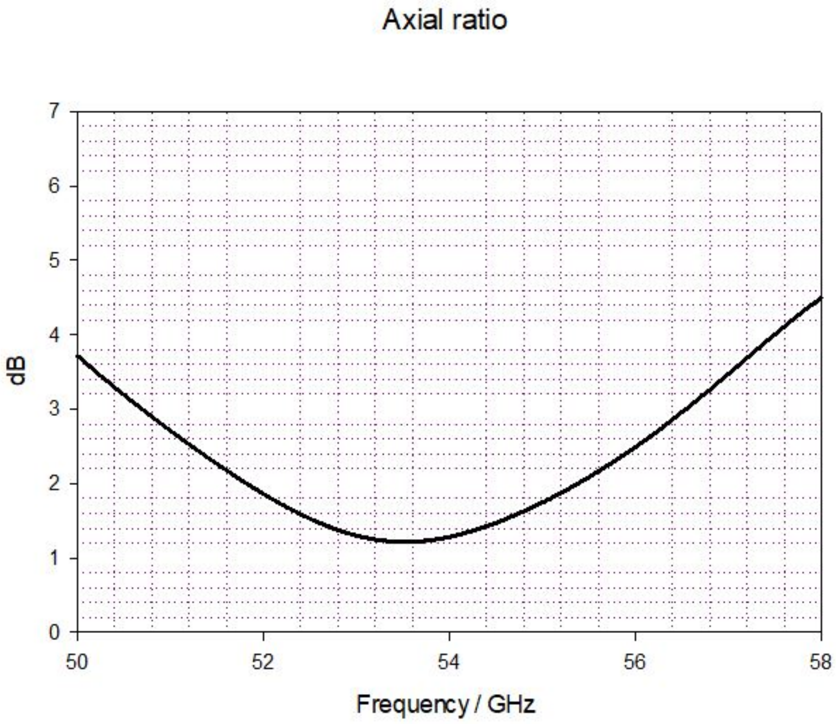

Figure 4.14: S-parameters 1 × 2 open loop design

4.7 2 × 2 Open loop array at 60 GHz

4.7.1 Antenna design considerations

For the third iteration, a couple of open loops were added to enhance the gain of the array. Fig. 4.15 illustrates the design overview. The feeding transition is explained in detail in section 2.4.4. The antenna array substrate was modified according to the commercial values of the materials for its fabrication, the utilised material was Rogers RO3003 $\epsilon_r = 3$. Their main advantages are the lowest electrical loss, uniform electrical properties, ease of cutting, and machining. A symmetrical stub was added on top and bottom of the substrate attached at the primary crossed T-junction of the antenna. It contributes to the antenna matching compensating strategy, its corresponding size is length 0.064 λ_0, width 0.02 λ_0, it can be shown in Fig. 4.15. The stubs are present from the third iteration and were modified according to the operating frequency of the antenna.

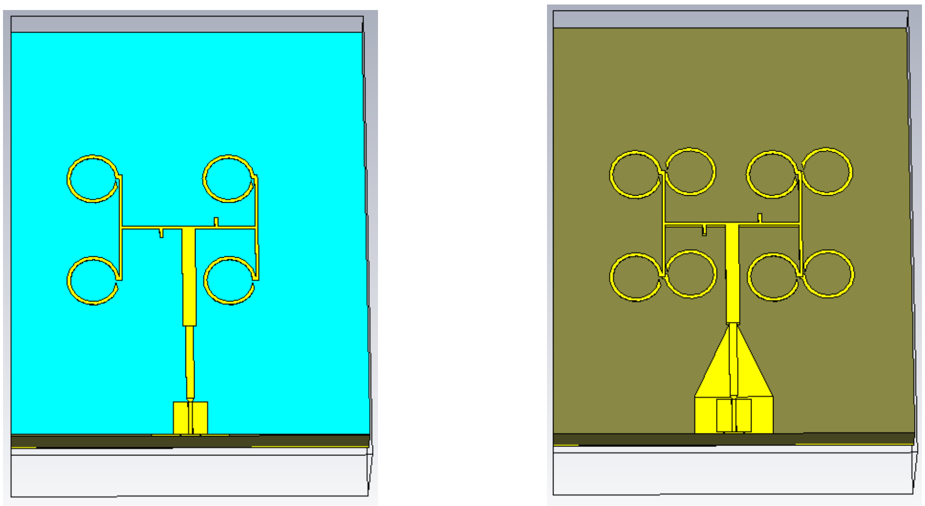
(a) Upper loop view

(b) Antenna double side view

Figure 4.15: 2 × 2 Open loop design at 60 GHz

4.7.2 S-parameters

The S-parameters expose an impedance bandwidth of 5.05 % at a resonant frequency of 55.56 GHz as shown in Fig. 4.16.

4.7.3 Antenna radiation pattern

The radiation pattern at the resonant frequency of interest is shown in Fig. 4.17 where the simulated result of a unidirectional radiation pattern in z-axis direction with a maximum gain of 13.8 dBi.

4.7.4 Axial ratio

Fig. 4.18 illustrates the addition of the two double-sided loops to the array. The Axial ratio represents a 9.03 % bandwidth which overlaps with the corresponding Impedance bandwidth

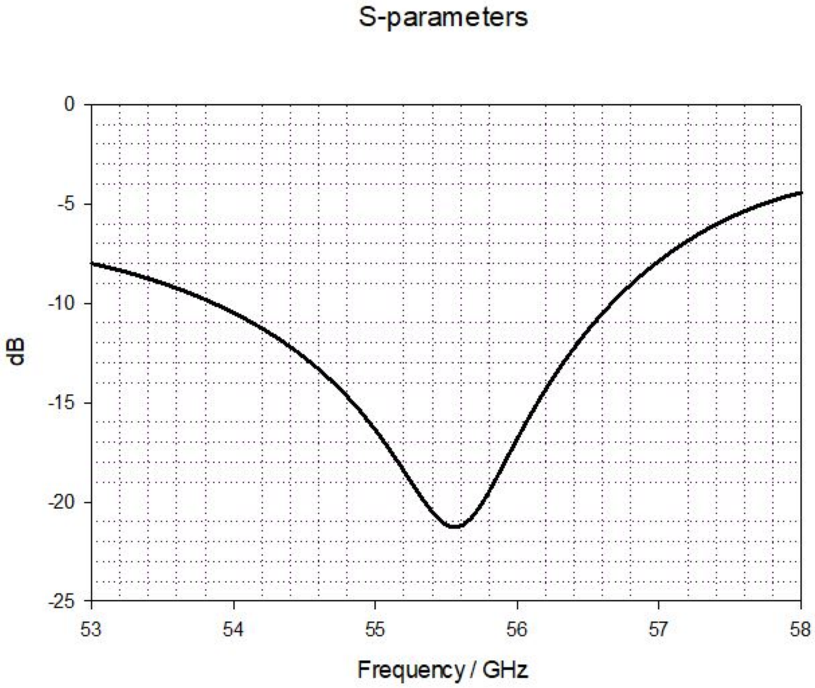

Figure 4.16: S-parameters 2 × 2 loop design

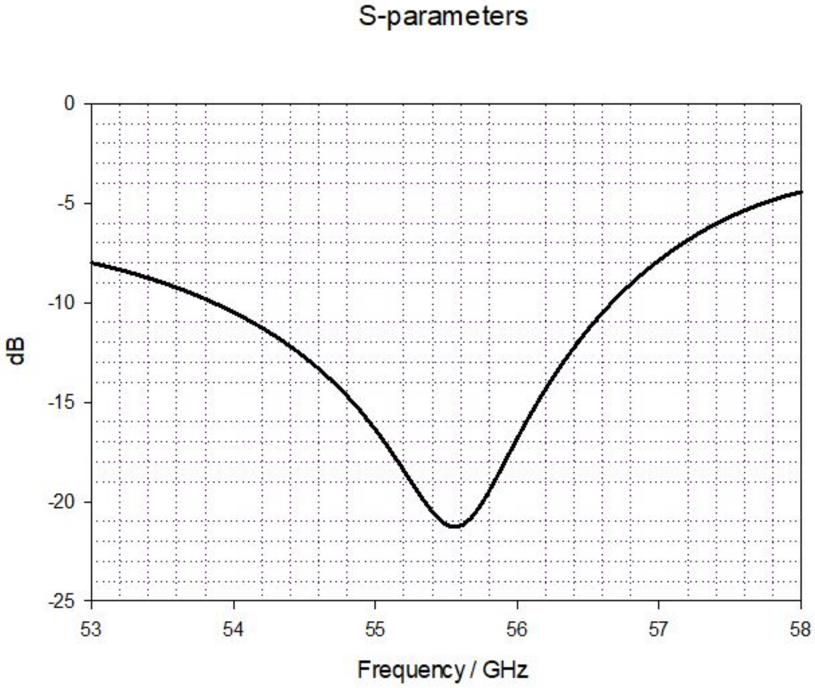

Figure 4.17: Radiation pattern 2 × 2 double sided loop element

before mentioned. Comparing the present results, there was a reduction of around 1.77 % in the <3 dB axial ratio bandwidth.

In comparison with the previous iteration, the impedance bandwidth remains the same.

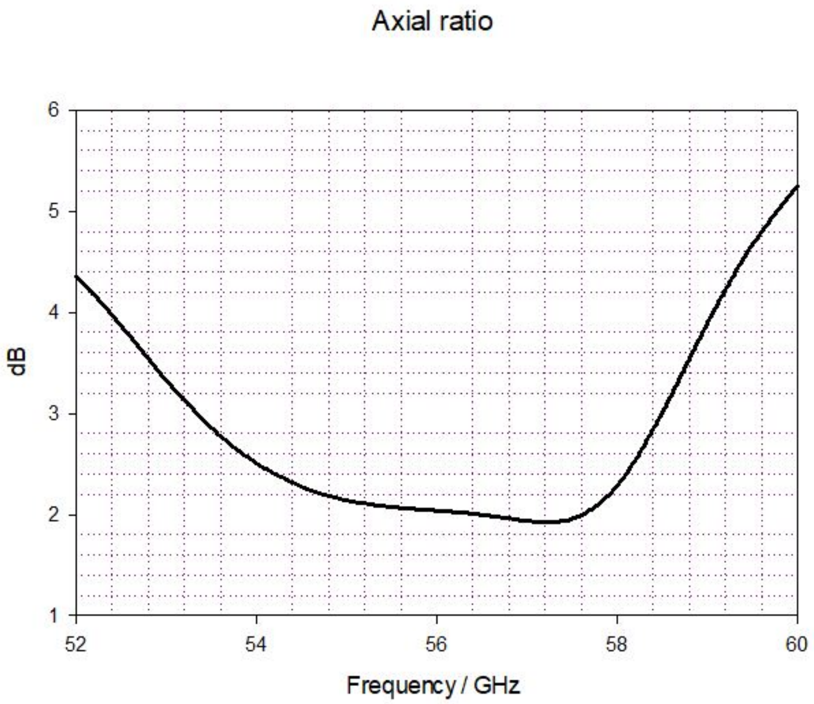

Figure 4.18: Axial ratio of 2 × 2 loop design

The gain was increased simultaneously with the addition of the antenna loops of about 2.4 dBi and a reduction in Axial ratio <3 dB of 1.77% due to simulation adjustments.

4.8 Feeding array mechanism at 30 GHz

The transmission line impedance transitions with DSPSL include the simultaneous feeding of a couple of antennas located in the same area based on preserving a 180 °difference between the top and the bottom transmission lines signal. This is based on the conformal mapping of the dielectric boundary [109]. The transition frontal view is illustrated in Fig. 4.19a. with the following dimensions *wb* = 4.47 mm , *w* = 0.18 mm , *w1* = 0.52 mm, *lp* = 1.51 mm, *lp1*= 4 mm, *lt* = 4.47 mm. The complementary view is illustrated in Fig. 4.19b. where *lb* = 4.4 mm, *lb1* = 1.74 mm. Both faces are connected through twenty vias of 0.30 mm diameter, distributed symmetrically as shown in Fig.4.19b. for grounding all the structure. The antenna's outer dimensions are 25.41 × 21.54 mm.

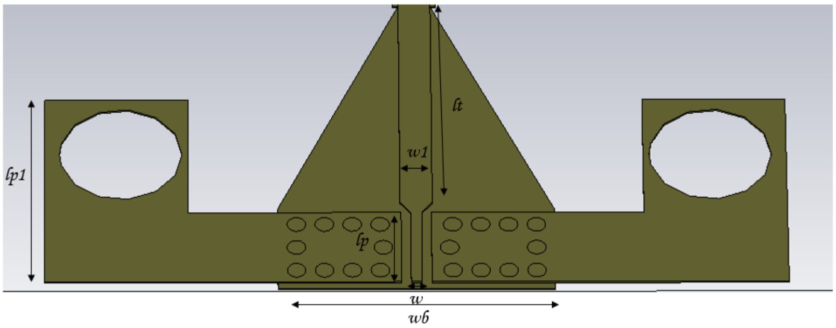

(a) Front side view

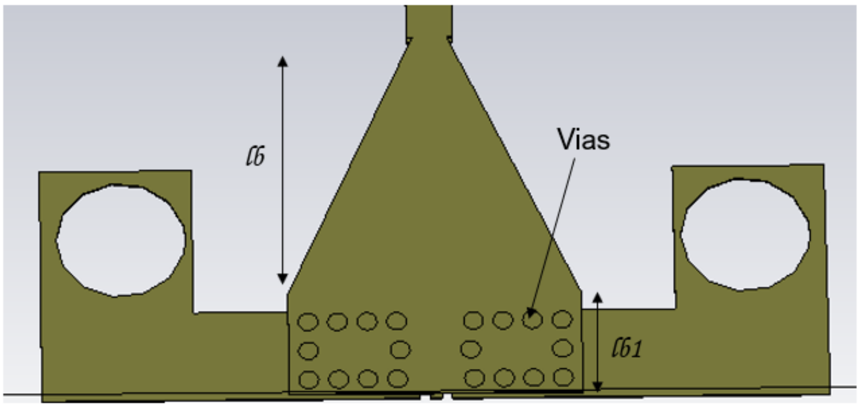

(b) Back side view

Figure 4.19: DSPSL 50 Ω microstrip transition.

4.9 2 × 2 Open loop antenna array design at 30 GHz

4.9.1 Antenna design considerations

As the final iteration, the design was scaled up to 30 GHz due to the fabrication minimum size requirements of the prototype. The final proposed antenna has a three-layer structure [107]. The top layer consists of an open loop antenna double-sided array that is printed on a RO3003 substrate with a relative permittivity of $\epsilon_r = 3$, and a thickness of 0.130 mm as illustrated in Fig. 4.20a. The design was adapted to the characteristics of the before mentioned substrate. A copper reflector was incorporated at a distance of 2.28 mm below the substrate with a polyurethane foam layer inserted in between to provide the required physical support. The antenna consists of a 2 × 2 array. As can be observed from Figs. 4.20a and 4.20b, the array elements are fed using microstrip transmission lines that are located on both sides of the same substrate. The transmission line was incorporated with a DSPSL transition structure for matching and practical feeding [113]. It should be noted that an open circular antenna supports a travelling wave current distribution to generate circular polarisation.

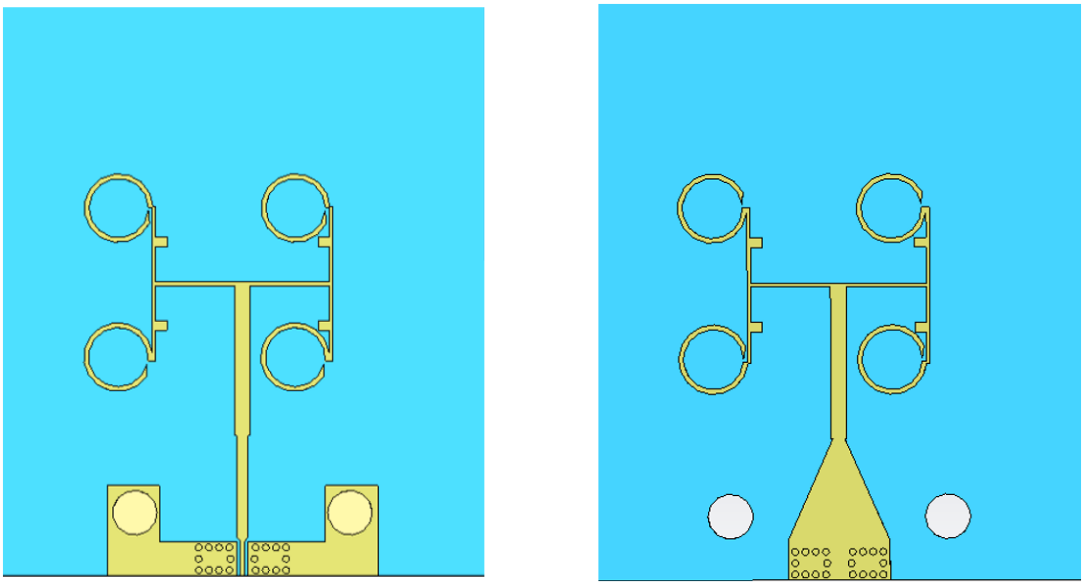

(a) Front view (b) Back view

Figure 4.20: Open loop antenna array at 30 GHz.

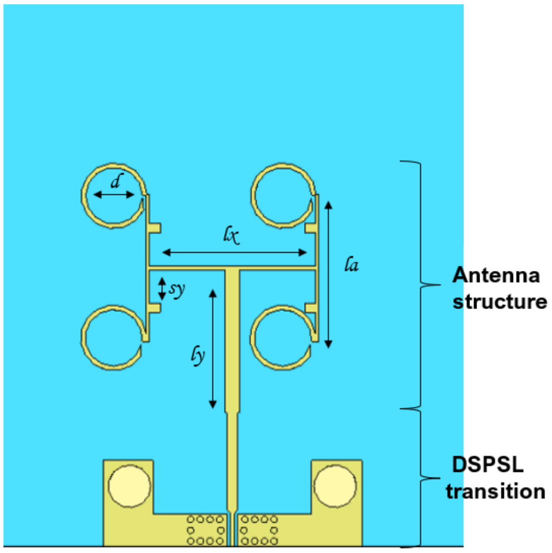

Figure 4.21: The proposed antenna dimensions, upper view.

4.9.2 Antenna dimensions

The radiating section illustrated in Fig. 4.21 with dimensions of Table 4.1 proposes a loop diameter d, with a T feeding structure of dimensions lx and ly. The transversal feeding line to lx is defined as la and the distance from the endpoint to the stub transformers is 1.55 mm. The impedance is matched using four double-sided stubs with dimensions 0.4 × 0.5 mm.

Table 4.1: Antenna array dimensions

Variable name	dimension (mm)
d	3.05
lx	7.7
ly	6.64
la	6.83
sy	1.56

4.9.3 S-parameters

The measured and simulated reflection coefficients are presented in Fig. 4.22 with an impedance bandwidth of 4.60%, within a frequency range of 29 to 30 GHz and 3.55% within a frequency range of 33 to 34 GHz. The measured results are in close agreement with the simulations. However, the measured bandwidth of the 1st band is 6.75% compared to the simulated counterpart of 4.6%. This difference can be attributed to the design of the antenna open loop radiators in combination with the array impedance.

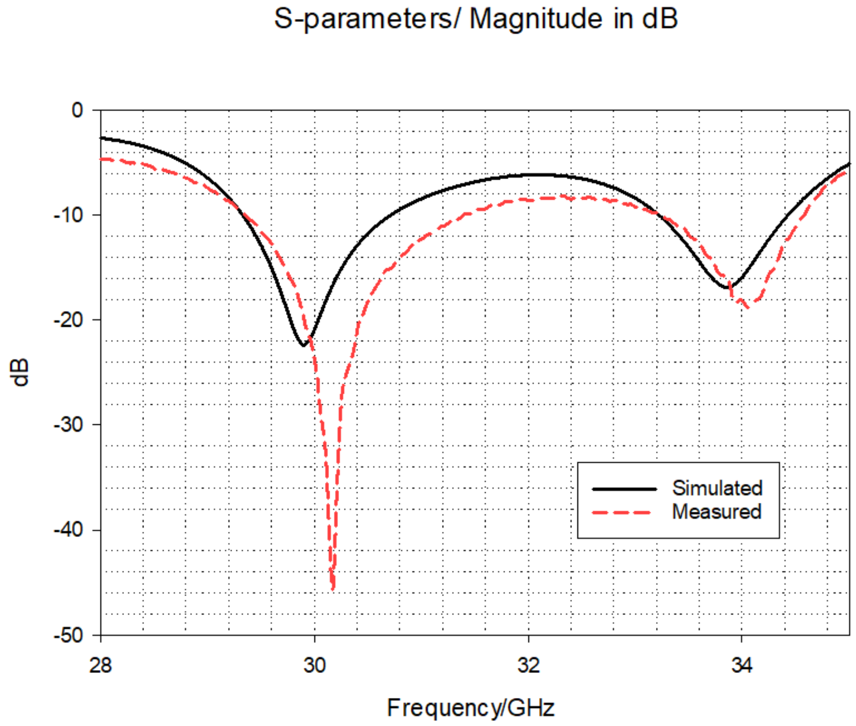

Figure 4.22: Scattering parameters

4.9.4 Antenna radiation pattern and axial ratio

Since the antenna array considers CP, it is important to study particularly its radiation patterns given by E_R and E_L, emphasizing on E_R, thus implying a RHCP on the antenna.

Fig. 4.23 demonstrates the comparison between the simulated and measured radiation patterns at 30 GHz for the Elevation planes at $\phi= 0$ ° and $\phi= 90$ ° with close agreement between measurements and simulation. At the same time, it presents the E_R and E_L patterns, demonstrating that the prototype is constituted by a RHCP with a unidirectional beam oriented at the Elevation plane on $\phi= 0$ °.

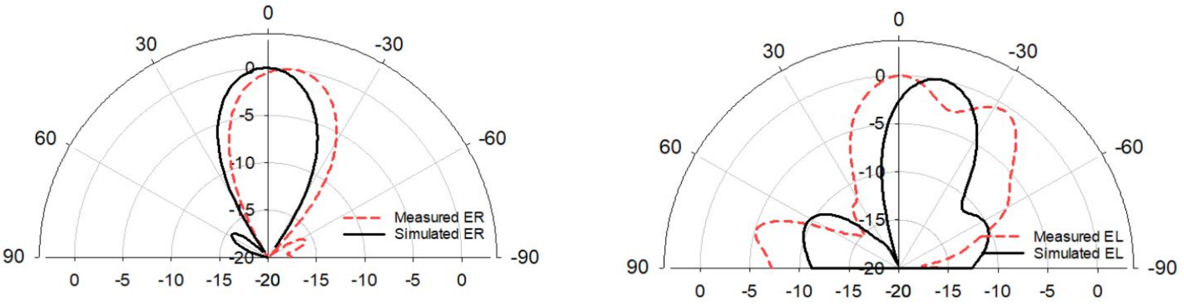

(a) E_R, 30 GHz at $\phi= 0$ °

(b) E_L, 30 GHz at $\phi= 0$ °

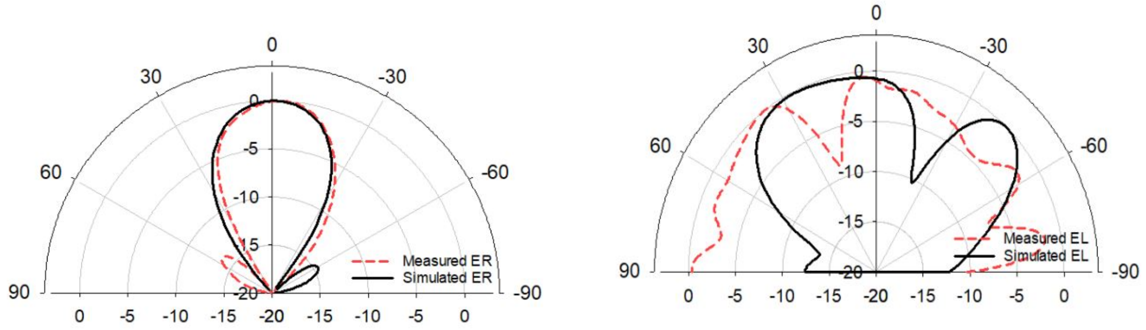

(c) E_R, 30 GHz at $\phi= 90$ °

(d) E_L, 30 GHz at $\phi= 90$ °

Figure 4.23: Measured and simulated radiation elevation patterns E_R at 30 GHz at $\phi= 0$ °

The same previously made comparison occurs at 34 GHz in Fig. 4.24 demonstrating good agreement with the simulated results and RHCP.

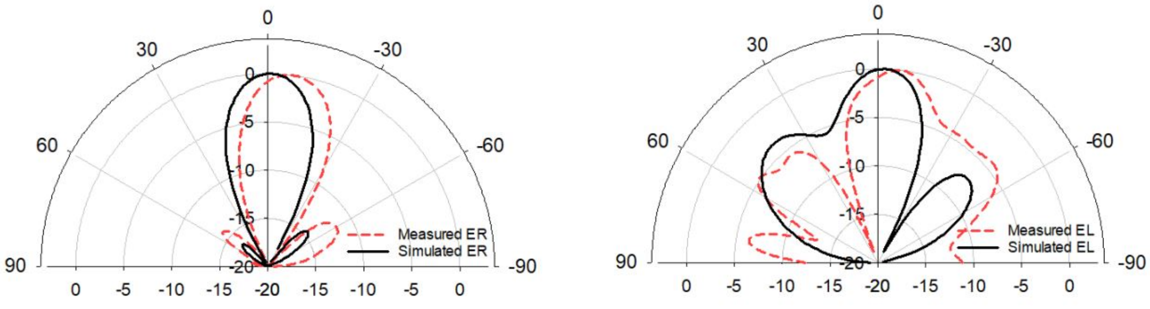

(a) E_R, 34 GHz at ϕ= 0 °　　(b) E_L, 34 GHz at ϕ= 0 °

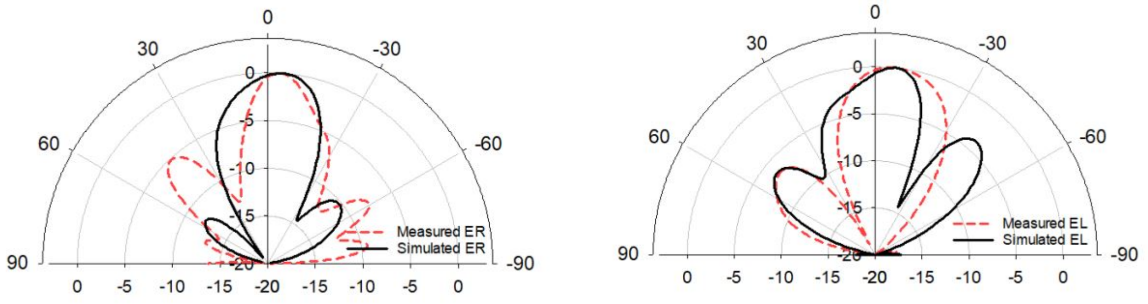

(c) E_R, 34 GHz at ϕ= 90 °　　(d) E_L, 34 GHz at ϕ= 90 °

Figure 4.24: Measured and simulated radiation elevation patterns E_R at 34 GHz at ϕ= 0 °

The gain and CP, analysed as AR <3 dB, are presented in Fig. 4.25. The simulated average gain ranges from 28 to 35 GHz is 13.7 dBi, compared with an average measured gain of 13.85 dBi demonstrating an excellent agreement. The 3dB measured AR bandwidth of the antenna is 10.16%.

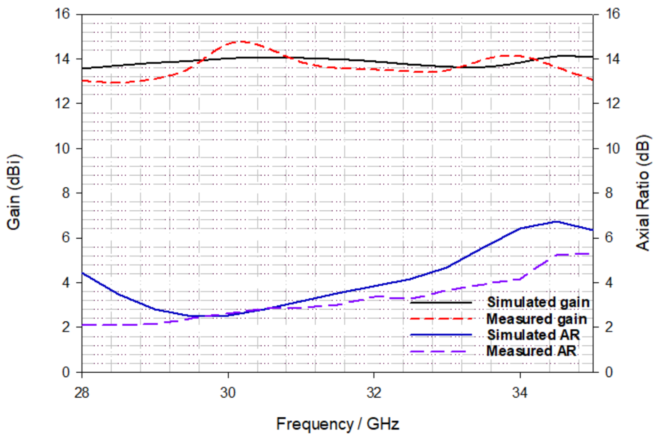

Figure 4.25: 3D radiation pattern at the resonant frequency

For complementing the 2D analysis, Fig. 4.26 shows the entire plot of the antenna array radiating in z-direction. The antenna simulation demonstrates unidirectional radiation with a directivity of 14.4 dBi at the resonant frequency.

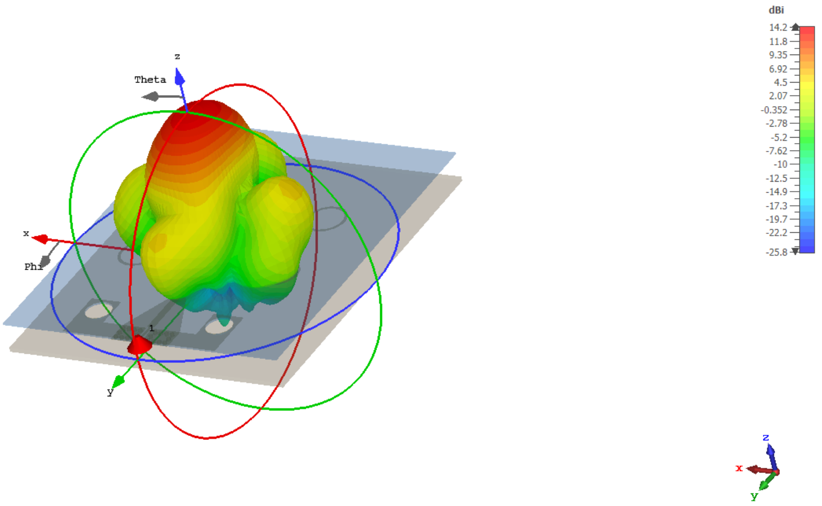

Figure 4.26: Simulated 3D radiation pattern at the resonant frequency

4.10 Open loop antenna array in a MIMO system

Due to the potential of the proposed work as a single element, the array design was considered to be researched as a MIMO system. Based on [114], two iterations were added to the antenna, the first one, by mirroring two antenna elements and the second one by repeating the same exercise but with four antenna elements. The aims of the system designs were focused on obtaining considerable isolation through elements and naturally splitting the beam radiation as a result of the isolation techniques which are described below, preserving at the same time the good performance of the single array.

The first applied isolation technique consisted of the positioning of the arrays. Two elements were located with a distance of $2.4\lambda_0$ from centre to centre of the arrays. As an initial test, the isolation between inter elements S_{12} and S_{21} at the resonant frequency was -37.3 dB. The Impedance bandwidth presented was 5 % in addition to a maximum realized gain of 13.6 dBi. Moreover, the CP on the main lobe radiation direction of both arrays was lost.

The second isolation technique, consisted of adding symmetric squares of dimension $0.2\lambda_0 \times 0.2\lambda_0$, on top of the substrate to disturb the E-field, to split the radiation pattern direction. The inter port reflection coefficient increased to -27.8 dB at the resonant frequency, which at the same time suffered a shift of 100 MHz up in frequency. Regarding the Impedance bandwidth of the system, it was reduced to 4.71 %. Realized gain was reduced to 13.3 dBi and the CP disappeared.

As the third isolation technique, a meandered line was investigated on top of the substrate based on [115]. The resonant frequency and impedance bandwidth were preserved compared with the original design. The isolation in between inter elements S_{12} and S_{21} at the resonant frequency was -44.15 dB. Despite the two antennas being located one in front of the other, the radiation was split due to the isolating technique illustrated in Fig. 4.27, which at the same time contributes to a realized gain of 15.2 dBi. The axial ratio <3dB from the open loop antenna array is preserved for this structure.

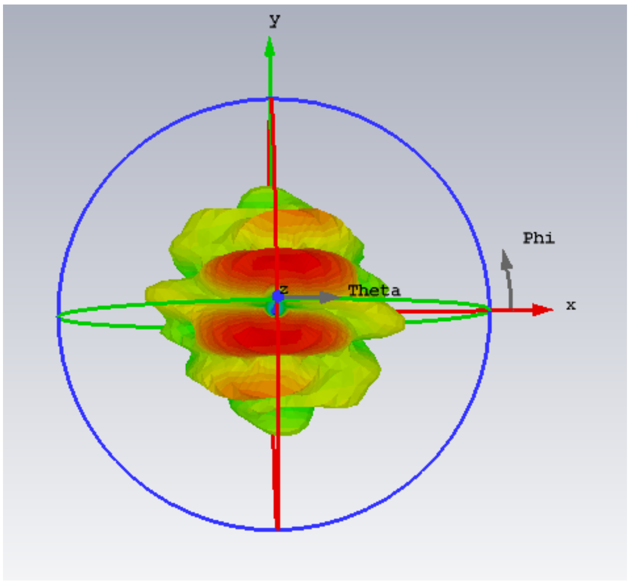

Figure 4.27: Simulated four port MIMO radiation pattern

Four antenna open loop arrays were investigated in a common GP, and the distance from centre to centre of each antenna was $2.4\lambda_0$. The resonant frequency of the system is 30 GHz with an Impedance bandwidth of 4.65%. The maximum realized gain in the main lobe radiation direction was 10.8 dBi. The isolation through the ports S_{12}, S_{21}, S_{34}, S_{43} ranges in -35 dB as a maximum value. Ports S_{13}, S_{31}, S_{14}, S_{41}, S_{23}, S_{32}, S_{24}, S_{42} present an isolation of -51 dB. This particular scenario does not contemplate any additional isolation technique. The axial ratio in the direction of the main lobe radiation was 3.59 dB.

A cross sequence of circular slots of diameter $0.05\lambda_0$ were located at the bottom within the GP. From the back view, a diagonal sequence of circumferences with a spacing of 1 millimetre. The isolation through the ports S_{12}, S_{21}, S_{34}, S_{43} ranges in was -42.6 dB as a maximum value within the frequency range. Ports S_{13}, S_{31}, S_{14}, S_{41}, S_{23}, S_{32}, S_{24}, S_{42} present an isolation of -46.5 dB. The system comprises an impedance bandwidth of 5.31 % with a resonance frequency of 30GHz. The antenna's realized gain is 14.2 dBi. It can be observed in Fig. 4.28 the formation of four individual unidirectional radiation beams. Axial ratio < 3dB was preserved by simulation as 4.7 % on the main lobe radiation direction.

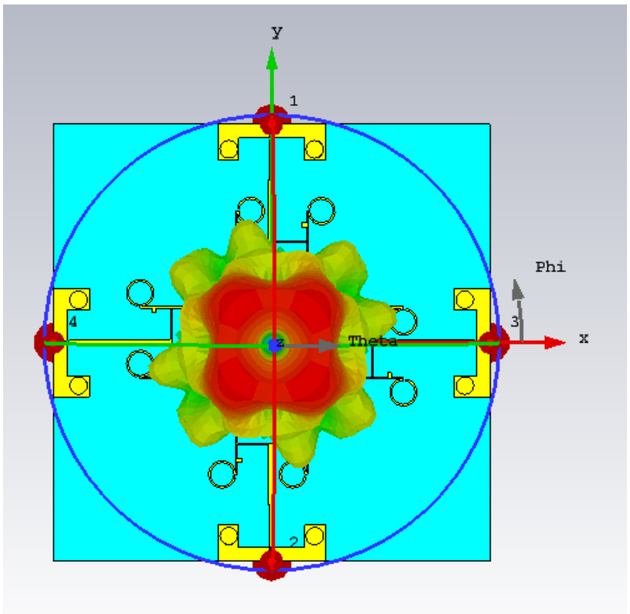

Figure 4.28: Simulated four port MIMO radiation pattern

Two millimetre diameter square slots were added on top and bottom of the antenna to reduce the isolation between elements. Both of them were aligned, from the top of the antenna as circular copper shapes, from the bottom as etched holes within the GP. The resonant frequency and impedance bandwidth were preserved at 30 GHz, and the realized gain of the system was 12.6 dBi. The isolation through the ports S_{12}, S_{21}, S_{34}, S_{43} ranges in -48.07 dB as a maximum value. Ports S_{13}, S_{31}, S_{14}, S_{41}, S_{23}, S_{32}, S_{24}, S_{42} present an isolation of -39 dB.

Another utilised technique consisted of adding a T-stub inside the open loop of each one of the arrays, corresponding to the top and bottom layers of the radiators. By adding the stubs, it was noted that the Impedance bandwidth increased to 6.82 % with a shift in frequency of ∼1 GHz compared to the single element S-parameters antenna array reference results. The maximum achieved realized gain for this case was 17.3 dBi. Regarding the isolation between ports, S_{12}, S_{21}, S_{34}, S_{43} ranges in -35 dB as a maximum value. Ports S_{13}, S_{31}, S_{14}, S_{41}, S_{23}, S_{32}, S_{24}, S_{42} present an isolation of -47dB. Circular polarisation was not preserved in this case.

4.11 Conclusions

Three iterations of the open loop antenna array and the fabricated design have been discussed in this chapter. The first one consisted of a double sided open loop antenna with a realized gain of 8.54 dBi, an impedance bandwidth of 3.73 %, a resonant frequency of 55 GHz, and an AR <3dB of 11%. The second iteration consisted of a two double sided open loop radiations addition as well as a T-junction with an increased gain of 11 dBi. It exposes an impedance bandwidth of 4.61%, with a resonant frequency of 53 GHz, and an AR $<$ 3 dB of 10.80 %. The third iteration contemplated another couple of open loops to the array with an additional T-junction for the summing network. This iteration shows a 13.8 dBi gain. Its impedance bandwidth is 5.05 %, with a resonant frequency of 55 GHz, and an AR <3 dB of 9.03 %. Finally, the design was scaled for working with a $\lambda_0 = 10$ mm which resulted in a dual-band array with resonant frequencies at 30 and 34 GHz. Its impedance bandwidth was 4.60% with a gain of 13.7 dBi, and an axial ratio $<$ 3 dB of 10.16%. Further tests were investigated via simulation with the fabrication characteristics for a MIMO system. The isolation results for two elements were successful for the case of the meandered line technique with a reduction of -44.15 dB, preserving CP and achieving at the same time a gain of 15.2 dBi. The four element scenario designs were unsuccessful, despite the reflection coefficient values obtained in between ports being lower than -20 dB, the four radiation beams were not split in the four intended directions due to the coupling in between antenna arrays. Designing a one-layer structure, and adding repeated two layers isolating techniques are some suggested further tests for tackling the unwanted behaviour and taking advantage of the potential design. The observed high directivity, gain, and circular polarization, coupled with the design's inherent characteristics, make the antenna array a promising candidate for IoT-based healthcare monitoring systems, specifically for an on-body architecture also because of its size. Circular polarisation mitigates polarisation mismatch losses, enhancing transmission reliability.

Chapter 5

Rectangular DRA MIMO at the C-band

Due to fabrication drawbacks for MIMO systems, an alternative antenna architecture is investigated throughout this chapter. RDRA antennas claim simplicity and good performance in terms of high gain and circular polarisation presence. Additionally, the reflection coefficients, S-parameters, are a key parameter to understand the reduction of mutual coupling between antenna elements. The following sections will present the proposed RDRA designs working at C-band, 4 to 8 GHz frequency, methodology and results of a single element followed by the corresponding analysis with four antenna elements in a MIMO structure.

5.1 Single RDRA element for C-band

The initial antenna was designed with a resonant frequency of 4.6 GHz, i.e. $\lambda_0 = 65$ mm. The antenna design substrate material was chosen as Rogers RT5880 with $\epsilon_r = 2.2$, size of $0.97\lambda_0 \times 0.97\lambda_0$ and a thickness of 1.5 mm. The copper layers have a thickness of 35 μm. The radiating termination of the strip line consists of a rhombus shaped strip as presented in Fig. 5.1a, the larger diagonal is $0.296\lambda_0$, the smaller diagonal is $0.157\lambda_0$. The RDRA is made of Alumina $\epsilon_r = 9.9$ and its dimensions are $0.153\lambda_0 \times 0.153\ \lambda_0 \times 0.307\lambda_0$. Fig. 5.1b illustrates the antenna design with all the antenna components from an upper perspective.

5.1.1 Fabrication considerations

As a general consideration, the studied designs were simulated using CST Studio Suite, fabricated and measured at the University of Sheffield facilities; either at the X-band or the UKVI millimetre wave laboratory.

The initial antenna is made of multiple parts. The first one refers to the Printed Circuit

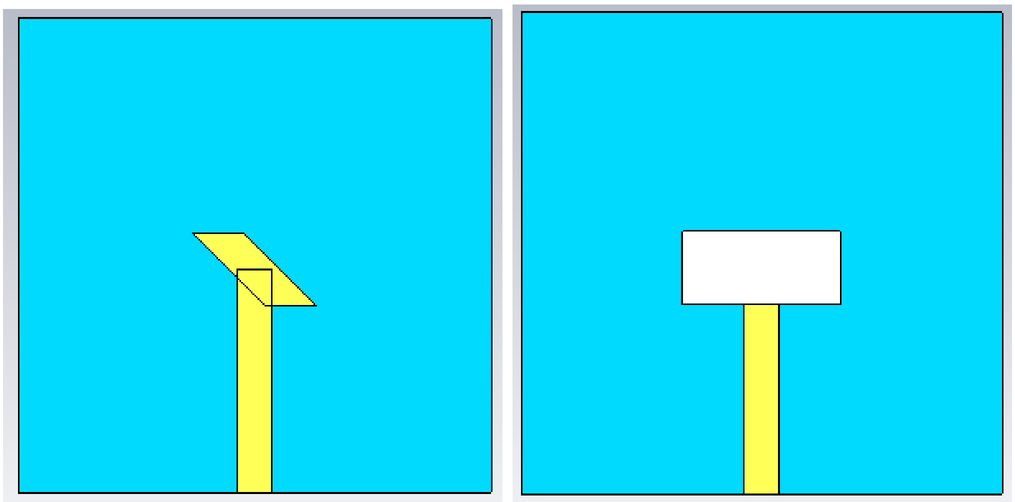

(a) Antenna design without the DR (b) Antenna design with the DRA

Figure 5.1: Antenna design with the DRA

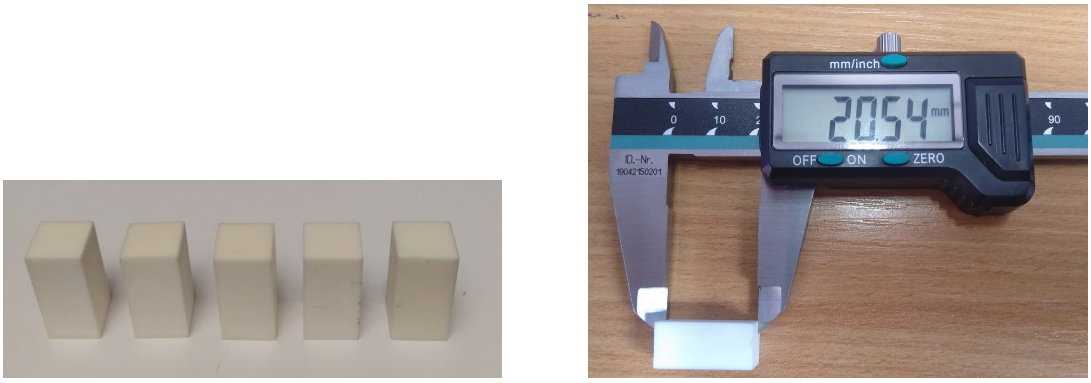

(a) Rectangular ceramic pieces (b) Ceramic piece measured size

Figure 5.2: Ceramic rectangular resonator

Board (PCB) structure, which consists of the transmission line and radiator. The second section refers to the Alumina ceramic resonator, which will complement the first part of the antenna. Fig.5.2a shows the Alumina pieces.

The ceramic radiators were first measured, as illustrated in Fig. 5.2b which presents the fabrication tolerances for the samples, resulting in the tolerances shown in Table. 5.1.

Table 5.1: Ceramic resonator tolerances

Variable name	dimension (Δmm)
width (a)	0.05
length (c)	0.1
thickness (b)	0.5
permittivity	1

The antennas were assembled by aligning the DRA precisely so that it is in the geometrical middle of the rhombus as previously mentioned. Fig. 5.3 illustrates the procedure.

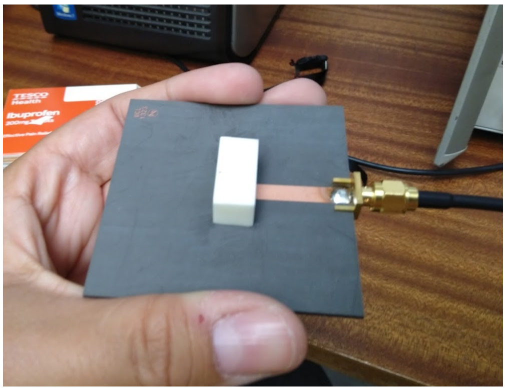

Figure 5.3: Assembled RDRA single prototype

5.2 Single RDRA design

5.2.1 S-parameters

The S-parameters for this case were measured. The conducted measurements consisted of a frequency span ranging from 4 to 6 GHz due to the impedance bandwidth. The measured impedance bandwidth represents a 5.66 % vs a 3.03 % of the simulated results, widening by 2.2% the antenna frequency range due to a reduction in reflections. The impedance bandwidth differences are attributed to lateral gaps between the transmission line and the ceramic resonator, in addition to its alignment. Fig. 5.4. shows a comparison between the measured and the simulated results of the single antenna.

5.2.2 Antenna radiation pattern

Figs. 5.5 and 5.6 shows the right and left components, respectively, at the resonant frequency of the single antenna element. The simulations and measurements are in good agreement. These results show that the DRA offers right-hand CP (RHCP) radiation since E_R is greater than E_L by more than 10 dB.

5.2.3 Antenna gain

The antenna gain measurements were taken in the anechoic chamber in two scenarios. The first one contemplated the horn antenna of the model R&S HF906 located in LOS with the proposed AUT, and the second one considered two horn antennas of the same type positioned in LOS. Based on this logic, the horn antennas acted as a reference so that the gain could

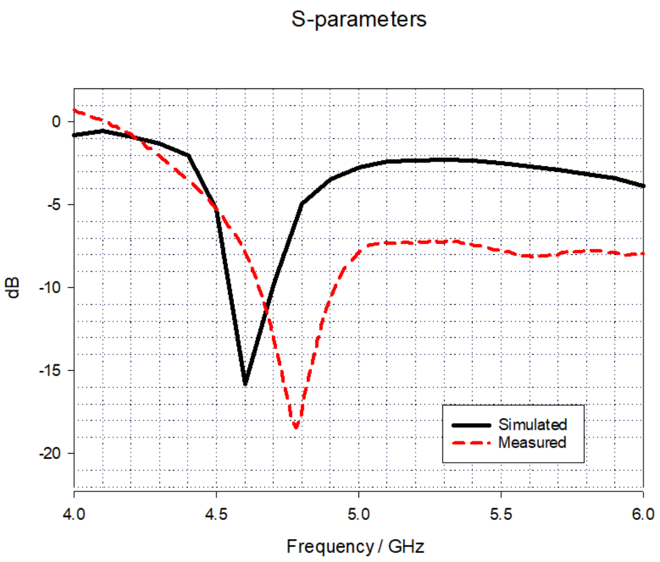

Figure 5.4: S-parameters RDRA

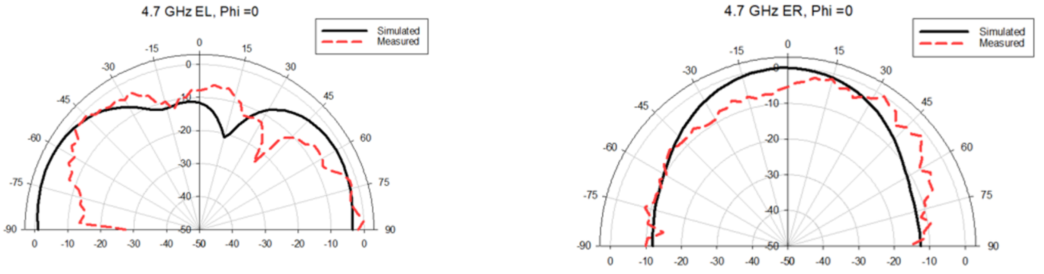

(a) E_L

(b) E_R

Figure 5.5: Measured and simulated radiation elevation patterns at 4.7 GHz at ϕ= 0 ° and ϕ= 90 °

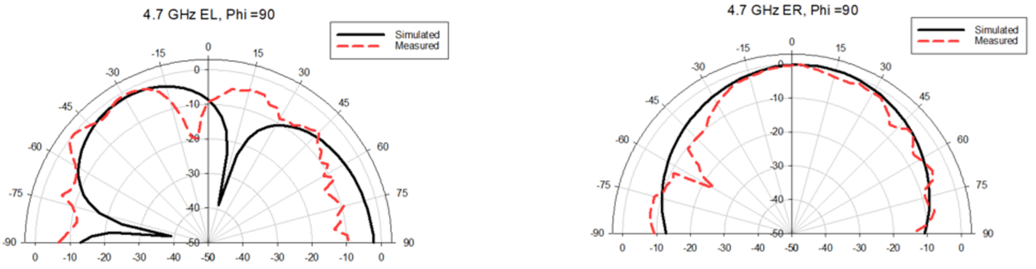

(a) E_L

(b) E_R

Figure 5.6: Measured and simulated radiation elevation patterns at 4.7 GHz at ϕ= 0 ° and ϕ= 90 °

be measured. Fig. 5.7 presents the measured and simulated Gain of the AUT which is approximately 7.03 dBi.

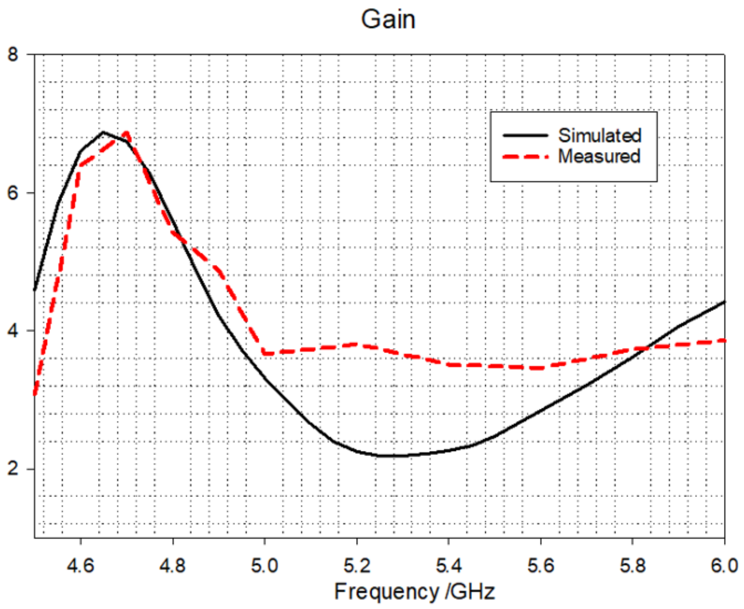

Figure 5.7: RDRA gain comparison

5.2.4 Axial ratio

In accordance with the antenna radiation patterns, the CP bandwidth overlaps the impedance bandwidth. The measured axial ratio is presented in Fig. 5.8 with a <3dB bandwidth of a 26.05 % which is in close agreement with the simulated axial ratio bandwidth.

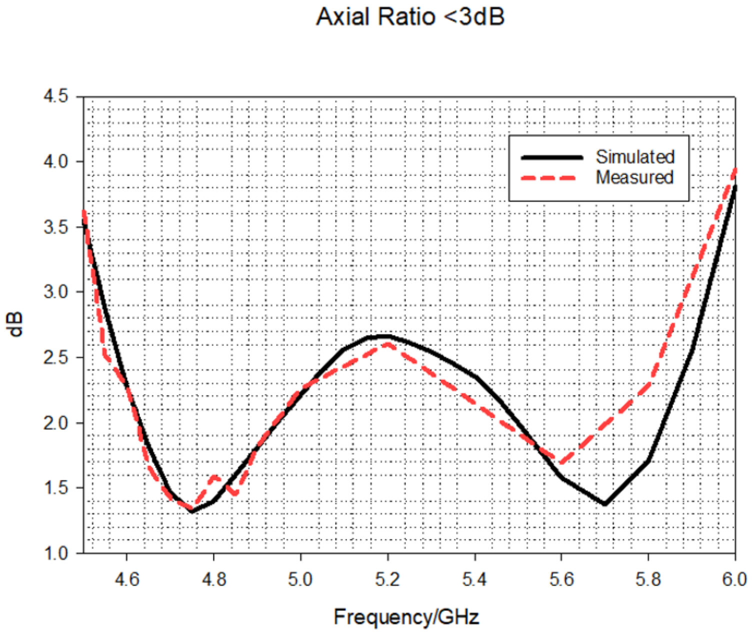

Figure 5.8: Simulated and measured axial ratio

5.2.5 Four element RDRA design

Once the single RDRA was measured and analysed, the MIMO system was introduced based on the single element design considerations. The substrate material consisted of a Rogers RT5880 with $\epsilon_r = 2.2$, size of $1.9\lambda_0 \times 1.9\lambda_0$ and substrate thickness of 1.57 mm. The conductive elements are fabricated using copper with a thickness of 35μm. The antenna system considered four RDRA elements positioned at different azimuthal angles of 0 ° , 90 ° , 180 ° and 270 °. The centre to centre distance between RDRA's is approximately 0.976 λ_0.

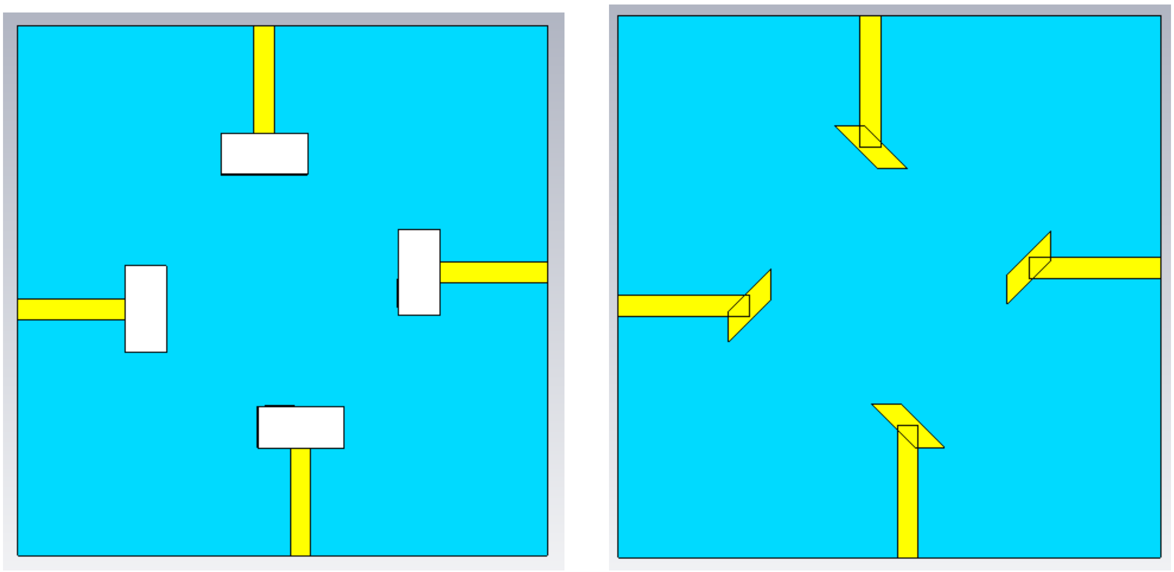

(a) Four element design with RDRA

(b) Four element design without RDRA

Figure 5.9: MIMO structure

There are two main strategies employed throughout this work to reduce the mutual coupling between the MIMO elements. The first refers to the RDRA positions.

The second strategy refers to the use of diagonal slots etched into the Ground Plane of the antenna. They are rotated at a 30 ° angle. In the case of the main lobe radiation pattern direction, each one of the RDRA's are shifted 0.065 λ_0 from the substrate's centre as illustrated in Fig. 5.9a. Additionally, the four feeding mechanisms without placing the dielectric resonators are shown in Fig. 5.5a.

The antenna assembly procedure was the same as followed for one element. Fig. 5.10a. illustrates a top view of the assembled four element MIMO antenna. Similarly, the bottom view is illustrated in Fig. 5.10b.

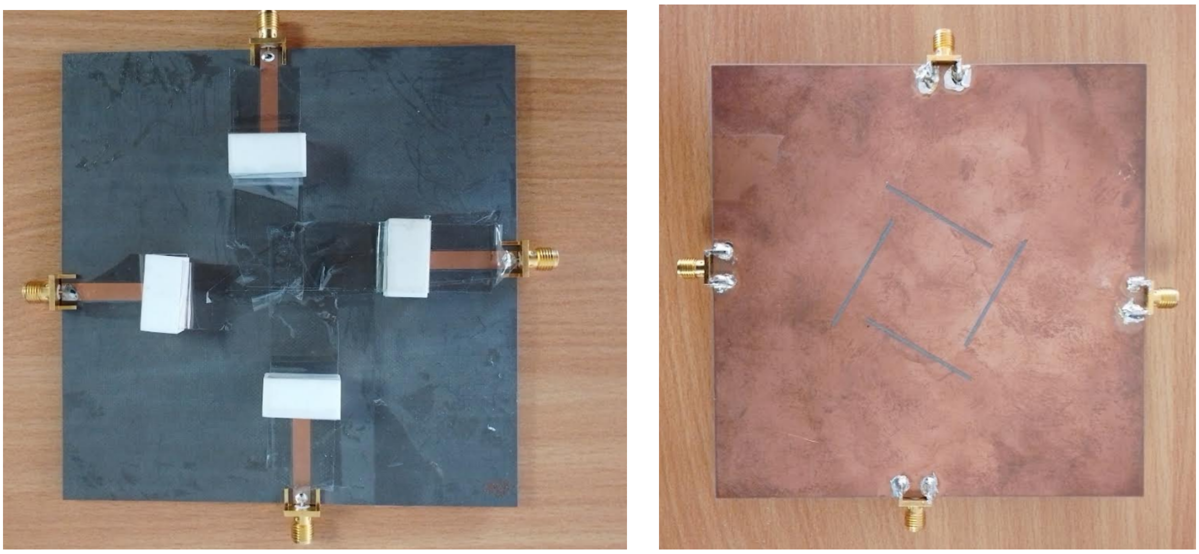

(a) Top view (b) Bottom view

Figure 5.10: MIMO DRA prototype

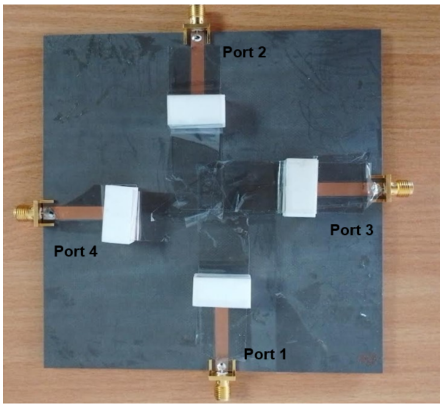

Figure 5.11: Antenna MIMO port distribution

5.3 Four element RDRA results

5.3.1 MIMO S-Parameters

After assembling the full antenna structure, the scattering parameters were measured according to the setup shown in Fig. 5.11. HP 8720B Network Analyzer with the two calibrated ports.

Based on Fig.5.11 labeling, ports 1 and 2 were connected to the VNA, while the rest of the ports were terminated by 50 Ω loads. This setup was considered for measuring S_{11}, S_{12}, S_{21}, S_{22} . Consequently, ports 3 and 4 were connected to the VNA and the rest of the unused ports were terminated with 50 Ω loads to avoid unwanted power losses, S_{33}, S_{34}, S_{43}, S_{44} were measured for this case. For the case of S_{13} and S_{31}, port 1 and port 3 were connected to the VNA. For S_{14} and S_{41}, port 1 and port 4 were connected to the VNA. For S_{23} and S_{32}, port 2 and port 3, were connected to the VNA. For S_{24} and S_{42}, port 2 and port 4, were connected to the VNA, leaving the rest of unused ports terminated with 50 Ω loads.

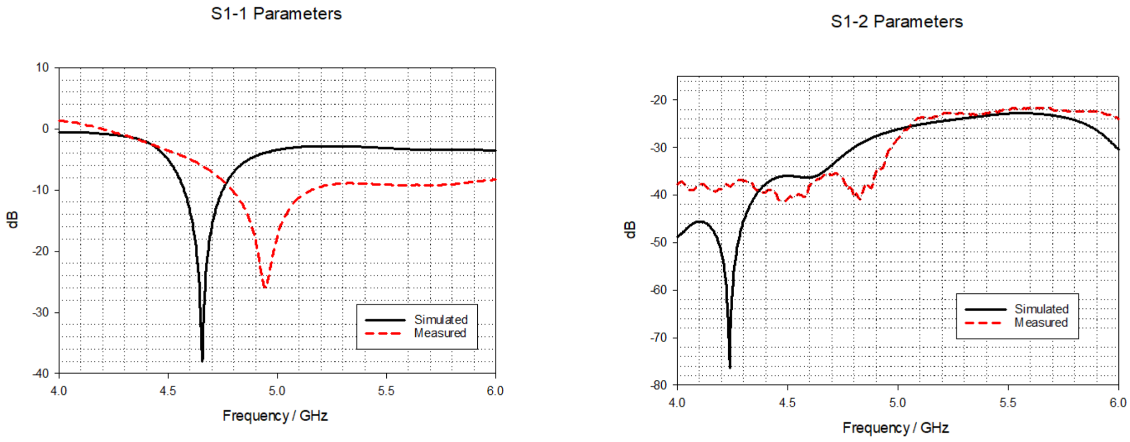

(a) S11 (b) S12

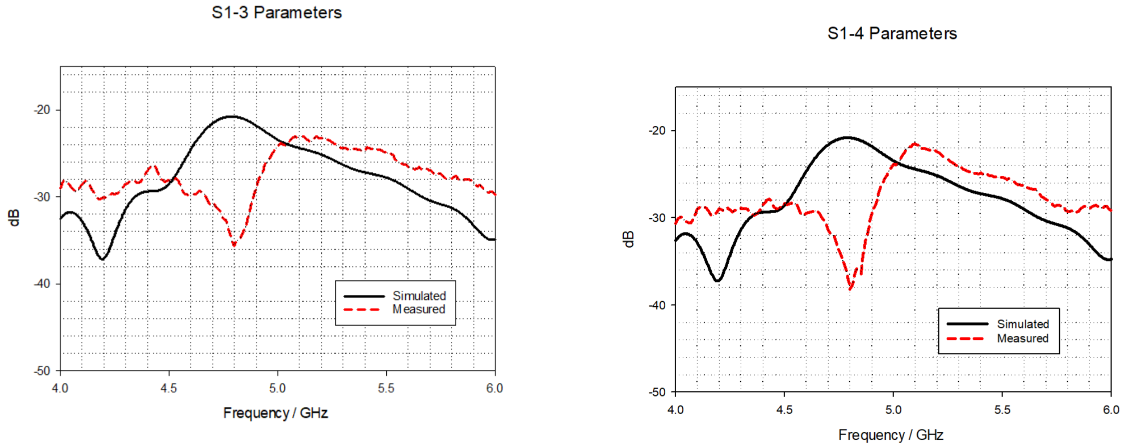

(c) S13 (d) S14

Figure 5.12: Scattering parameters when port 1 is fed.

Fig.5.12 illustrates a comparison between the simulated and measured scattering parameters throughout the four element architecture between port 1 and the other 3 ports. For the S_{11} measured results and in comparison with the simulated ones, there is a shift on the resonant frequency of approximately 3.15%, exposing an impedance bandwidth of 6.30 %. By comparing the single element and the four elements S_{11} cases, the simulated results propose a lower resonant frequency of 4.62 GHz. Concerning the measured results, there is an improvement in the impedance bandwidth of the MIMO system of 0.64 %. It is important to mention that the shift of the experimental antennas is due to minimum errors produced due to the dielectric resonator assembling alignment. Moreover, the radiator exposes uncertainties per se due to fabrication tolerances illustrated in Table 5.1. For the case of S_{12}, there is a good agreement between simulated and measured results. On the other hand, there is a reduction of coupling for about an approximate maximum of 15 dB for S_{13} and S_{14} within the impedance bandwidth, Figs. 5.12b, 5.12c, 5.12d illustrates particularly the differences.

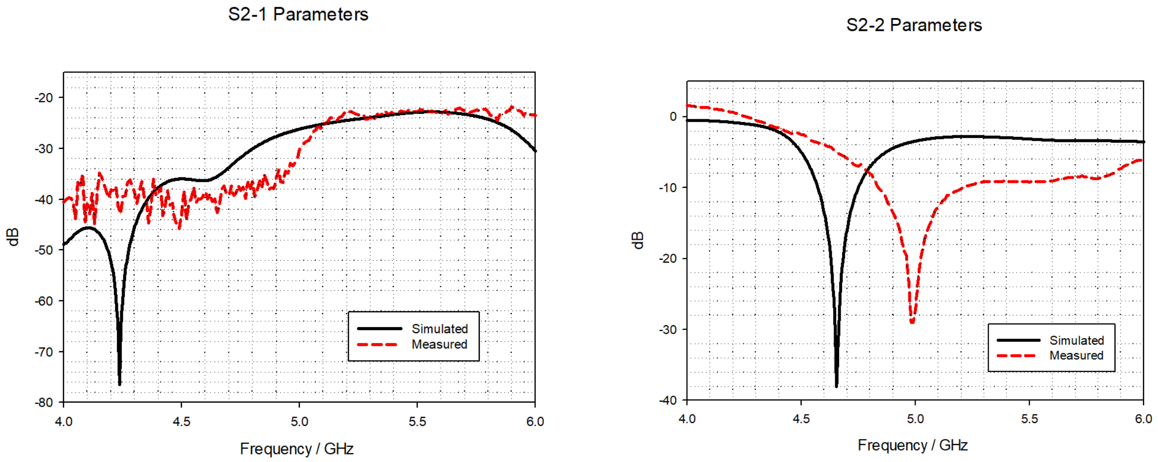

(a) S21 (b) S22

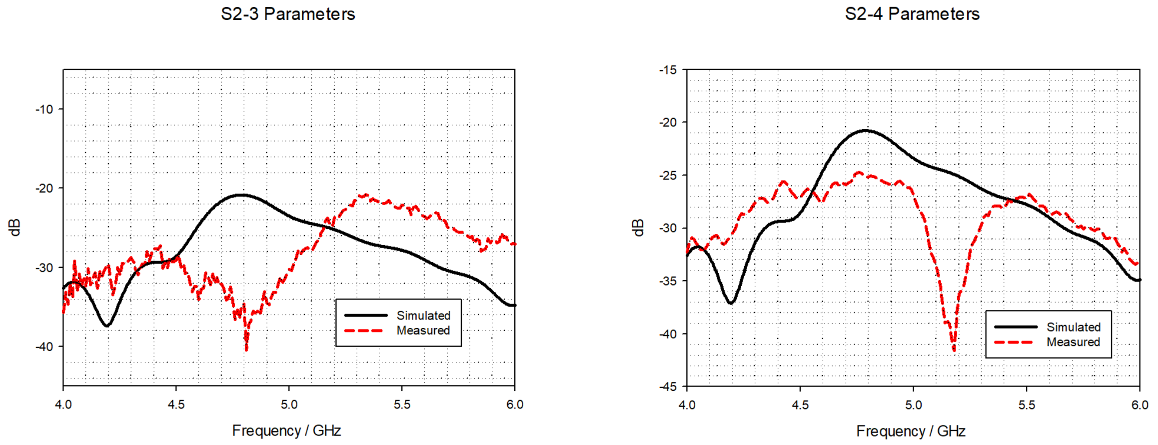

(c) S23 (d) S24

Figure 5.13: Scattering parameters when port 2 is fed.

Fig 5.13a presents a slight difference between simulated and measured results of a reduction of ∼ 9.47 dB within the impedance bandwidth frequency range, which at the same time can be attributed to an appropriate calibration of the VNA ports, in addition to the PCB fabrication precision. Fig. 5.13b presents a 3.65% simulated against a 7.42 % measured impedance bandwidth, this change can be attributed to the precision of alignment when assembling the radiator. In the case of Fig. 5.13c, a reduction of ∼ 18 dB in coupling was measured. Fig. 5.13d represents a lower maximum reduction in mutual coupling of ∼ 5 dB. At this point, and analysing the simulation results, it is important to mention that by design, the GP angled slots propose a reduction of 18 dB for Fig.5.13a, 3dB for Fig.5.13b, 4dB for Fig.5.13c and 10 dB for Fig.5.13d. The obtained results for port 3 of the system reported its mutual coupling value less than -20 dB which verifies the level of good isolation per each case.

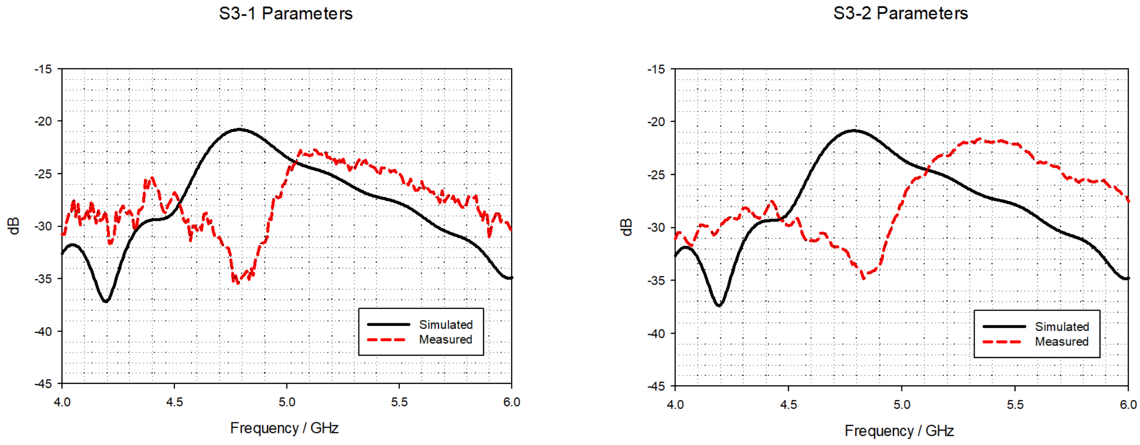

(a) S31 (b) S32

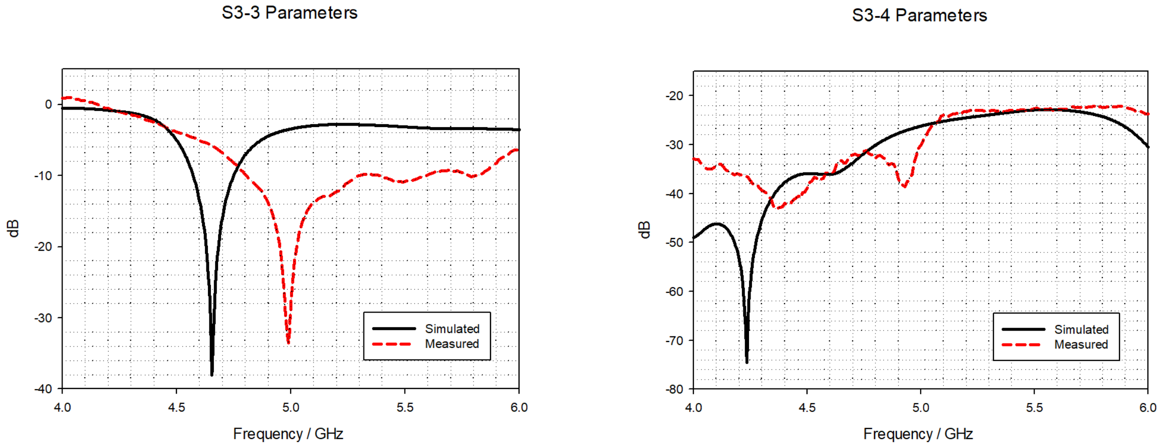

(c) S33 (d) S34

Figure 5.14: Scattering parameters when port 3 is fed.

Fig 5.14a presents a slight difference between simulated and measured results of a reduction of ∼ 14.62 dB within the impedance bandwidth frequency range, which at the same time can be attributed to an appropriate calibration of the VNA ports, in addition to the PCB fabrication precision. In the case of Fig. 5.14b, a reduction of ∼ 12 dB in coupling was measured. Fig. 5.14c presents a 3.65% simulated against a 9.61 % measured impedance bandwidth, this change can be attributed to the precision of alignment when assembling the radiator. Fig. 5.14d represents a lower maximum reduction in mutual coupling of ∼ 11 dB. The obtained results for port 3 of the system reported its mutual coupling value less than -20 dB which verifies the level of good isolation per each case.

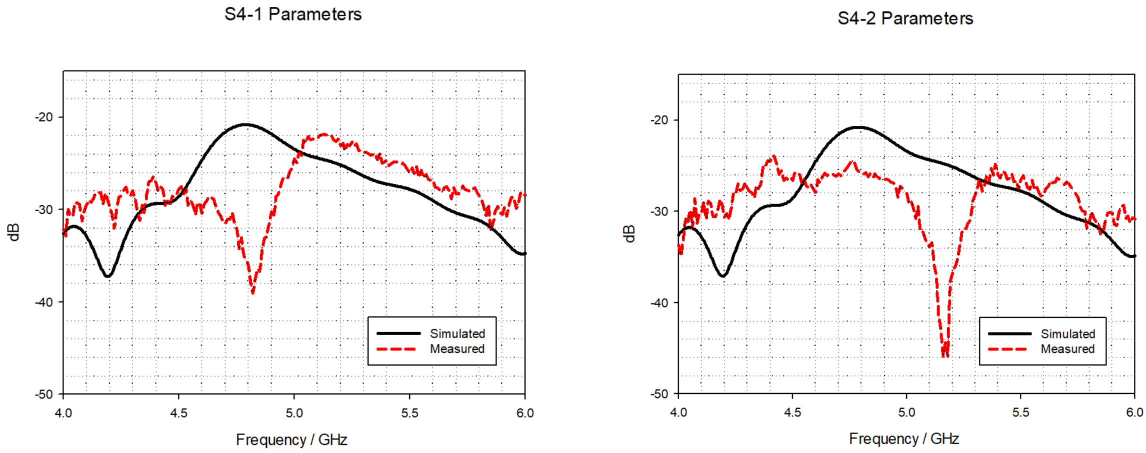

(a) S41 (b) S42

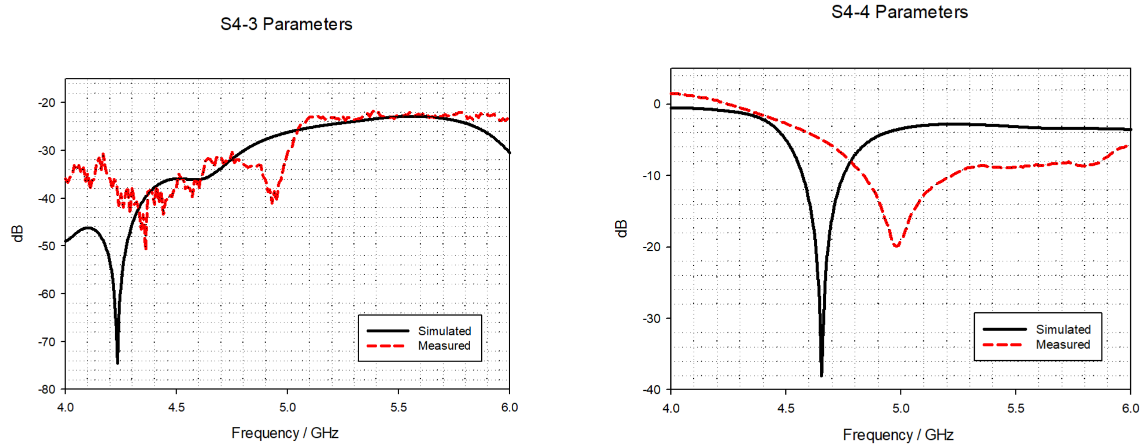

(c) S43 (d) S44

Figure 5.15: Scattering parameters when port 4 is fed.

Fig 5.15a shows the difference between simulated and measured results of a reduction of ∼ 18 dB within the impedance bandwidth frequency range, which at the same time can be attributed to an appropriate calibration of the VNA ports, in addition to the PCB fabrication precision. In the case of Fig. 5.15b, a reduction of ∼ 20 dB in coupling was measured. Fig.

5.15d presents a 3.65% simulated against a 7.63 % measured impedance bandwidth, this change can be attributed to the precision of alignment when assembling the radiator. Fig. 5.15c represents a lower maximum reduction in mutual coupling of $\sim$ 13 dB. The obtained results for port 3 of the system reported its mutual coupling value less than -20 dB which verifies the level of good isolation per each case.

As an overview of the MIMO return losses, there is a maximum shift in frequency of $\sim$ 7 % which is present due to the tolerances of the ceramic materials and the DRA's alignment. In the case of the parallel ports, the maximum measured coupling reduction was of 13 dB, and the perpendicular ports respectively of 20 dB which implies an improvement in the quality of the communication channel.

5.3.2 MIMO Radiation pattern

Analysis of multi-user MIMO antennas in terms of radiation pattern is presented in this section. The testing procedure contemplated the horn antenna R&SHF906 as a transmitter in LOS with a positioning of no more than $\frac{\lambda_0}{3}$ with the AUT and as a receiver. The AUT was connected to the HP 8720B Network Analyzer integrated into the 800F-10 system run by NSI-MI Technologies. An important consideration for the antenna testing inside the anechoic chamber is the antenna radiation pattern to be divided into four different structures. These structures will be explained in detail on each specific test using Fig. 5.11 MIMO ports arrangement.

Firstly, the MIMO system was fully scanned, and all ports were connected to the VNA via two 3-way splitters. This test emulated the entire MIMO system working at the same time and assuming a simultaneous transmission. The scan at the resonant frequency was determined with a cut at the Azimuth angle ranging from ϕ= -90 ° to ϕ= 90 °, the Elevation angle ranging from θ= -180 ° to θ= 180 °, to determine the direction of the maximum gain point illustrated in Fig. 5.17. The measured and simulated results present similar radiation patterns. At this point, it is relevant to consider that the radiation pattern main lobe directions will behave in the same way but in the complementary direction. The antenna mounting system for the MIMO design is presented in Fig. 5.16.

After determining the direction of the main beam from Fig.5.17, the following scans were made at θ= 42° to investigate the simultaneous beam radiation in four different directions. This time contemplating a 360 ° plane for studying the full radiation.

The antenna mounting system for the MIMO design is presented in Fig. 5.16. The VNA port was connected to a 3-way splitter to test two simultaneous ports and 2-3 way for the entire system. As an additional observation, the 4 elements antenna MIMO complete structure was located approximately $0.155\lambda_0$ away from the outer white acrylic layer, where the antenna is supported, as shown in Fig. 5.16.

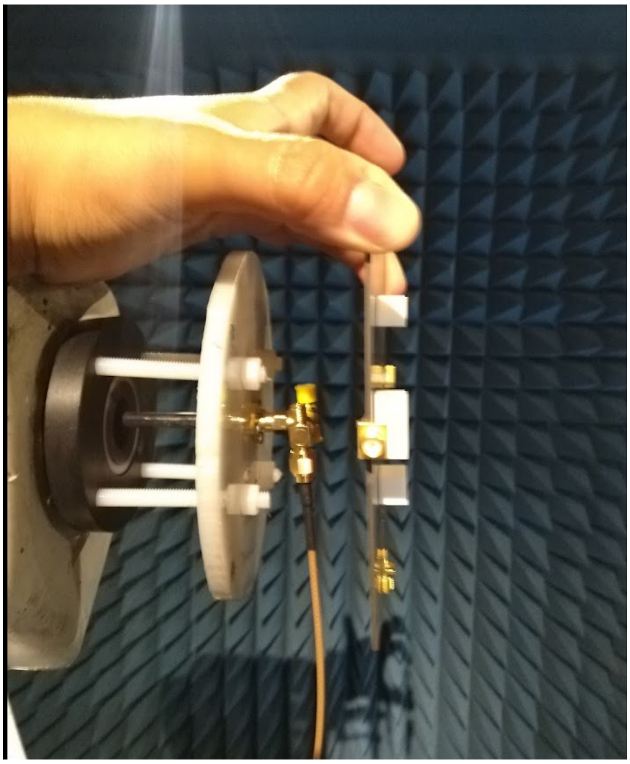

Figure 5.16: MIMO connection structure

Fig. 5.18 presents the antenna radiation patterns for an RHCP antenna at the resonant frequency in agreement with the left and right patterns of the simulation. Fig.?? shows a main lobe radiation at -40° due to antenna's behaviour when shift it from the middle board position by 0.976 λ_0 to the right.

For the second case, the general testing setup of the transmitter and receiver remains the same. The 1^{st} and 2^{nd} RDRA antennas, connected to ports 1 and 2 were input to the VNA and antennas 3 and 4 were terminated at 50 Ω according to Fig. 5.11. For this case, the radiation pattern was expected to be split in two symmetric halves concerning zero degrees shown in Fig. 5.19b. It can be seen that the positioning of the antennas contributes to the isolation between them due to the split of the beam, which is illustrated in Fig.5.22.

For the third case, the RDRA ports labelled as 1 and 3 were connected to the VNA, and antennas 2 and 4 were terminated with 50 Ω loads. Fig.5.19 presents the measured E_L and E_R at 4.65 GHz with good agreement with simulations. From the E_R, it is important to mention that the adjacent feeding ports present a radiation pattern split into two beams at 60 ° and -180 °. As can be shown in Figures 5.18, 5.19 and 5.20, the RDRA radiates on a lateral right side with the structure.

The two 3-way splitters were connected to the VNA port for the final case. This test is to emulate the entire MIMO system working simultaneously and assuming a simultaneous transmission. It is intended to prove the four independent antenna radiation due to its

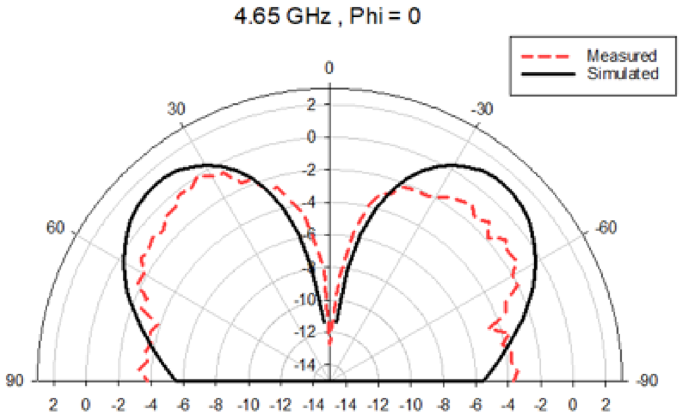

(a) ϕ= 0°

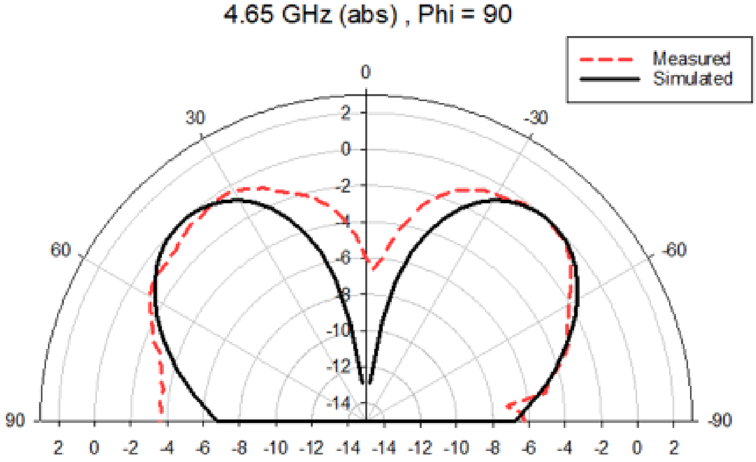

(b) ϕ= 90°

Figure 5.17: Measured and simulated radiation pattern magnitudes at 4.65 GHz

common substrate, GP and spacing between elements. Fig. 5.21 shows clearly four different beams, the first one radiating to the direction of 30°, the second one to 150°, the third one to 240° and the last one to 300° within a 0 to 360° scale.

Based on the radiation patterns presented in Fig. 5.21, the 3D radiation pattern scans were reconstructed with Matlab R2022b and are displayed in Fig. 5.22. It can be seen that the antenna radiated in four different independent directions. This behaviour was achieved by the positioning of the four antenna elements in the substrate. Fig. 5.22 demonstrates the MIMO system propagation in the z-direction, according to the coordinate system shown in the figure, with four beam lobes observed from the Elevation angle at 30°, 150°, -120°, -60° within a 0 to 360°.

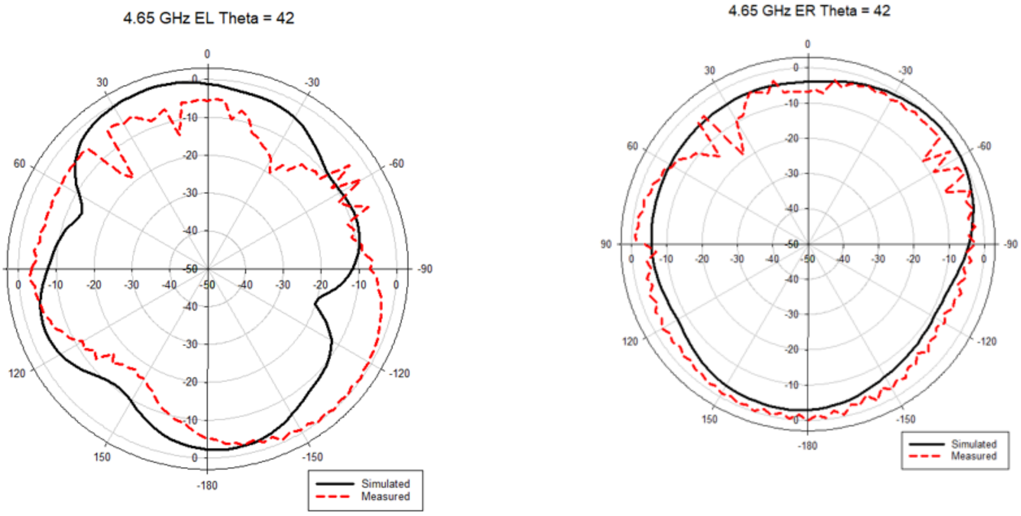

(a) E_L (b) E_R

Figure 5.18: One port feeding measured and simulated radiation elevation patterns at 4.65 GHz at $\theta = 42$ °

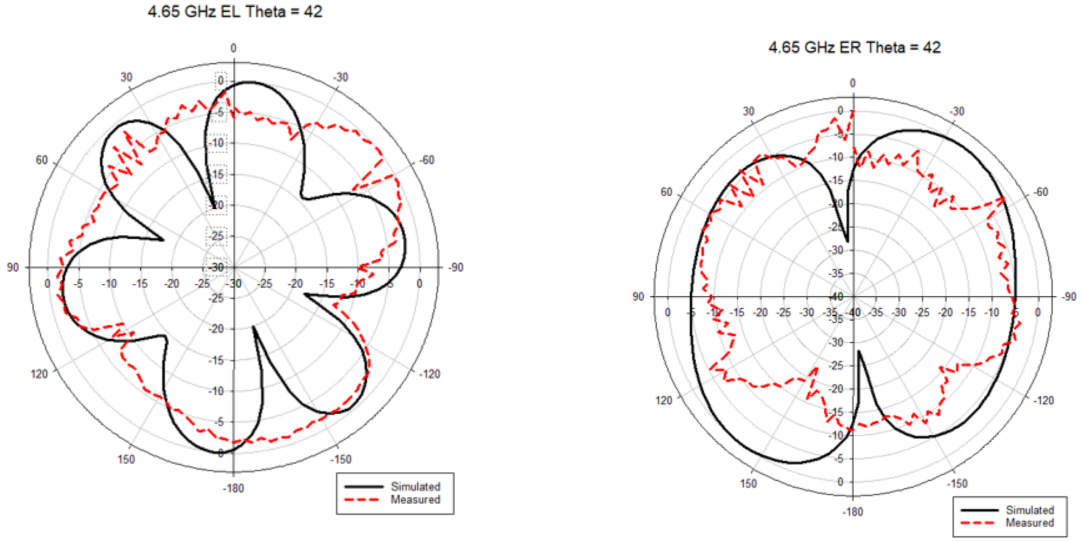

(a) E_L (b) E_R

Figure 5.19: Two parallel port feeding measured and simulated radiation elevation patterns at 4.65 GHz at $\theta = 42$ °

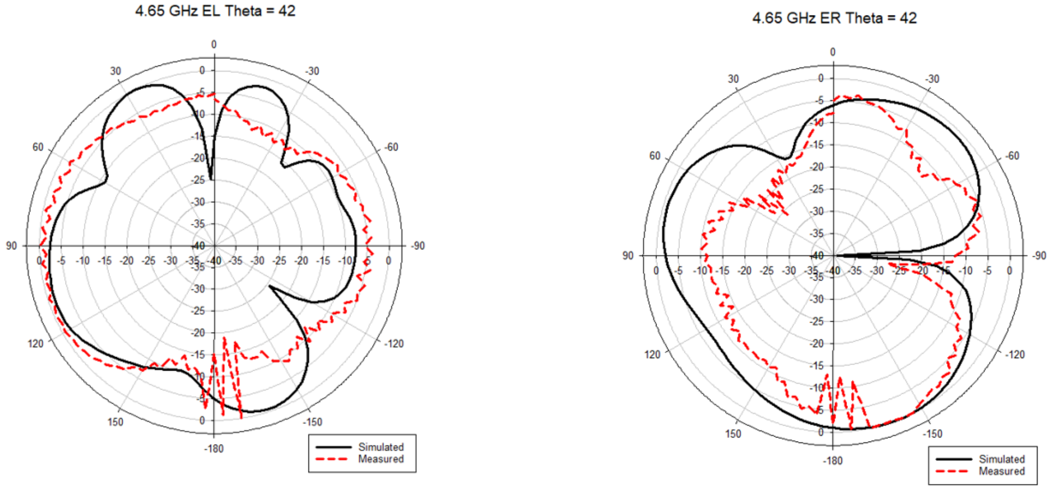

(a) E_L (b) E_R

Figure 5.20: Two perpendicular port feeding measured and simulated radiation pattern at 4.65 GHz at $\theta = 42$ °

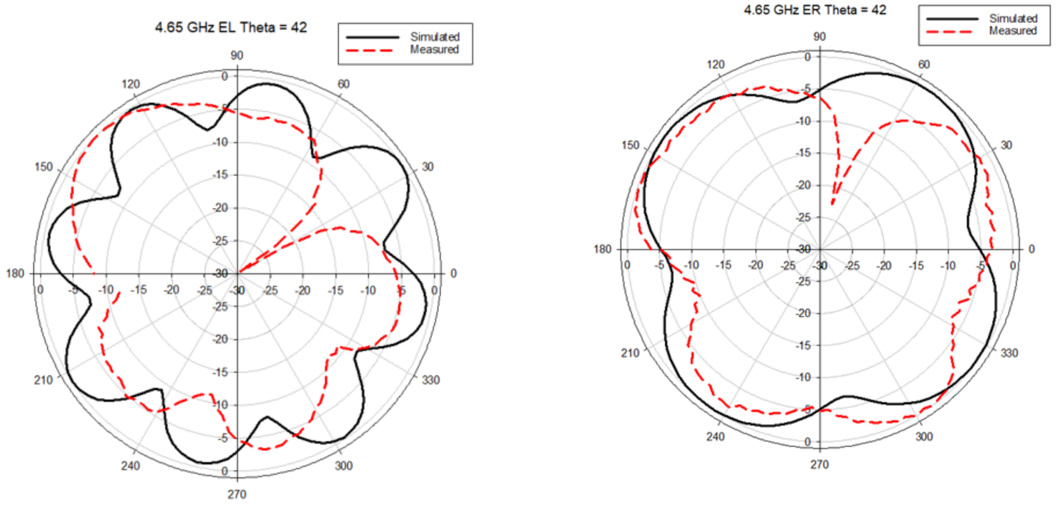

(a) E_L (b) E_R

Figure 5.21: MIMO antenna architecture measured and simulated radiation pattern at 4.65 GHz at $\theta = 42$ °

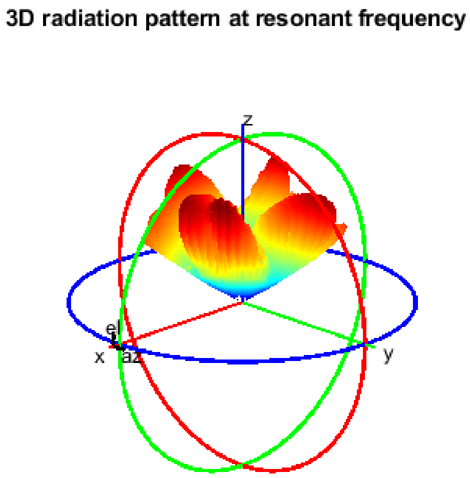

Figure 5.22: Simultaneous feeding MIMO 3D radiation pattern

5.3.3 MIMO Gain

As indicated at the beginning of this chapter, some of the highlights about the DRA's is the capacity to achieve high gain in relation to a high efficiency due to the nature of the ceramic radiator. For the case of evaluating the gain on the MIMO system, firstly the maximum radiation point at the Elevation plane where the maximum antenna gain was found resulted at $\phi = 54°$ presented in Fig. 5.23. It is important to mention that the measurements resulted in a shift of around 10° different from the simulated values.

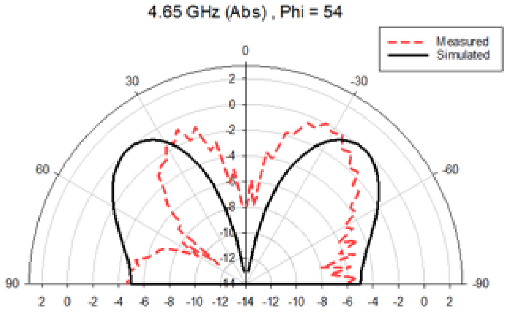

Figure 5.23: MIMO gain at cut angle of $\phi = 54$ °

The antenna system gain was determined in specific points within the impedance bandwidth range presented in the Scattering parameters results section. Fig. 5.24 shows the antenna maximum gain was determined based on the maximum radiation direction.

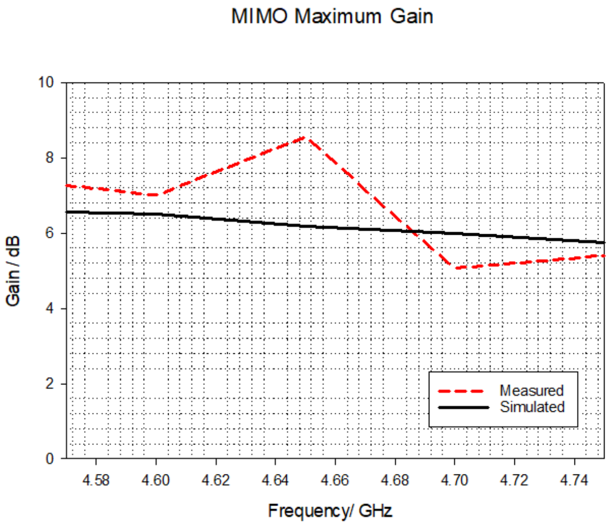

Figure 5.24: MIMO Gain

5.3.4 MIMO Circular polarisation

For the case of CP, the radiation of the main lobes was considered to determine the existence of AR < 3dB on the system. Some of the key considerations for the following results reside in studying four different angles for the antenna radiation. According with the previously presented results in Fig.5.25, the angles of interest are 55°, 146°, -33°, -124° respectively. It is quite important to consider the impedance bandwidth frequencies for acknowledging the overlapping with the CP within the entire system.

5.3.5 Envelope Correlation Coefficient and Diversity Gain

After studying the general performance of an antenna, the present MIMO architecture needs to be analysed and evaluated in a systematic environment. The first parameter to be presented is the ECC which, as mentioned in section 3.4.3, shows the independence of each antenna component. Fig.5.26 shows the interactions between the antenna system based on the labelling of Fig.5.11. For Fig.5.26a, the simulated values with CST presenting values of 0.0006 to 0.0013 at the resonant frequency. In case the of measured values, illustrated in Fig.5.26b, the values vary from < 0.005 to < 0.01 according to the frequency. According to [40] the maximum acceptable ECC value should be < 1 which is fulfilled by the present system.

As the complementary value for acknowledging the ECC, Diversity Gain measured results are presented in Fig. 5.27b showing values for DG12, DG13, DG14, DG23, DG24, DG34

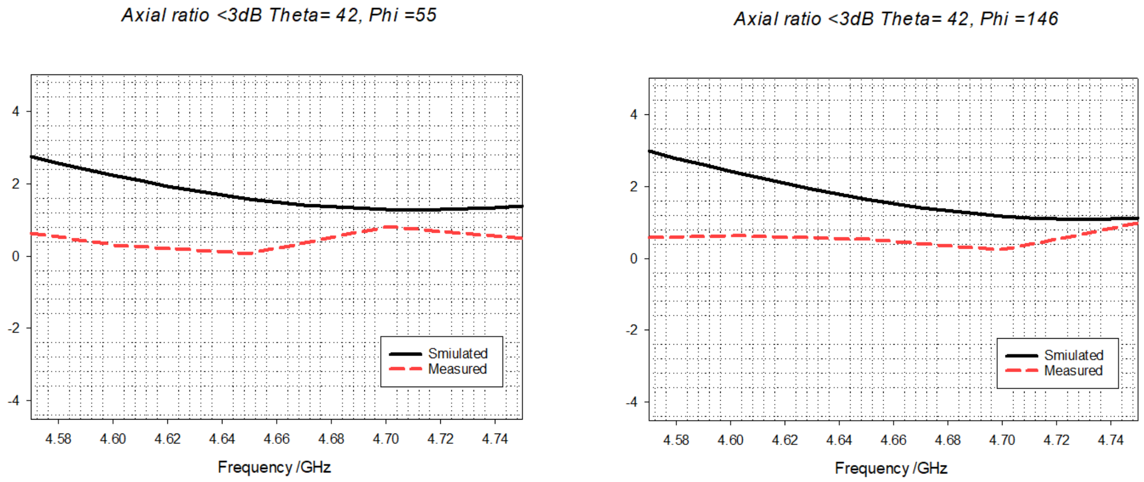

(a) ϕ= 55 °

(b) ϕ= 146 °

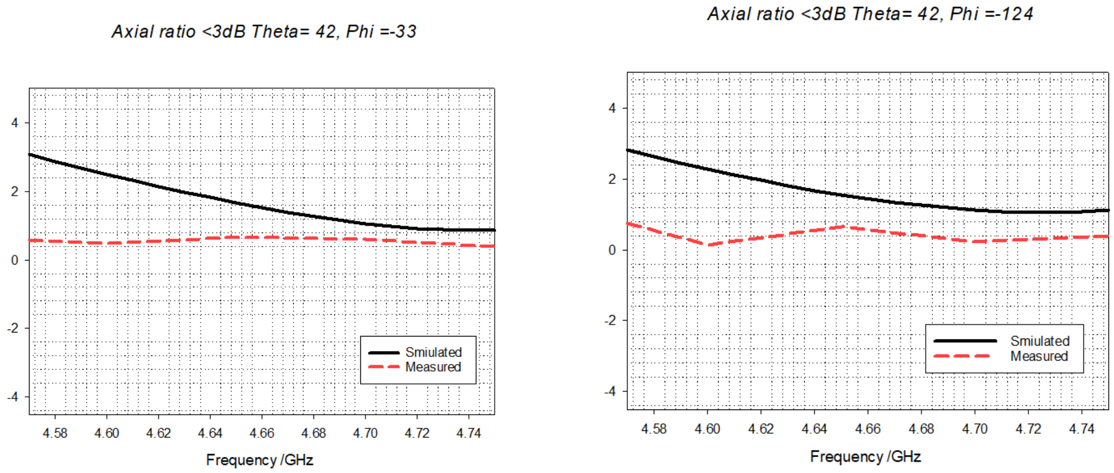

(c) ϕ= -33°

(d) ϕ= -124°

Figure 5.25: axial ratio < 3dB at θ= 42 °

not smaller than 10.

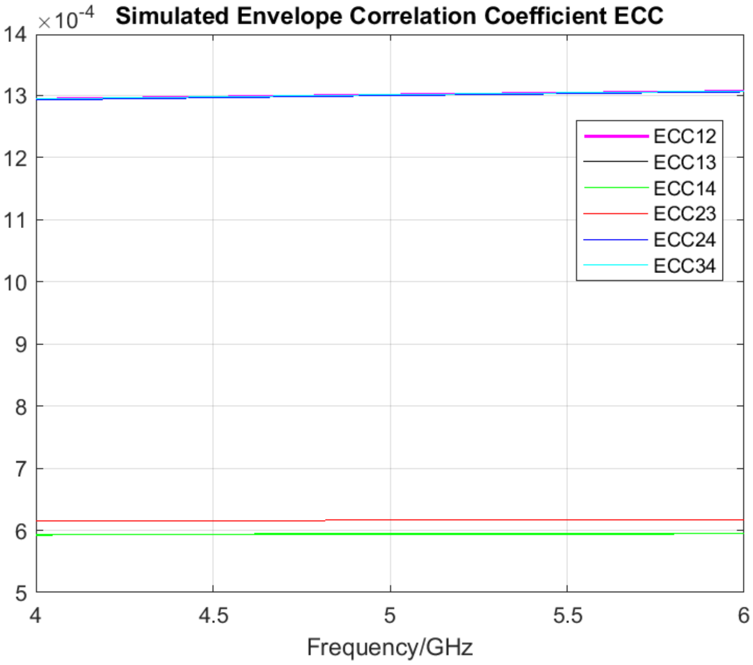

(a) Simulated ECC

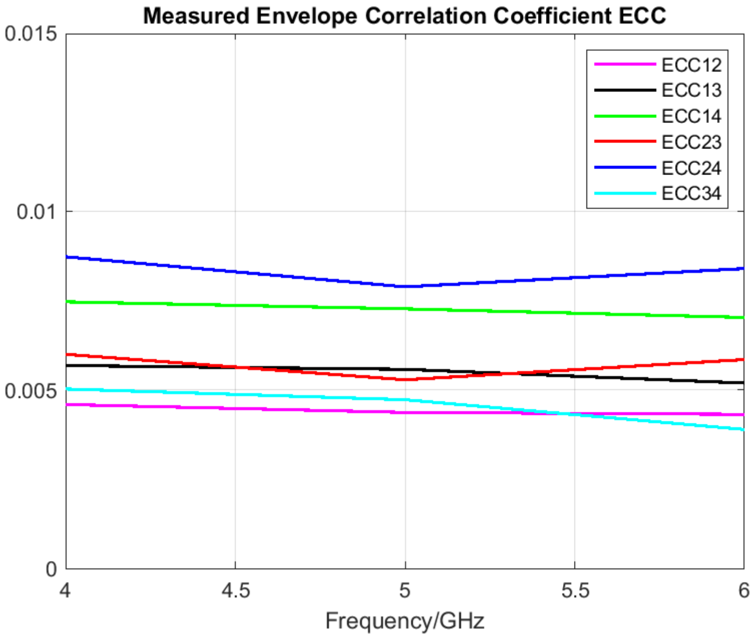

(b) Measured ECC

Figure 5.26: ECC for the MIMO system

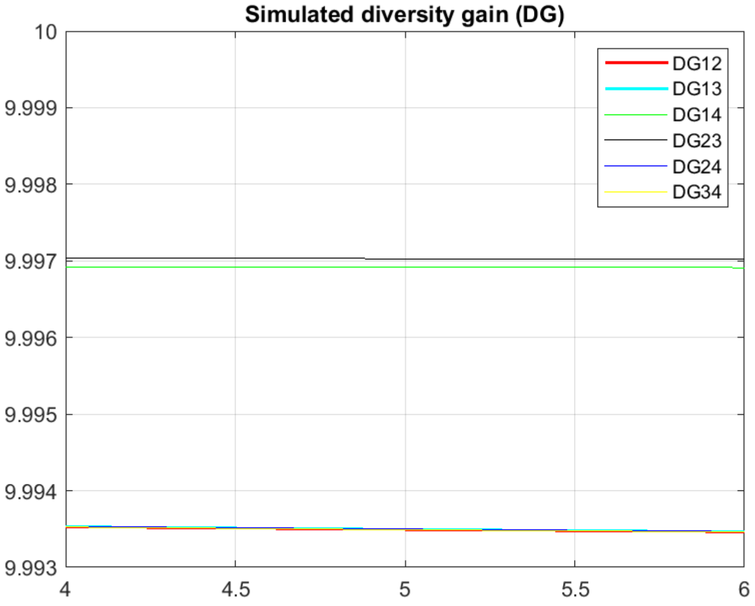

(a) Simulated DG

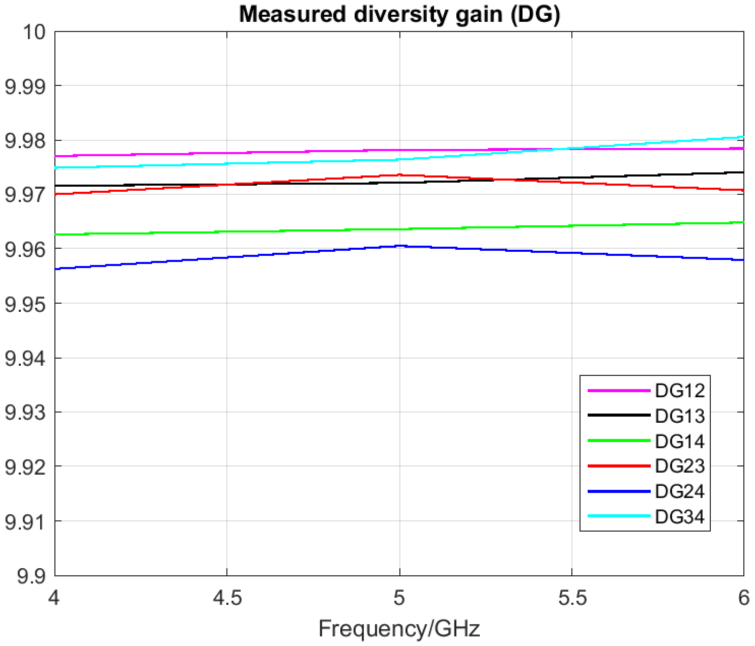

(b) Measured DG

Figure 5.27: DG of the MIMO system

5.4 Conclusions

A single RDRA antenna with CP and high gain at the C-band spectrum was designed. It presumes an Impedance bandwidth of 5.45% with an axial ratio $<$ 3dB of 26.05 % overlapping the resonant frequency. Moreover, the design presents a unidirectional radiation pattern with a maximum gain of 7.03 dBi. Consequently, a four antenna MIMO system was investigated based on the first reported design. The system considered a 30 ° angled slot located at the GP of the four antennas as a mutual coupling reduction technique. An average maximum reduction of 27 dB was present due to the angled slot in combination with the antenna positioning. Moreover, each antenna left position shift suggested four lateral radiation beams, split by regions corresponding to the antenna users. The antenna gain of the single element is preserved in the MIMO system. In terms of the radiation pattern behaviour, four main beams located at ϕ = -33 °, -124 °, 55 ° and 146 ° were identified through the measurements with axial ratio <3 dB. MIMO ECC, DG metrics of the system were found in range. The measured parameters results were in good agreement with the simulated CST results. These antennas are well-suited for 5G user equipment integrated into routers within a MIMO architecture. This configuration enables reliable and high-speed communication, making it suitable for home wireless communication systems and in line with its operation frequency band.

Chapter 6

Rectangular DRA mmWave MIMO

In this chapter, a RDRA design at the mmWave spectrum is investigated due to the favourable performance demonstrated in Chapter 5. An initial linearly polarized antenna was subjected to both simulation and measurement for comprehensive characterization. Its corresponding MIMO system was assessed in terms of mutual coupling reduction, ECC and DG. Slot etching techniques are employed to reduce mutual coupling, which is assessed by measuring an inter-port reflection coefficient reduction $<$ -20 dB.

6.1 The mmWave frequency range

Rectangular DRAs will be investigated at mmWave spectrum. The mmWave spectrum is defined in [116] as a range of waves propagating from 30 to 300 GHz frequencies. Its wavelength, λ_0, corresponds to the millimetre equivalent size ranging from 10 mm to 1 mm. Millimetre wave systems main characteristics can be highlighted as narrow beam widths generated by antennas, an influence coming from the atmosphere at the propagation moment, and wide frequency bandwidths. The antennas presented in this chapter were designed to resonate at 28 GHz, with a free space wavelength of λ_0=10.7 mm. This frequency was selected due to its nature as a transmission band, in addition to an oxygen attenuation of $<0.1 \frac{dB}{km}$ as well as a water vapour attenuation of $0.1 \frac{dB}{km}$. Moreover, the size of the antenna is reduced but it is feasible for physical fabrication and manipulation. Additionally, the manufacturing challenges were considered for making the design component selection.

6.1.1 RDRA antenna feeding considerations at mmWave

This chapter presents RDRAs at mmWave with linear polarisation. As a starting point, design considerations will be presented followed by its corresponding experimental results.

The RDRA matching is constituted by a combination of the feeding mechanism impedance and the ceramic resonator characteristics on top of the prototype. The slot aperture width w_s, length l_s as well as position s size will control the amount of admittance passing through the circuit which in consequence will determine the percentage of antenna impedance bandwidth and the resonant frequency. The DR position for this case was placed symmetrically in the middle of the slot aperture.

Referring to the overall RDRA feeding design structure in Fig.2.10b, from the bottom layer, the transmission line is highlighted in gold. The top face in dashed black shows the area for locating the slot aperture etched on the same substrate. The substrate copper layers, illustrated in gold colour in Fig. 2.10b consist of a double-sided 35μm .

The resonance modes and propagation of the RDRAs operate as previously explained in Chapter 2, section . The ceramic resonator size initial considerations were based on [25] and considering h with a similar value to w and $2{\cdot}l$.

Based on Fig. 6.1, on the bottom, the transmission line will propagate electromagnetic waves to reach the aperture slot confinement. Once the slot aperture area is reached, the Electric field will be reduced significantly due to the boundary condition of the PEC in the GP. By defining the ceramic resonator's permittivity on $\epsilon_r = 9.9$, the Magnetic field will be confined and as a consequence will follow the pattern of the walls of the ceramic material to generate short magnetic dipole finalising in the antenna radiation.

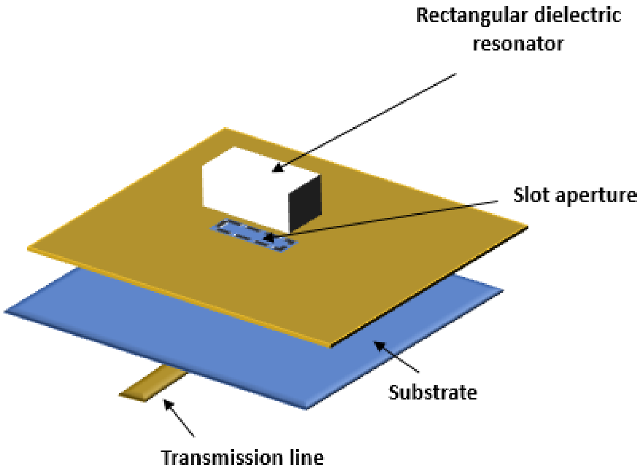

Figure 6.1: RDRA general structure

6.2 Single RDRA mmWave

The initial antenna design considerations consist of a resonant frequency of 28 GHz, with a wavelength $\lambda_0 = 10$ mm. The antenna design substrate material refers to a Rogers RT5880 with a $\epsilon_r = 2.2$, with a size of $1.62\lambda_0 \times 1.62\lambda_0$ and a thickness of 0.508 mm. The substrate copper layers have a thickness of 35 μm. The radiating slot is located at the GP aligned with the transmission line and placed at the centre of the RDRA radiating component with dimensions $0.048\lambda_0$ width, $0.191\lambda_0$ length as illustrated in Fig. 6.2.

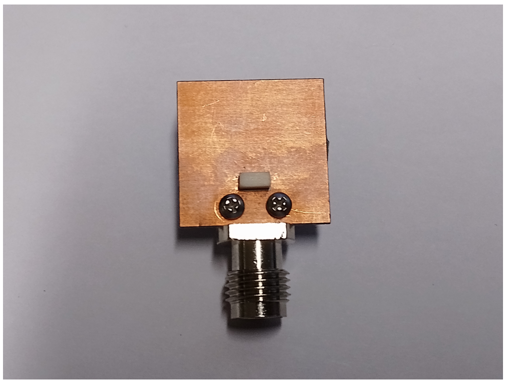

Figure 6.2: RDRA assembled antenna

The RDRA material is Alumina $\epsilon_r = 9.9$ and its dimensions are $0.322\lambda_0 \times 0.152\ \lambda_0 \times 0.155\lambda_0$. Fig. 6.2 illustrates the antenna fabricated design assembled.

6.2.1 Fabrication considerations

The antenna is fabricated of multiple parts. The first one, the PCB structure, obeying the IPC2221 standard. The second one, the Alumina ceramic resonator whose fabrication tolerances are illustrated in Table 6.1. Moreover, Fig. 6.5 illustrates the SMA board edge connector position.

Table 6.1: Ceramic resonator tolerances at mmWave

Variable name	dimension (Δmm)
width (a)	0.04
length (c)	0.12
thickness (b)	0.05
permittivity	1

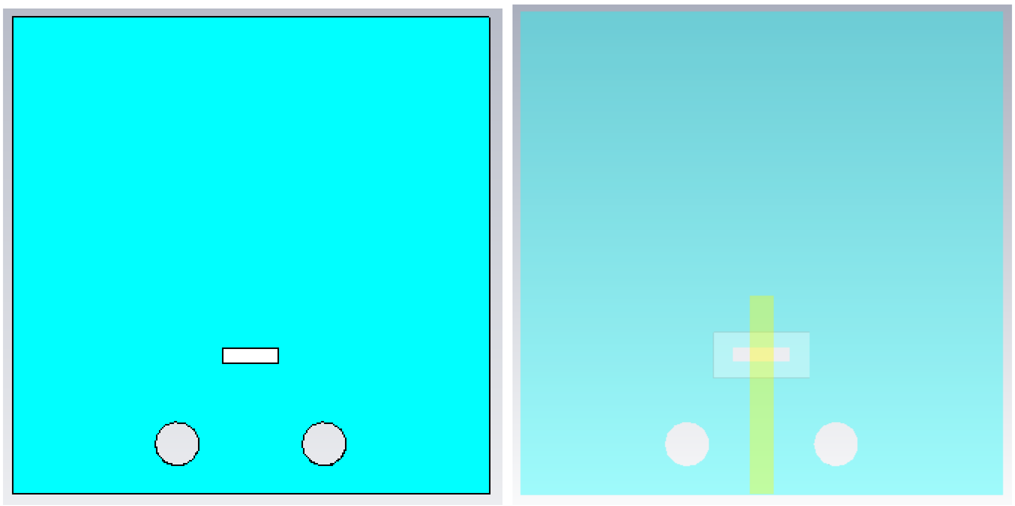

(a) Antenna design without the DR (b) Antenna design with the DRA

Figure 6.3: DRA mmWave single element design

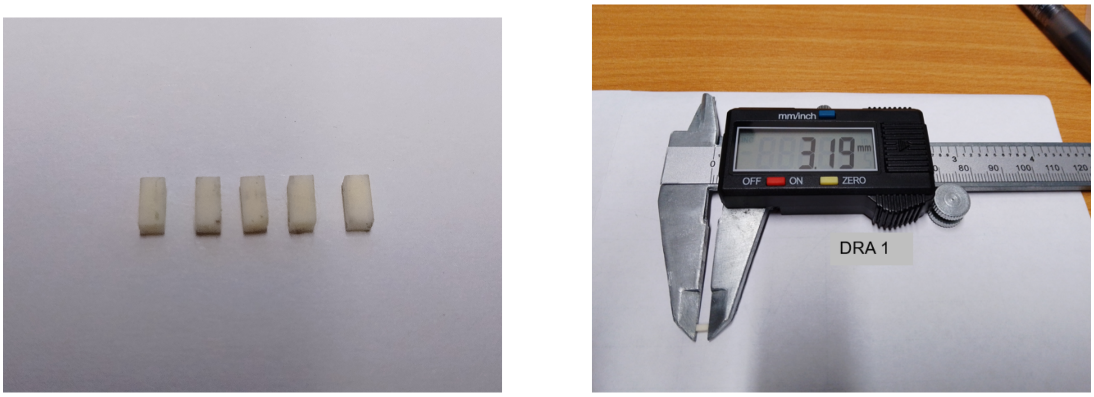

(a) Rectangular ceramic pieces (b) Ceramic piece measured size

Figure 6.4: Ceramic rectangular resonator at mmWave

6.2.2 RDRA assembling methodologies

As part of the assembling methodology. The SMA connectors were placed in the substrate via screwing. For the ceramic resonator assembling procedure, a silkscreen was printed by the antenna supplier as illustrated in Fig. 6.5.

As an alternative cheaper surface printing technique, A4 Sheets Heat Toner Transfer Paper was laser printed at approximately 200 °C with the rectangular 2D DR position shapes and then transferred by ironing the substrate shown in Fig. 6.5b

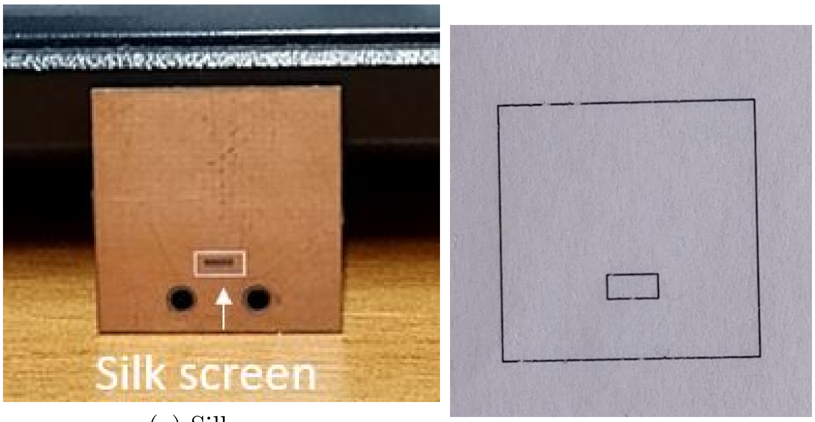

(a) Silkscreen

(b) Laser printing

Figure 6.5: DRA connector assembling

Two different materials were utilised for adhering the resonator to the substrate. The first one refers to sellotape due to its transparency with EM waves on top of the resonator and the second one to the use of double-sided copper tape with a thickness of 0.04 mm in between the ground plane and the DR, considering a slot aperture gap on the inner section of the ceramic material.

6.3 Single mmWave RDRA

6.3.1 S-parameters

S-parameters were initially measured for the single RDRA element with the PNA-X Network Analyzer N5245B. The DR alignment on the substrate is crucial for obtaining accurate results for this case. The measured impedance bandwidth of the antenna resulted in a 6 % against a 4.025 % of the simulated design. The resonant frequency suffered a shift from 28.07 GHz of the simulated design to 27.5 GHz which is attributed to assembling and fabrication uncertainties. Fig.6.6 shows the comparison of both cases. Simulations and measurements show a good agreement.

6.3.2 Antenna radiation pattern

The Standard Gain Horn (SGH) antenna ANT-WGP-26-40 was placed as a transmitter in LOS with the positioning best practice consideration of no more than $\frac{\lambda_0}{3}$ apart from the centre of each antenna. The AUT was connected to the PNA-X Network Analyzer N5245B and at the same time connected to the NSI2000 system. The radiation pattern scanning was considered in a range of ϕ = -90 ° to ϕ = 90 °.

Fig. 6.7a shows the absolute value for the radiation pattern at the resonant frequency, stated

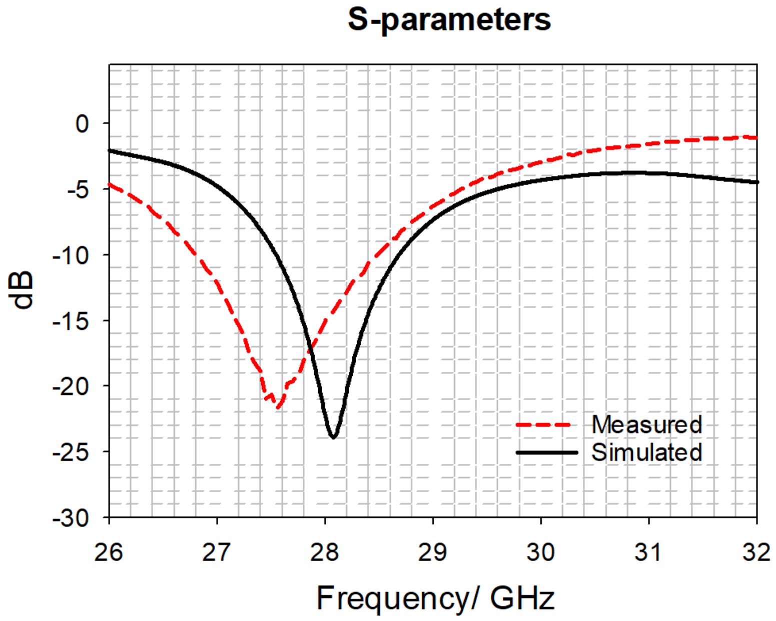

Figure 6.6: S-parameters single element

below as 28 GHz. The main beam radiation is expected to be oriented unidirectional to $\theta =$ 0 ° and $\phi = 0$ °. Simulations and measurements are in good agreement. For the case of Fig. 6.7b, the main beam radiation is expected to be oriented unidirectional to $\theta = 0$ ° and $\phi =$ 90 °. A tilting of 13° can be seen as part of the simulation. A slight tilting on the measured pattern is attributed to the antenna's alignment. In the case of the $\phi =$ -90 ° lump can be attributed as a systematic error which can be observed in Chapter 4 measurements.

6.3.3 Antenna gain

By observing the radiation pattern beam maxima, the antenna gain of the RDRA can be determined. The maximum realized gain exposed in simulations at the resonant frequency is 7.07 dBi. As illustrated in Fig. 6.8, measurements show a difference not bigger than 2 dBi on the frequency range and agree with simulations. The difference is attributed to the adaptor in addition to cable losses.

6.4 Four RDRA mmWave MIMO

Moving on to the MIMO system structure, the design consists of a substrate material Rogers RT5880 with a $\epsilon_r = 2.2$, its size is $1.62\lambda_0 \times 1.62\lambda_0$ and the thickness of the substrate is 0.508 mm. The conductive sides of the substrate material are made of copper with a thickness of 35μm . The antenna system considered four RDRA elements positioned in the opposite direction one from the other at 0 °, 90 °, 180 ° and 270 ° on the 2D plane. The distance

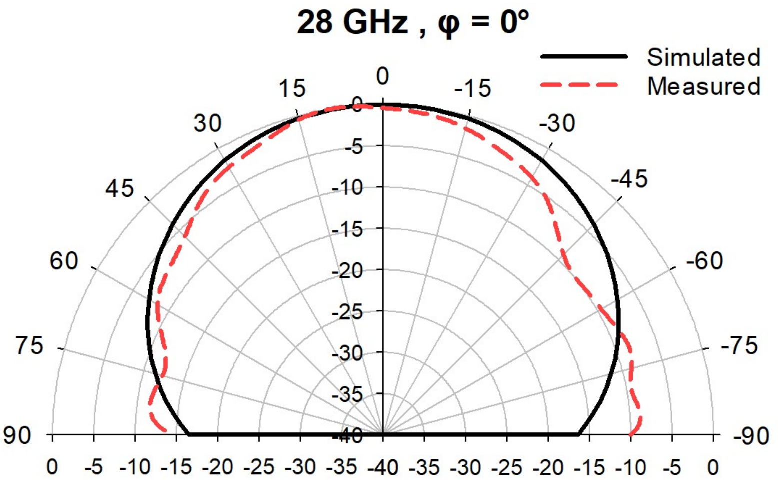

(a) ϕ= 0 °

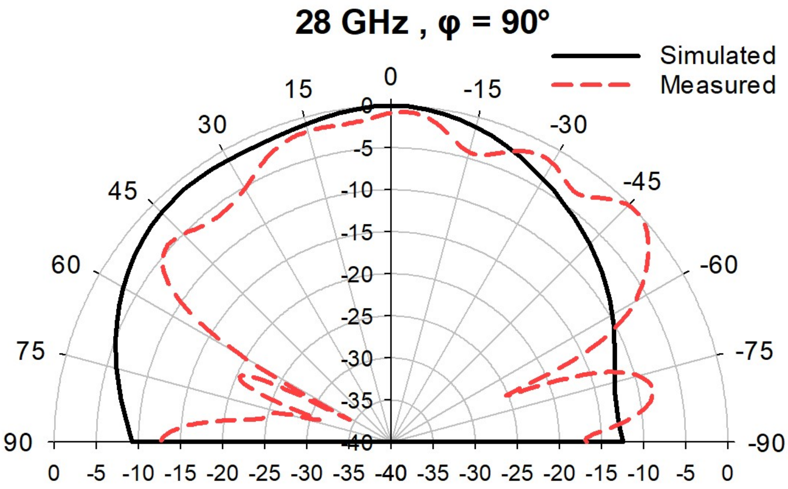

(b) ϕ= 90 °

Figure 6.7: Single element radiation pattern

between RDRA's from centre to centre is approximately $0.6\lambda_0$ which obeys the minimum distancing between elements of $\frac{\lambda_0}{2}$.

The antenna assembly procedure was the same utilised for one element. Fig. 6.9 shows the four element PCB and the assembled corresponding MIMO antenna at Fig. 6.9a Top view with RDRA, Fig. 6.9b Top view without RDRA, and Fig. 6.9c bottom view. In Fig. 6.10, the fabricated antenna view is illustrated with the corresponding port labelling which will be utilised throughout this chapter.

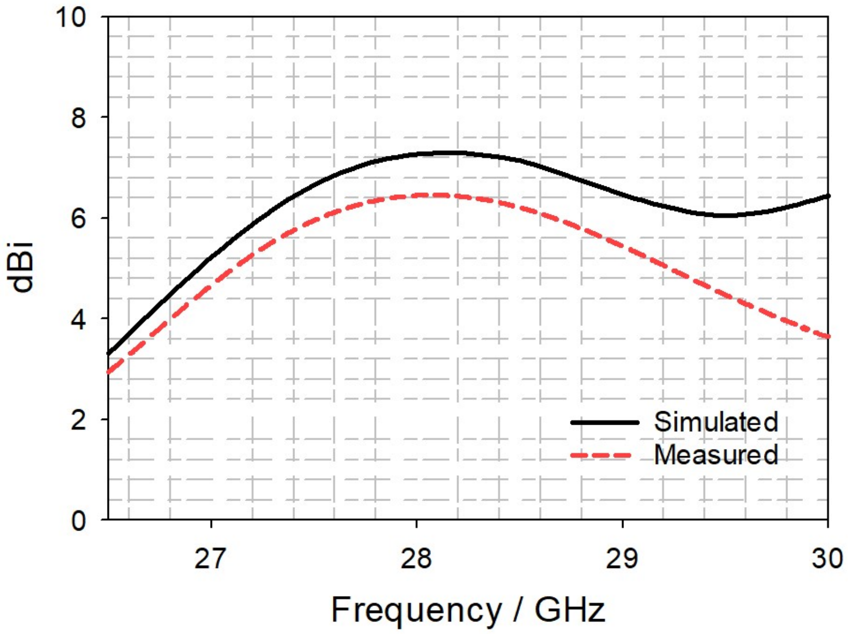

Figure 6.8: Realized gain on the antenna frequency band

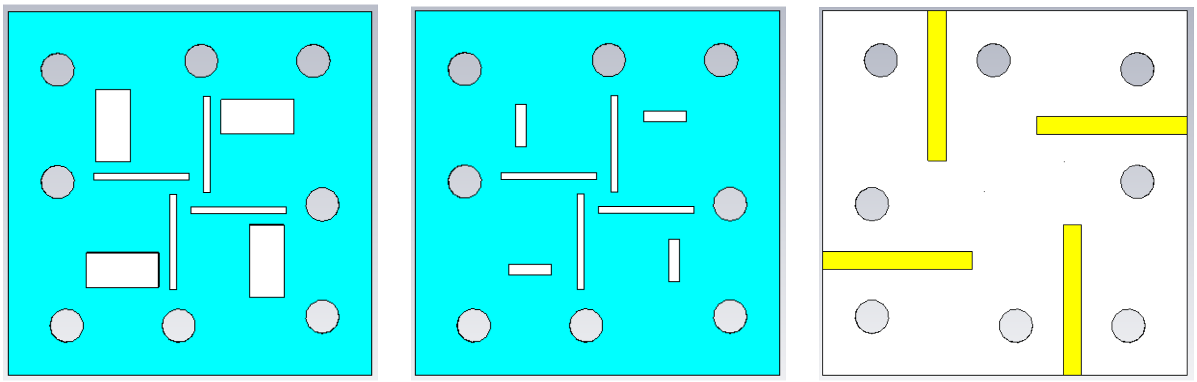

(a) Four antenna design with the DR

(b) Four antenna design without the DRA

(c) Back view four antenna design

Figure 6.9: Antenna MIMO designs with DRAs

6.4.1 Four MIMO RDRA design simulations

There are two main strategies employed through this work for reducing the mutual coupling between the elements of the MIMO.

The first one refers to the RDRA positioning in the GP, in which the four elements are located in a symmetrical orthogonal location at 0 °, 90 °, 180 ° and 270 ° in the x-y axis direction. Each one of the RDRA's is shifted 0.065 λ_0 from the middle of the board to the left-hand side direction. The radiation pattern is influenced by the positioning of the antenna which in this case will propagate in the direction of the shifting. The second strategy

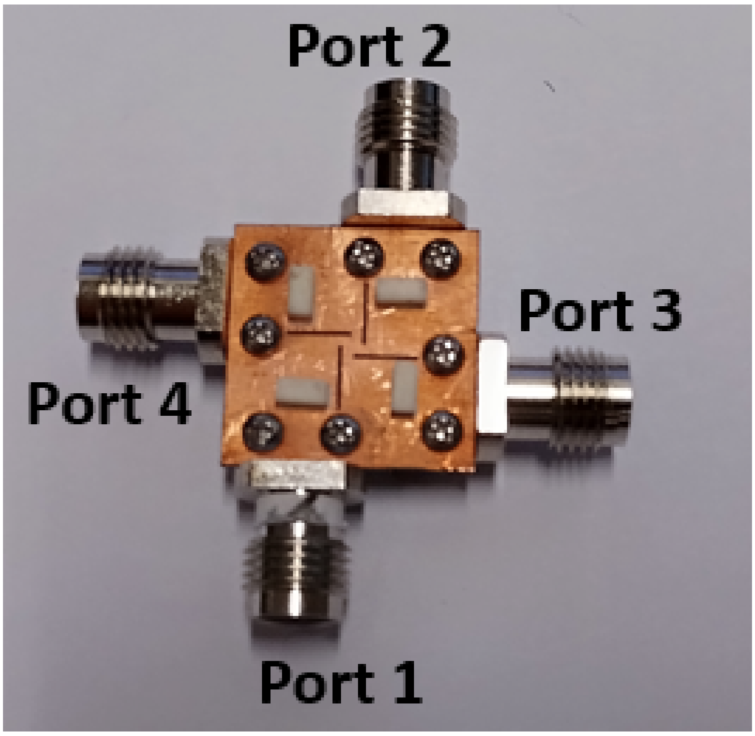

Figure 6.10: MIMO RDRA structure assembled

refers to the use of slots positioned at GP of the antenna. They are placed in parallel to the radiating RDRA with dimensions of slot length 0.425 λ_0 and slot width $0.03\lambda_0$ as illustrated in Fig. 6.11.

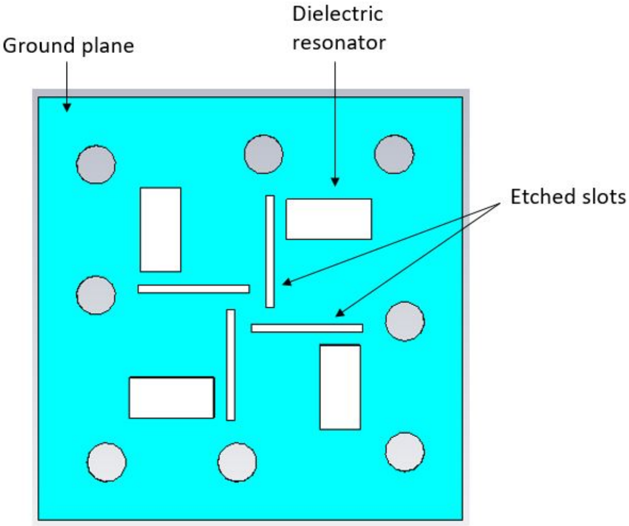

Figure 6.11: Ceramic rectangular resonator

Next, attention is paid to the slot etching effect of the antenna performance. The slots influence directly the antenna matching which will reflect on the resonant frequency, surface current, and consequently its EM fields. Table 6.2 shows the most notable differences with and without slots in the design.

Table 6.2: Slots etched comparison

	Without slots	**With slots**
Maximum surface current	393 $\frac{A}{m}$	423 $\frac{A}{m}$
Realized gain	7.33 dBi	7.06 dBi
Resonant frequency	27.6 GHz	27.8 GHz
Impedance bandwidth	4.28 %	5.18%

The addition of the slots in the GP provoked an increment in the surface current leading to a change in radiation efficiency reflected on the overall antenna realized gain. Moreover, there is an increment in the impedance bandwidth of the antenna, where the slot effect is reflected in a modification of the reactance. Fig.6.12 illustrates the reflection coefficient reduction within -7 to -14 dB within the frequency range. The geographic position of these antennas is parallel to each other which contributes to the RDRA's isolation.

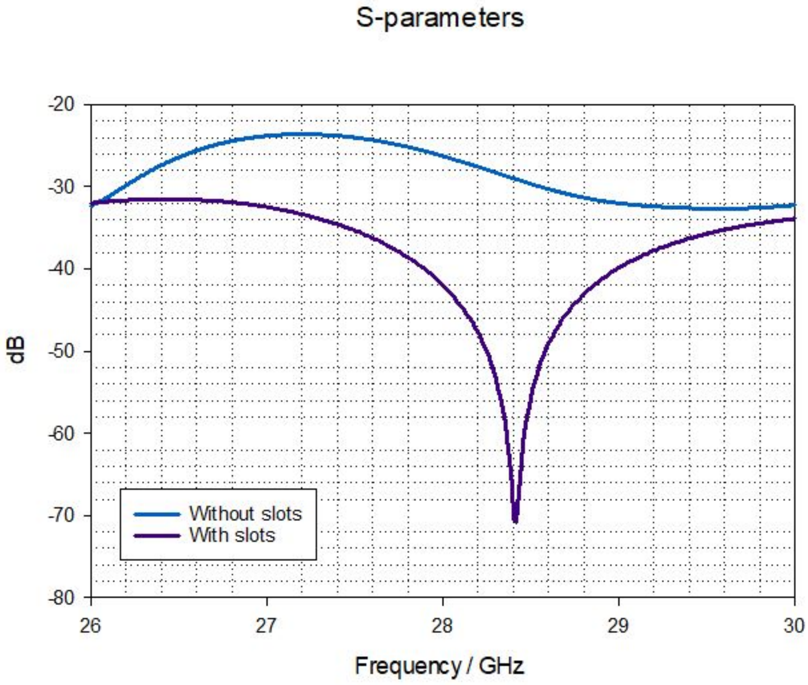

Figure 6.12: $S_{12}, S_{21}, S_{34}, S_{43}$ with and without slots addition

Complementary, Fig. 6.13 illustrates the reflection coefficient between perpendicular antennas in the proposed system. In this case, the slots provoked an increment in the S-parameters which relies on relatively small power reflected values below the -20 dB threshold.

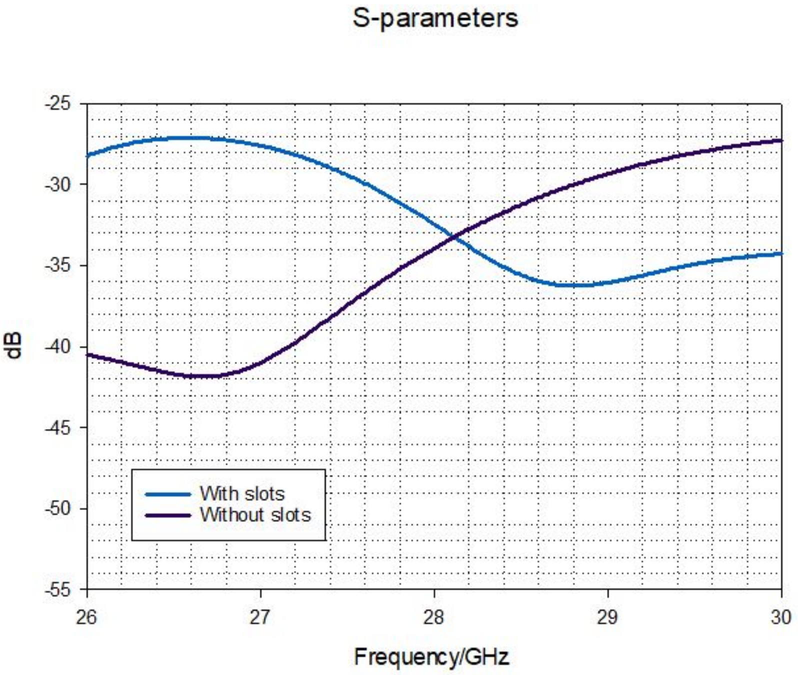

Figure 6.13: $S_{13}, S_{31}, S_{14}, S_{41}, S_{24}, S_{42}, S_{23}, S_{32}$ with and without slots addition

The addition of the slots in the GP has a potential impact on the antenna's mutual coupling reduction, however, it doesn't represent a homogeneous reduction of the system, it will depend on the direction and location of them. Its size will have a specific reflection coefficient reduction effect according to the frequency affected and the proximity of them to the radiators can produce a direct disturbance in the impedance matching and the resonant frequency.

6.4.2 MIMO S-parameters

Experimentally, the first stage consisted of validating the correct assembling for the MIMO structure; reflection coefficients were measured with the PNA-X Network Analyzer N5245B at the UKRI (National Millimetre Wave Facility). At this stage, the dielectric resonators were placed meticulously on top of the GP with the aid of the previously mentioned silkscreens. Any additional stress on the substrate or even glue residues from gluing tapes can have a direct impact on the resonant frequency of the antenna, modifying its performance due to the propagated high frequency.

The calibration procedure was applied to the HP 8720B Network Analyzer in ports 1 and 2. E-cal module was connected to the ports of interest at the frequency range 26 to 30 GHz. Each pair of ports, labelled as shown in Fig. 6.10 were connected to the VNA after calibration to obtain their corresponding scattering parameters. Ports 1 and 2 were initially connected to the VNA for measuring S_{11}, S_{12}, S_{21}, S_{22}, the rest of the ports were terminated by 50Ω loads. The same procedure was followed but for measuring S_{33}, S_{34}, S_{43}, S_{44} , leaving ports 1 and terminated at 50Ω. For the specific case of the ports located perpendicularly to each other, S_{13}, S_{31}, S_{14}, S_{41}, S_{23}, S_{32}, S_{24}, S_{42} were connected to the Analyzer ports, terminating at the same time the rest of the perpendicular ports with high frequency 50 Ω loads. The Scattering parameters of the four cases with their four corresponding ports will be presented and discussed in the following section. It is relevant to mention that an average 500 MHz shift in frequency is expected for the case of the use of double-sided copper tape. Fig. 6.14 refers to port 1 simulated and measured values. S_{11} measurements show a resonant frequency of 27.5 GHz and an impedance bandwidth of 6% as illustrated in Fig. 6.14a. By comparing its simulated results, the resonant frequency suffers a shift of 300 MHz, and an impedance bandwidth remains almost the same. The measured results difference is attributed to the alignment of the DRA on the ground plane in conjunction with the fabrication tolerances that were presented at the beginning of this Chapter. S_{12} presents a maximum difference between simulations and measurements of 5 dB within the impedance bandwidth range as illustrated in Fig. 6.14b. Consequently, S_{13} has a maximum mutual coupling reduction difference of 5 dB when comparing measured with simulated results as shown in Fig. 6.14c. Finally, after measuring S_{14}, it can be noted that there is a maximum difference of 8 dB compared with simulated data illustrated in Fig. 7.21d.

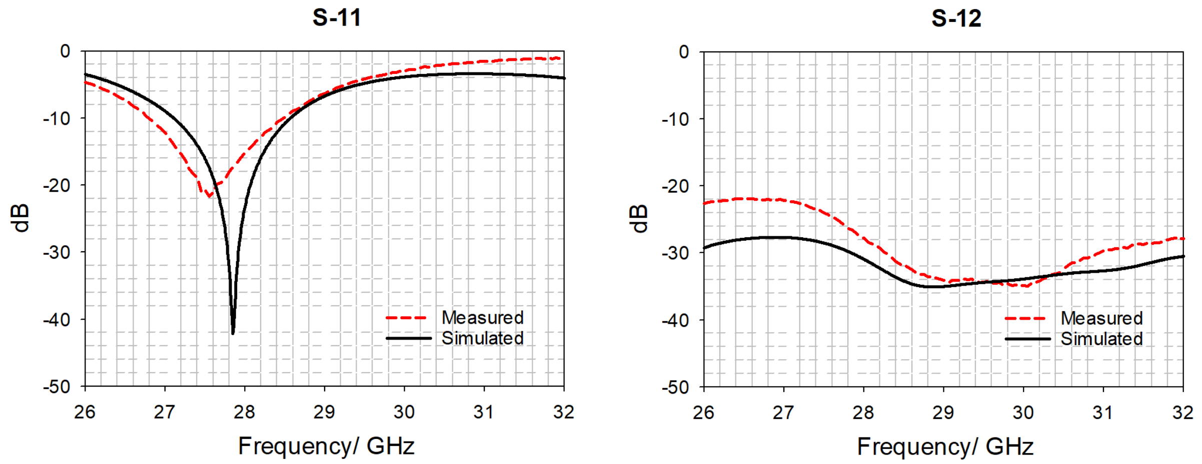

(a) S11 (b) S12

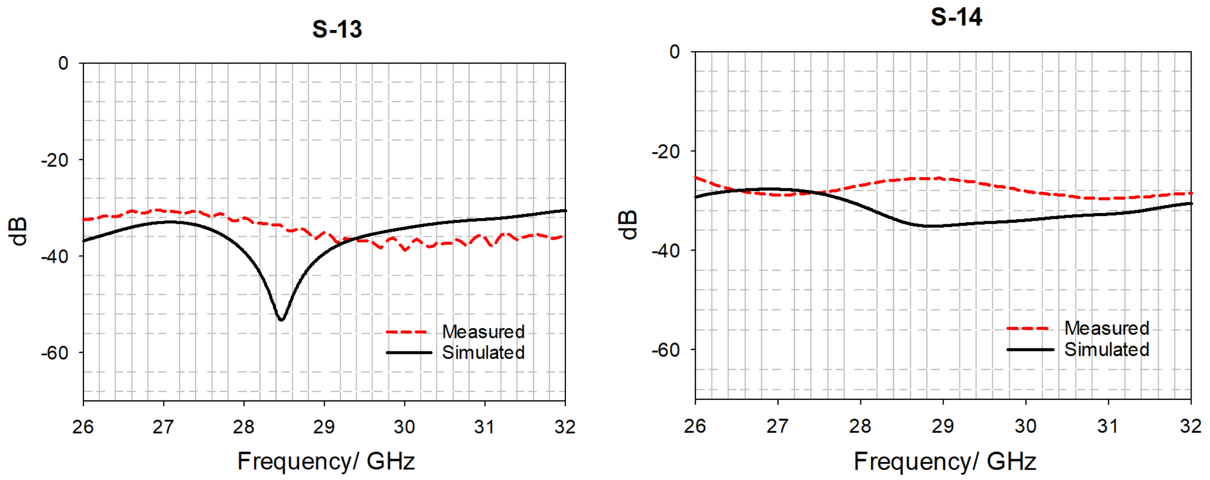

(c) S13 (d) S14

Figure 6.14: Scattering parameters when port 1 is fed.

Fig. 6.15 presents simulated and measured scattering parameters for port 2 of the antenna structure. It can be observed from Fig. 6.15a that S_{21} measured reflection coefficients are not bigger than 6.5 dB compared with simulations, within the impedance bandwidth. For S_{23}, a maximum mutual coupling reduction of 5.3 dB can be observed and for S_{24} a maximum 6 dB difference can be claimed. S_{22} illustrated in Fig. 6.15b illustrates an impedance bandwidth of 5% compared with a 5.28 % of the simulated results.

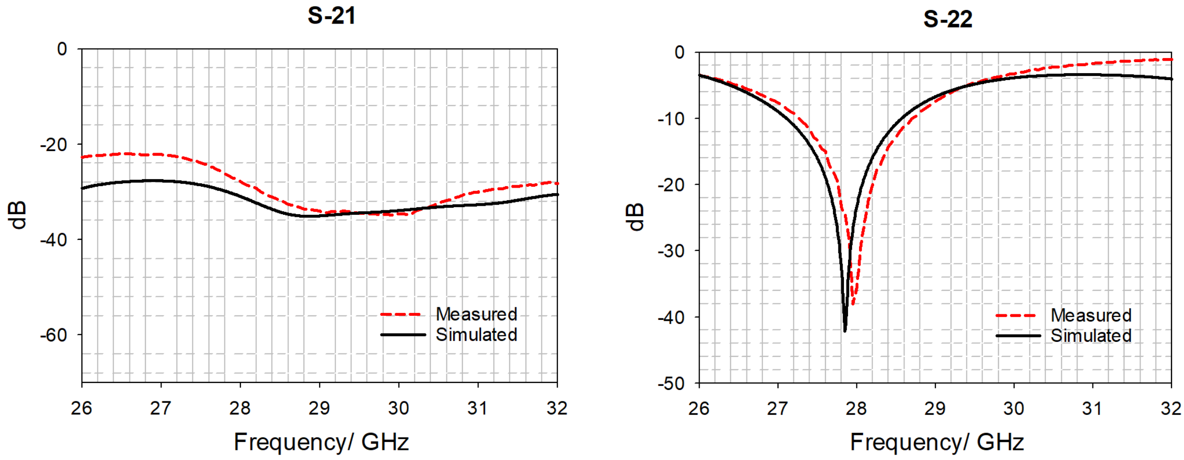

(a) S21 (b) S22

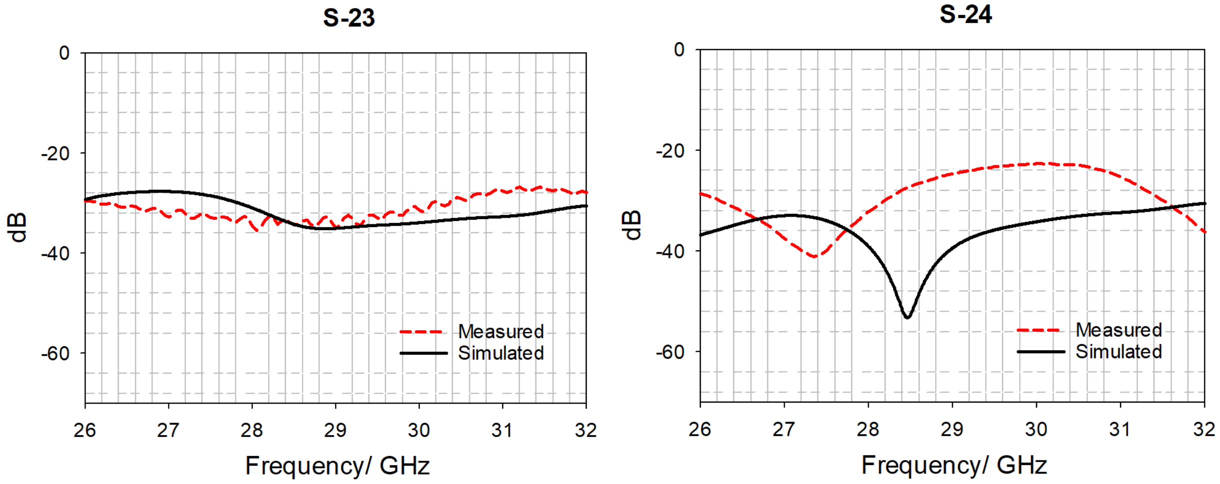

(c) S23 (d) S24

Figure 6.15: Scattering parameters when port 2 is fed.

Fig. 6.16 presents simulated and measured scattering parameters for port 3 of the antenna structure. It can be observed from Fig. 6.16a that S_{31} measurement results compared with the simulated ones are not bigger than 2.08 dB within the impedance bandwidth. For S_{32}, a maximum mutual coupling reduction of 3.76 dB can be observed and for S_{34} a maximum 4.8 dB difference can be shown in Figs. 6.16b, 7.23d. Finally , for S_{33}, Fig. 6.16c illustrates the measured impedance bandwidth is 4.46 % compared with a simulated 5.28 %.

Fig. 6.17 presents simulated and measured scattering parameters for port 4 of the antenna structure. It can be observed from Fig. 6.17a that S_{41} measurements are not bigger than 1.26 dB compared with simulations, within the impedance bandwidth. For S_{42}, a maximum mutual coupling reduction of 3.76 dB can be observed, and for S_{43} a maximum 4.28 dB difference can be shown in Figs. 6.17b, 6.17c. Finally , for S_{44}, Fig. 7.24d illustrates the measured impedance bandwidth is 4.61 % compared with a simulated 5.28 %.

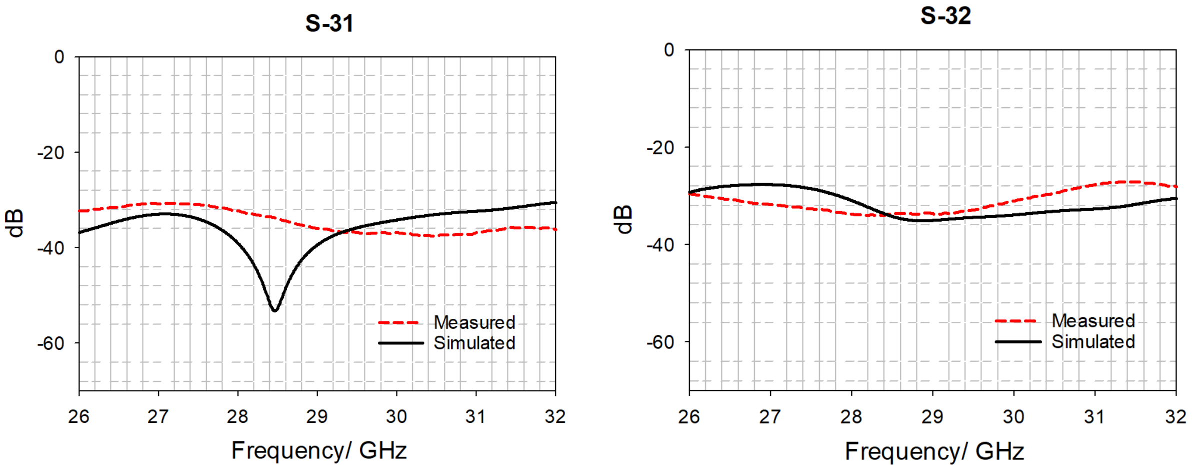

(a) S31 (b) S32

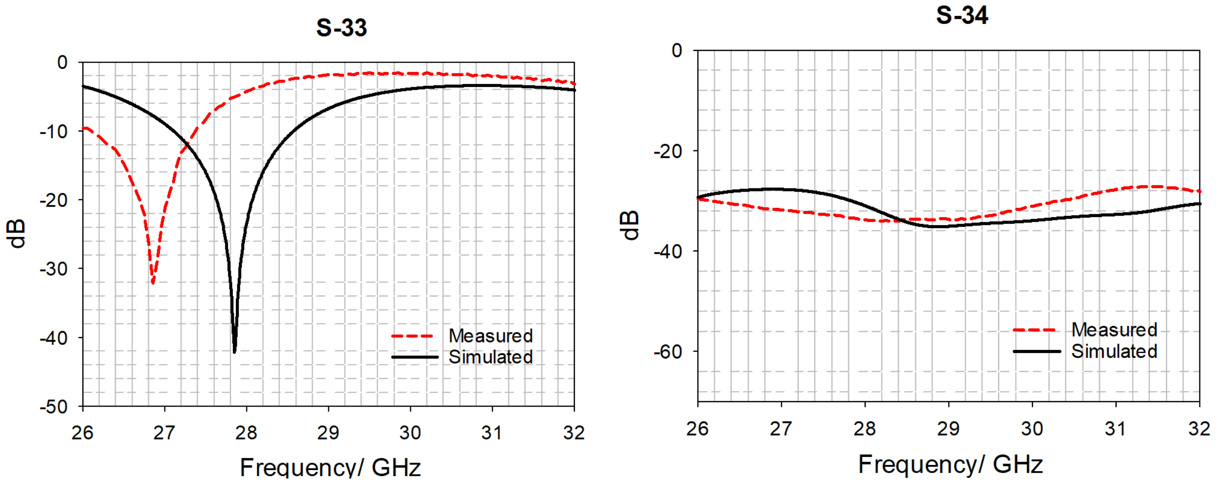

(c) S33 (d) S34

Figure 6.16: Scattering parameters when port 3 is fed.

Overall, the three inter port differences, for the 4 port cases previously mentioned, can be attributed to a couple of reasons. The first one is regarding the PCB fabrication tolerances, and the second one refers to the PCB manipulation when proceeding with measurements. Unwanted bending of the substrate due to cable weight, millimetre scratches in the ground plane, and conditions of the copper plane highly influence the before mentioned differences. Additionally, it is important to consider individually the connector's losses which are reported in [117].

6.4.3 MIMO Antenna radiation pattern

A similar methodology as the one presented in Chapter 3, section 3.5 at mmWave was followed through the present chapter. The SGH antenna ANT-WGP-26-40 was placed as a transmitter in LOS with the positioning of no more than $\frac{\lambda_0}{3}$ with the AUT and as a receiver.

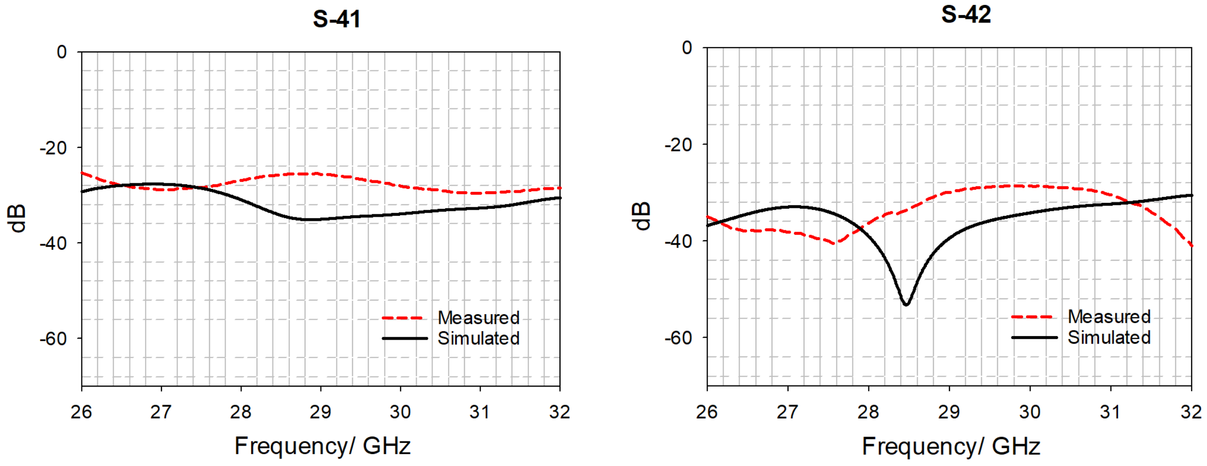

(a) S41 (b) S42

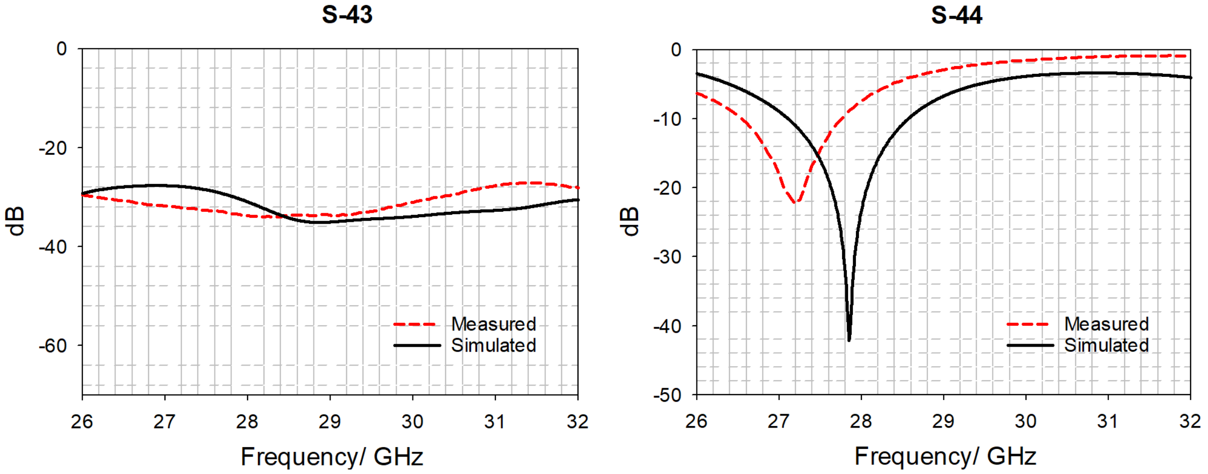

(c) S43 (d) S44

Figure 6.17: Scattering parameters when port 4 is fed.

The AUT was connected to the PNA-X Network Analyzer N5245B connected to the NSI-MI system Technologies. Moreover, the distance from SGH to AUT is approximately $53\lambda_0$. The radiation pattern full system scan for this case consisted of a four simultaneous port connection of the MIMO as illustrated in Fig. 6.18.

The system at the Elevation angle was scanned in the range of ϕ = -90 to ϕ = 90 to determine the maximum antenna radiation as well as the maxima of the realized gain. Consequently, the Azimuth angle will be analyzed in the post-processing stage with the frontal scan.

The MIMO system was fully scanned. From one side of the splitter, Fairview Microwave FMDV1069, the VNA single port was connected, from the opposite side, the four antenna ports would be receiving an equal amount of power via a 4-to-1 splitter connection with five female-to-male adaptors 6.19b working at the mmWave frequency range illustrated in Fig.

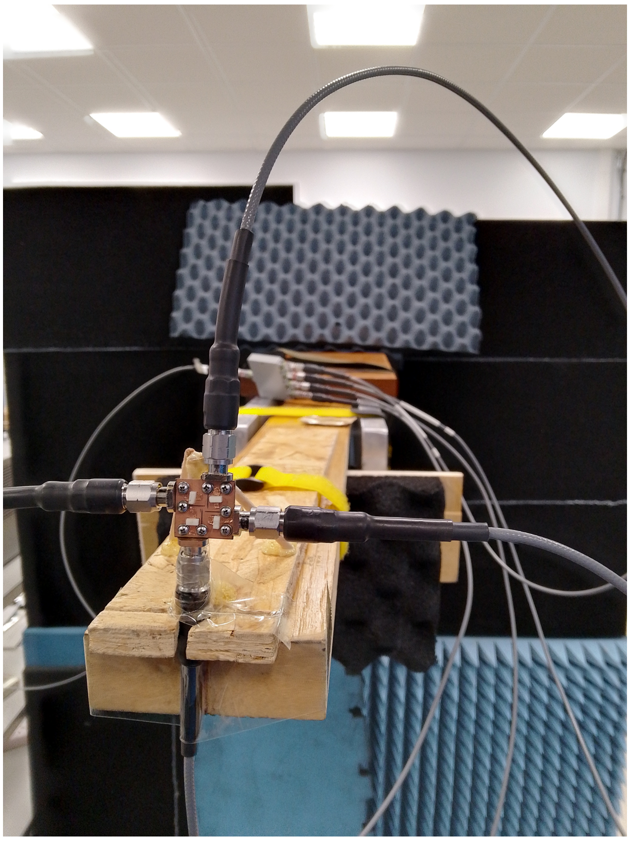

Figure 6.18: MIMO scanning set up

6.19a. Regarding the insertion losses of the splitter and adaptors, the splitter considers a maximum of 1.6 dB max according to [118]. Additionally, the utilised adaptors are no more than 0.32 dB according to [119]. This experiment tested the entire MIMO system under the conditions of a simultaneous transmission.

Following Chapter 3 C-band methodology, the maximum gain main lobe direction was first identified in the four-element radiation pattern. According to the four elements MIMO simulation, the main lobe direction refers to 32 °. Consequently, a $\theta = 32$ ° will be investigated to identify the main four element radiating lobes. Fig. 6.20 illustrates the absolute value of 4 elements at $\phi = 0$ °. The radiation pattern is in good agreement with the simulations.

Complementary, $\phi = 90$ ° cut was investigated for verifying consistency in the radiation pattern. The split at $\theta = 0$ °, $\phi = 0$ ° remains with slight variations on the termination of the lobes at exactly $\theta = 90$ ° and $\theta =$ -90 °. The variation can be attributed to a scan systematic error.

A single port of the MIMO was simulated with the rest of the three terminated at 50Ω. As indicated in Fig. 6.22 the main radiation lobe at the resonant frequency is directed to ϕ= -150 °, this is attributed to the position of the RDRA where the main's radiation lobe is directed to the largest side of the ceramic resonator. Moreover, there is a back lobe radiation

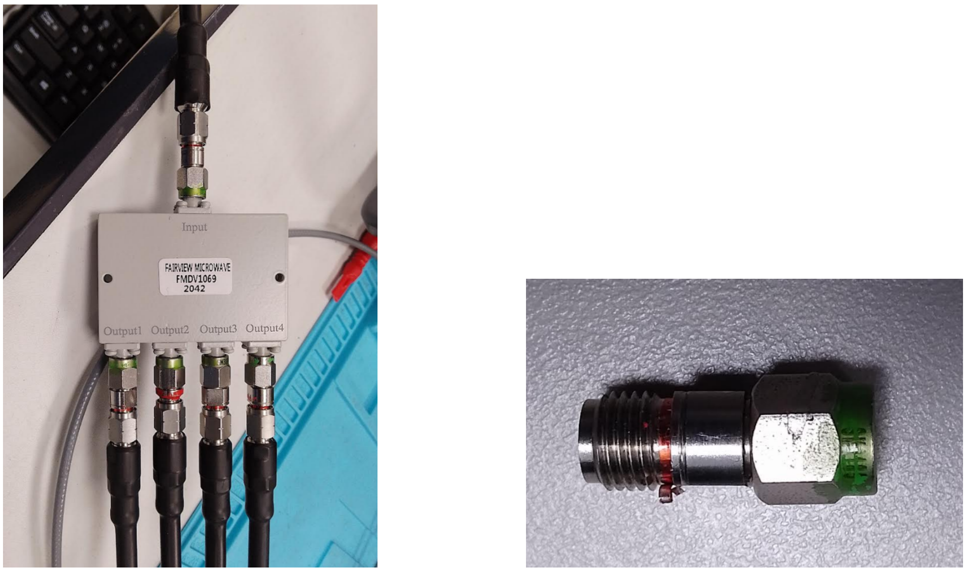

(a) 4 to 1 splitter

(b) 2.4 mm F/M adapter

Figure 6.19: Experiment components

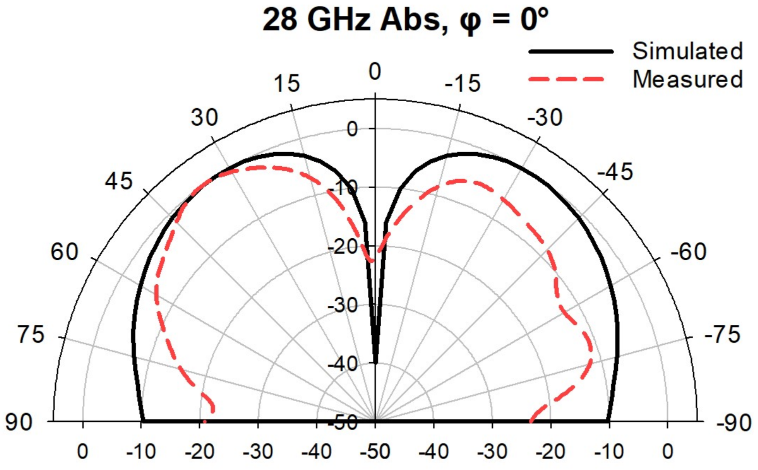

Figure 6.20: MIMO main lobes radiation

present where an interaction between adjacent antennas can be noted. For this case, it is important to mention that due to the position of the resonator, there is a contribution in terms of the surface current present bidirectionally to all of the antennas present in the MIMO system.

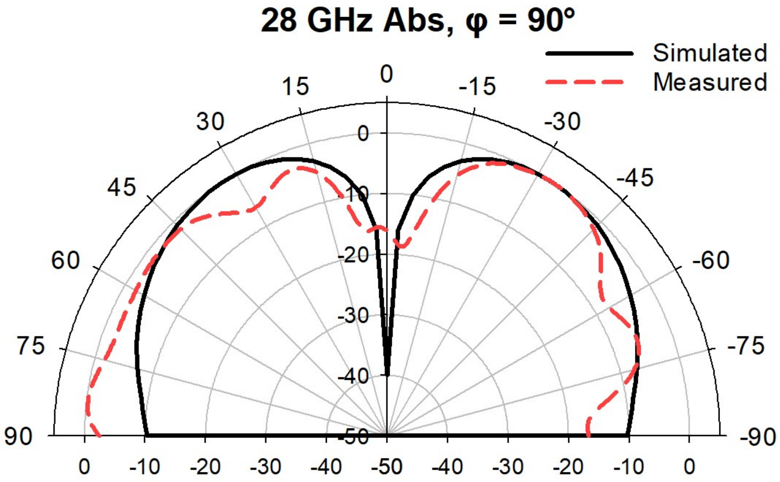

Figure 6.21: MIMO main lobes radiation

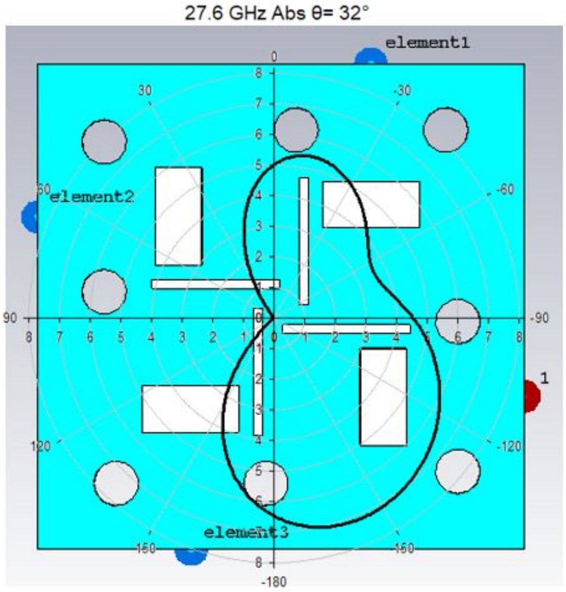

Figure 6.22: One port feeding radiation pattern

Following the iteration, two parallel ports were terminated at 50Ω for investigating the MIMO system radiation. The propagation direction of the two fed antennas is according to the single element which refers to a symmetrical design, the secondary main lobe of the second antenna is directed to ϕ= 50 °. The behaviour of two encountered of the radiation through two antennas generates a natural split between them as illustrated in Fig. 6.23 created a symmetrical null at ϕ= 150 ° and ϕ= -50 °.

In the following iteration, two perpendicular ports were terminated at 50 Ω. In this case, there is a constructive interference of the adjacent antenna radiation generating at the same time a back radiation lobe smaller than the parallel and single-fed analysis. Fig. 6.24

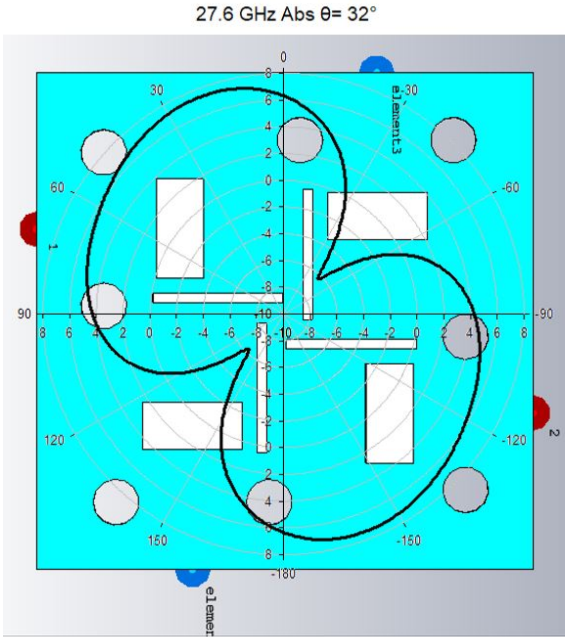

Figure 6.23: Two parallel port feeding radiation pattern

illustrates the contribution of adjacent antennas to the radiation pattern generation.

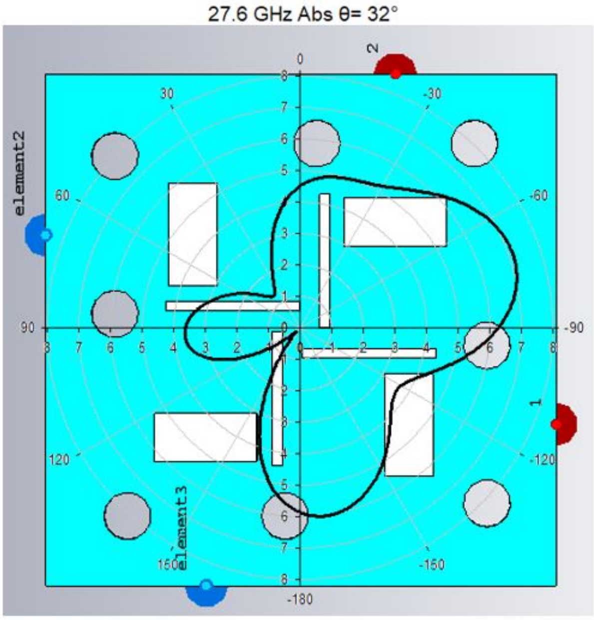

Figure 6.24: Two perpendicular port feeding radiation pattern

The four simultaneous ports were tested with an equal power input. The $\theta = 32$ ° cut is shown in Fig. 6.25. Three clear main petals can be illustrated in the Figure. The misalignment of the -40 ° is attributed to a millimetre misalignment of the DRA for the slot aperture. At this point, it is important to mention the inevitable tension produced when connecting the system to the 4-way splitter due to the weight of the connectors in addition to the length of the 2.4 mm cables. Despite the slight difference, three lobes can be observed with the beam width of the simulations.

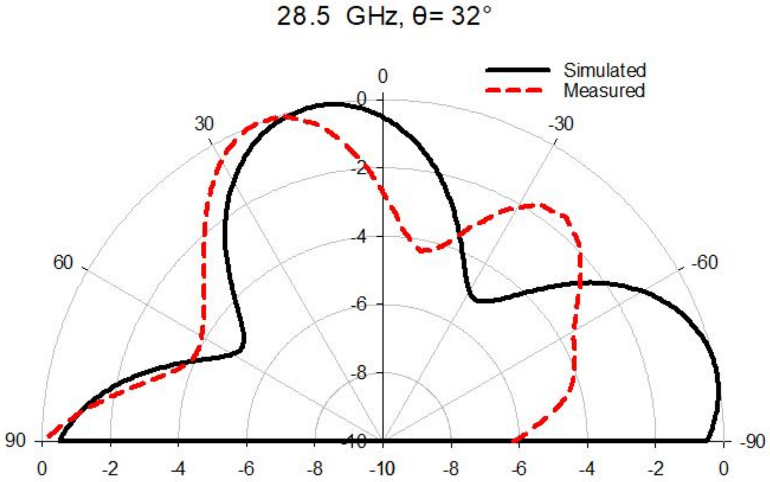

Figure 6.25: MIMO main lobes radiation

The four-port element 3D radiation pattern is illustrated in Fig. 6.26 and Fig. 6.27. Measured and simulated radiation patterns can be able to show four main beams corresponding to each antenna maximum radiation point.

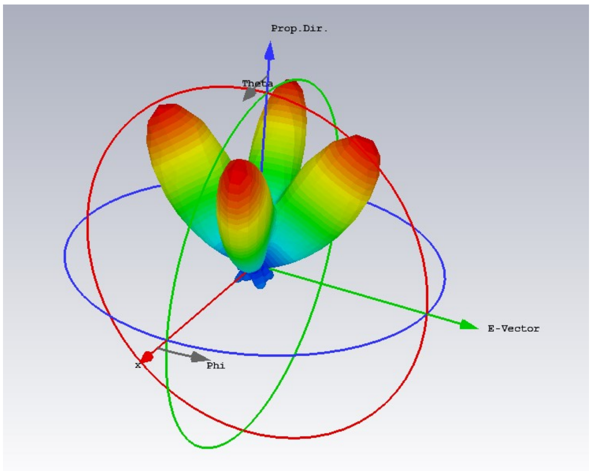

Figure 6.26: Simulated 3D radiation pattern

6.4.4 Four ports MIMO antenna gain

The realized gain of the four MIMO RDRA's at each maxima radiation lobe are illustrated in Fig. 6.28. The directions evaluated for the system case were 15°, 90°, -75° and -173°

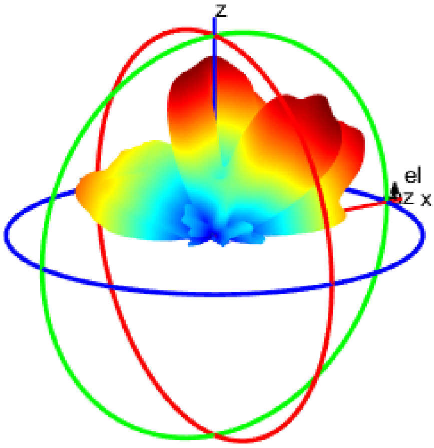

Figure 6.27: Measured 3D radiation pattern

respectively. Fig. 6.28a shows a range of homogeneous differences between 1 to a maximum of 2 dBi within the frequency range, attributed to connector losses. Simulated and measured results are in good agreement. For the second case, Fig. 6.28b shows similar behaviour to the first case. Simulated and measured results are in good agreement. Fig. 6.28c shows a maximum of 4 dBi difference at the lower frequencies within the previously mentioned impedance bandwidth. At this angle, it is important to consider the scanning procedure, despite the beam forming according to the simulations, there is a discrepancy in the results since the threshold maximum scanning angle is at 90 °. Simulated and measured results are in good agreement. Fig. 6.28d only shows the simulated results which are similar to the cases of Figs. 6.28a , 6.28b and 6.28c due to the MIMO design considerations. The entire radiation pattern can be seen in Fig. 6.27.

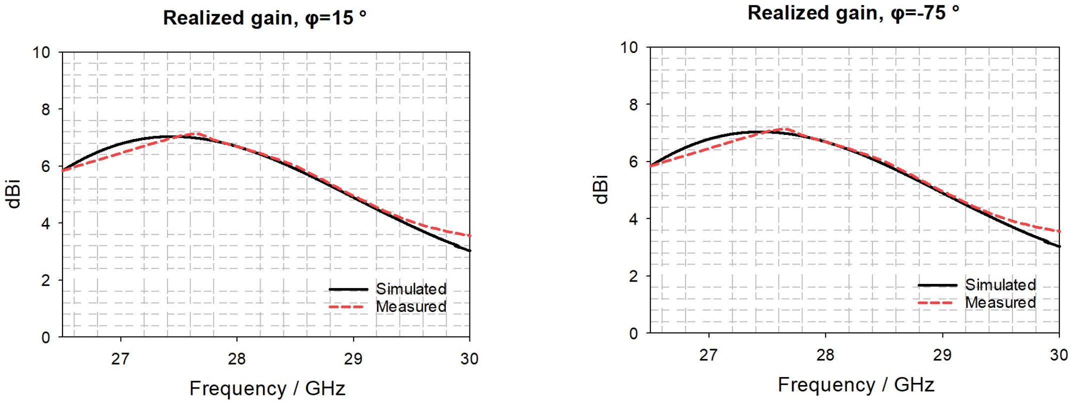

(a) Realized gain at ϕ= 15°

(b) Realized gain at ϕ= -75°

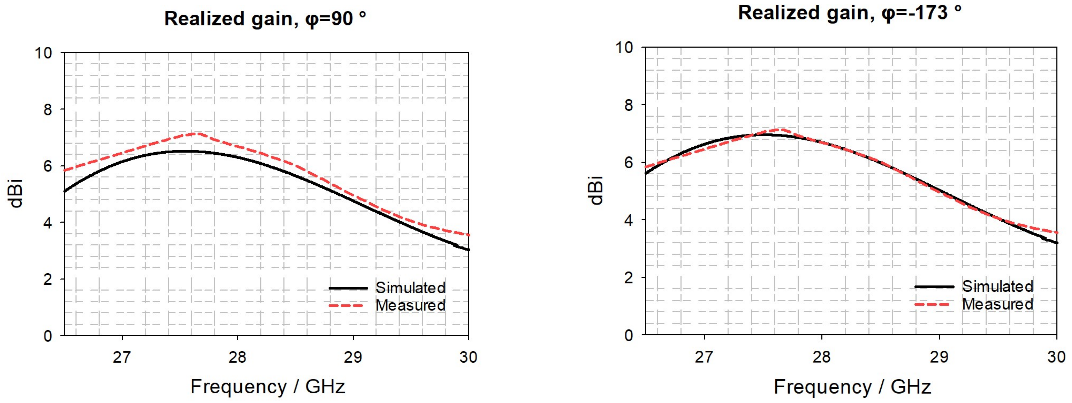

(c) Realized gain at ϕ= 90°

(d) Realized gain at ϕ= -173°

Figure 6.28: MIMO four beam realized gain

6.4.5 ECC and DG for the MIMO system

Moving on to the MIMO system performance evaluation, ECC and DG were evaluated to determine each antenna's independence in the system. Fig.6.29a illustrates the relationship of the inter ports showing repeatedly results due to the symmetry of the design, in a range of 0.045 to 0.075. In comparison, Fig.6.29b presents an increase of these results as a consequence of the interaction with a real environment with losses coming from connectors, adaptors, as well as the calibration system. For this case, a range of 0.1 to 0.35 values were obtained. Simulated and measured results fulfill the MIMO ECC and DG stated threshold which is explained in [40].

Complementary to the ECC results, diversity gain was calculated in the simulation. It can be observed in Fig. 6.30a that DG is lower than 10. In the case of the measured results, considering DG is a complementary value to the ECC, measured values illustrated in Fig. 6.30b for DG12, DG13, DG14, DG23, DG24, DG34 suffers an increment but they are still considered at not bigger than 10.

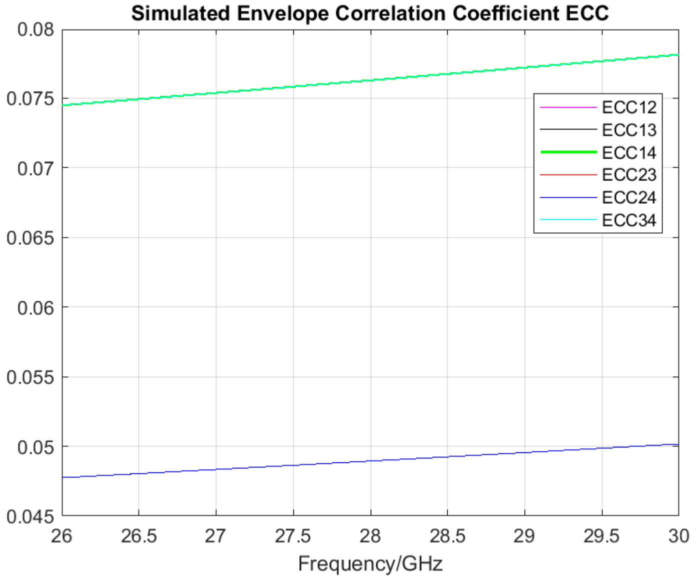

(a) Simulated ECC

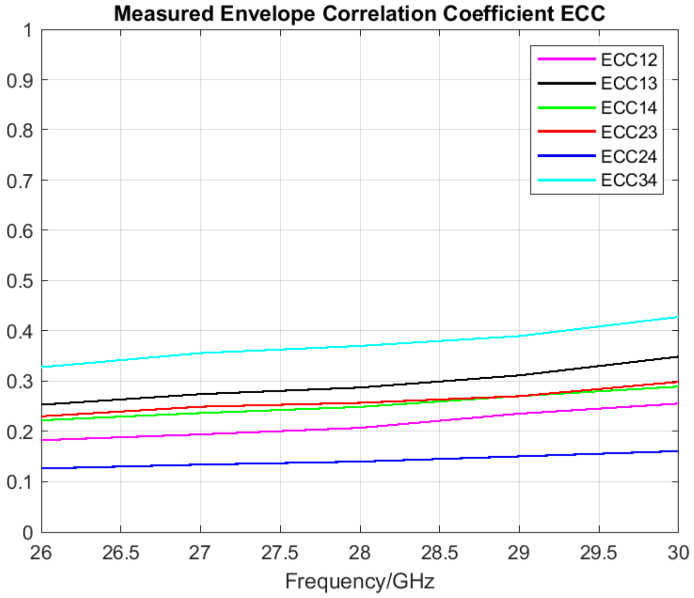

(b) Measured ECC

Figure 6.29: ECC for the MIMO system

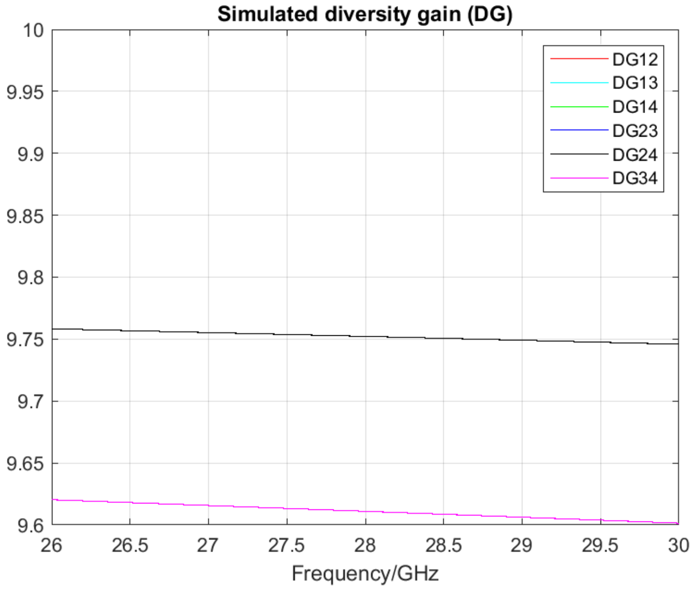

(a) Simulated DG

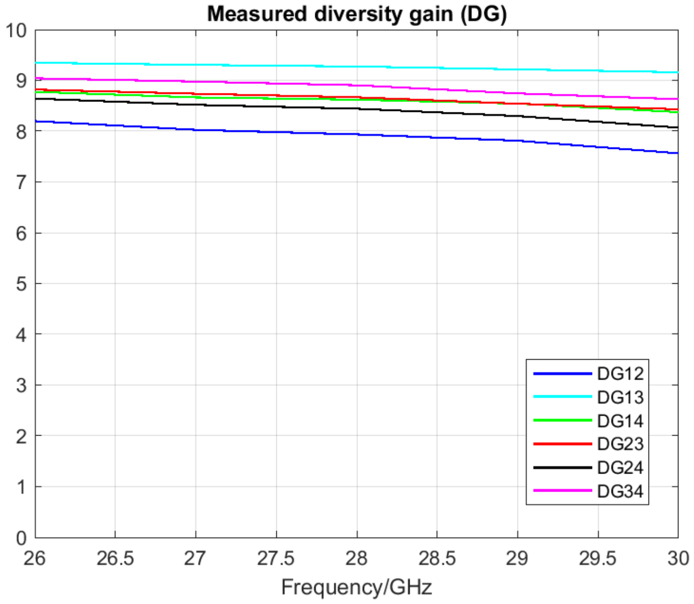

(b) Measured DG

Figure 6.30: DG of the MIMO system

6.5 Conclusions

A single antenna working at mmWave with LP was investigated. It exposes an impedance bandwidth of 6%, a maximum gain of 7.07 dBi in addition to a unidirectional $\phi = 0$ °, $\theta = 0$ ° radiation. Afterwards, a 4 MIMO system was designed and investigated with similar characteristics as the single antenna element, including LP. The design considered a common grounded plane within all the antenna structures. The resulting scattering parameters impedance bandwidth for each individual case were S_{11} of 6%, S_{22} of 5 %, S_{33} of 4.46 % and S_{44} of 5.28 %. The main attribution of the measured differences is related to the RDRA's alignment at the assembly stage. Moreover, two mutual coupling reduction techniques were investigated throughout this work. The first one is by modifying the components position, and the second one is by adding slot etched slots on the GP. The inter port coefficient reflection losses for adjacent ports S_{13}, S_{31}, S_{23}, S_{32}, S_{24}, S_{42}, S_{14}, S_{41} exposed a maximum reduction of -12 dB within the frequency range. Complementary, parallel ports S_{12}, S_{21}, S_{34}, S_{43} exposes a maximum range reduction of -7 to -14dB as a result of applying both before mentioned techniques. In terms of the antenna radiation pattern behaviour, it was found that there was a natural splitting on the beam width for the four-port system as the frequency increased. Interestingly, some of the main challenges for the MIMO system measurements refer to the antenna fabrication tolerances, assembly, manipulation, and scanning system alignment. It is suggested to measure each component before assembly as well as the use of thin double-sided tape in addition to highlighting the dielectric resonator position on its corresponding board. It is crucial to be aware of the proper handling of the components due to their fragility and effect on the antenna behaviour at mmWave. Further tests were desired but limited due to the available resources. A suitable application for the antenna system described in this chapter is its integration as a 5G/5GNR wireless module within on-chip mobile hardware.

Chapter 7

Circularly Polarised Rectangular DRA for mmWave MIMO

Throughout this chapter, RDRAs at the mmWave spectrum with circular polarisation are investigated due to its benefitial size and performance to work within a MIMO system.

7.1 CP mmWave RDRA

Circular polarisation on antenna design results in a potential feature for mmWave antennas to potentially mitigate channel environmental inconveniences when wireless communication is established. Antennas with this particular type of propagation can be an ideal solution in applications such as mobile, by reducing the multi-path interference between the Base station and the End user for MIMO systems, satellite, dealing with signal orientation changes caused by the same satellite rotation, and also shielding the transmission in a couple of routes, medical, by allowing the body communication devices to have freedom of movement without limiting signal transmission performance within human body, automotive, by ensuring reliable communication in between the vehicle and its controller [120].
This chapter presents a CP antenna for a four-element MIMO system. Three iterations of the main design will be investigated.

7.1.1 Single RDRA element mmWave CP

A CP single RDRA antenna design with a $\lambda_0 = 10.70$ mm, based on Eq. 2.25 in Chapter 2, is calculated. The antenna design substrate material was chosen as Rogers RT5880 with $\epsilon_r = 2.2$, size of $1.308\lambda_0 \times 1.308\lambda_0 \times 0.047\lambda_0$. The copper layers have a 35 μm thickness. The feeding mechanism consists of an aperture rhombus, for generating a CP due to the length difference between its diagonals, slot illustrated in Fig. 7.1a, the larger diagonal size is $0.166\lambda_0$ and, the smaller diagonal is $0.0579\lambda_0$. The RDRA is made of Alumina $\epsilon_r = 9.9$ and its dimensions are $0.1457\lambda_0 \times 0.1523\lambda_0 \times 0.315\lambda_0$ at a frequency of 28 GHz. Complementary, Fig.7.1a shows the top view of the antenna without the DRA, and Fig.7.1b shows the entire transparent structure.

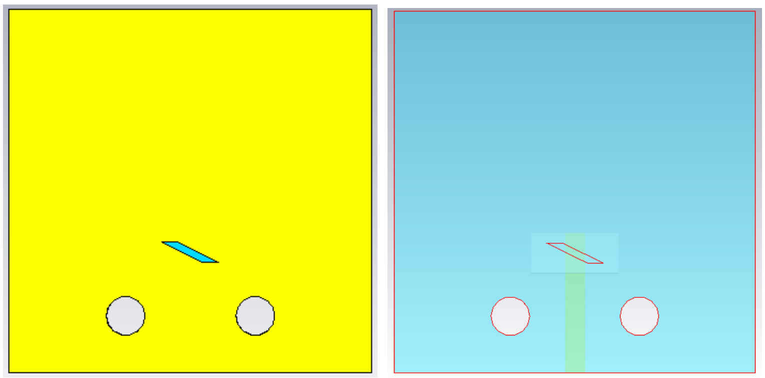
(a) Antenna front view without RDRA
(b) Antenna transparent structure

Figure 7.1: RDRA with circular polarisation

From top to bottom, Fig. 7.2 shows in white the Rectangular DRA located above of the rhombus aperture, generating the antenna's CP. In the middle of the structure, the GP can be observed followed by the substrate, and on the bottom is the transmission line which is aligned with the slot aperture to generate coupling by reducing the admittance between the RDR and the substrate. The admittance is key for achieving an adequate impedance bandwidth controlled by the length of the stub s defined in Chapter 4, Fig. 2.10a

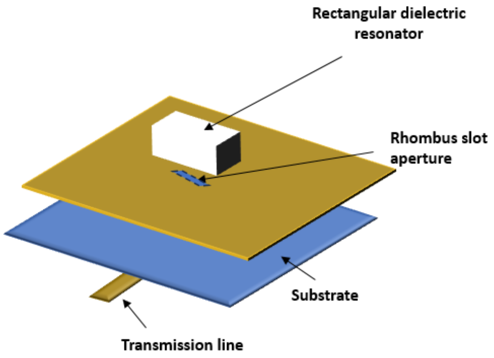

Figure 7.2: CP RDRA antenna design in layers

7.2 Fabrication considerations

The PCB was fabricated based on the IPC2221 standard tolerances. The antennas consist of PCB, SMA connector, and RDRA. The utilised connectors were similar to the design discussed in the previous chapter. The RDRA dimension tolerances are illustrated in Table. 7.1. When comparing them with the LP samples, it can be noted that there is a wider fabrication tolerance which will depend directly on the cutting process in addition to the raw ceramic conditions.

Table 7.1: mmWave ceramic rectangular resonator

Variable name	dimension (Δmm)
width (a)	0.13
length (c)	0.16
thickness (b)	0.13
permittivity	1

As part of an initial protocol, the RDRA was measured with the vernier shown in Fig. 7.3b is used to confirm the dimensions of each sample.

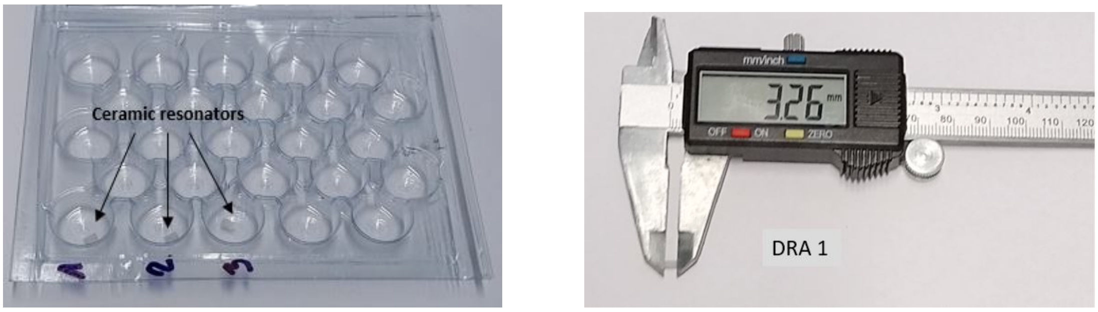

(a) Rectangular ceramic pieces

(b) Ceramic piece measured size

Figure 7.3: Ceramic rectangular resonator at mmWave frequencies

The rhombus slot must be located at the middle of the DRA lower side. Therefore, the DRA position has been highlighted with a white silkscreen to reduce uncertainties within the measurements. Fig. 7.4a illustrates the PCB silkscreen labelling. Fig. 7.4b illustrates the fabricated and assembled antenna prototype.

7.3 Single RDRA element

7.3.1 S-parameters

The single RDRA antenna, the reflection coefficient was first measured. As illustrated in Fig. 7.5, the simulated results expose an impedance bandwidth of 13.34 % highlighting

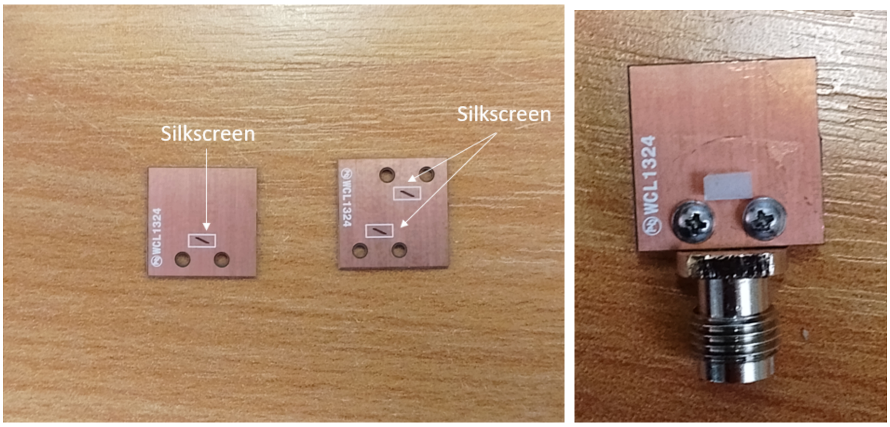

(a) Fabricated single and two antenna elements (b) Fabricated single antenna element

Figure 7.4: mmWave ceramic rectangular resonator antenna

two resonant modes at 26 and 28 GHz. Measured results show an impedance bandwidth of 8.49 % with a resonant frequency at approximately 29 GHz. A reduction in bandwidth and a frequency shift can be attributed to the RDRA tolerance of the fabricated ceramic permittivity.

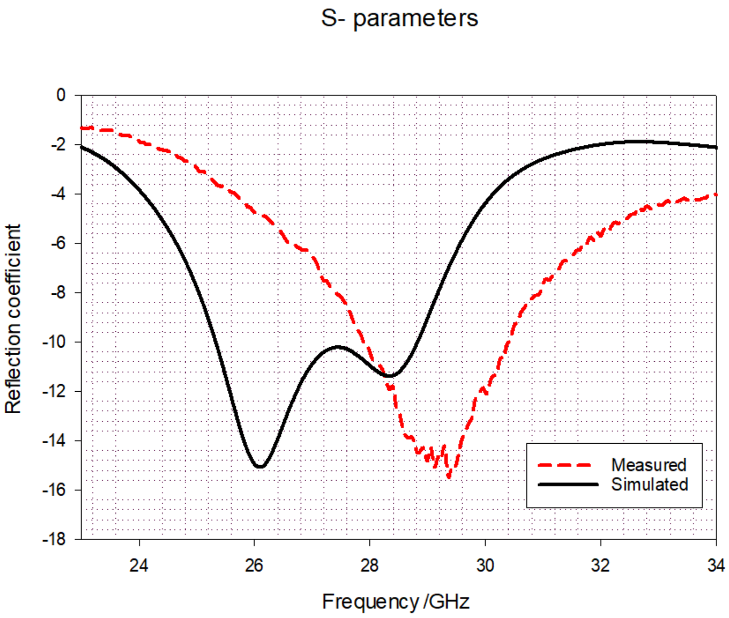

Figure 7.5: Reflection coefficients for CP DRA.

7.3.2 Radiation pattern

By simulating the radiation pattern, it is possible to observe a unidirectional radiation pattern with a main beam direction $\phi = 0\,^{\circ}$, $\theta = 0\,^{\circ}$, at the resonant frequency. Since the antenna is circularly polarised, its radiation pattern will propagate in a circular pattern on the left-hand direction defined by design E_{LHCP} according to the rhombus position. The measured radiation pattern at the resonant frequency of 29 GHz at ϕ = 0 °, θ = 0 ° is presented in Fig. 7.6a. It can be noted that the simulated pattern indicates the maximum point on the radiation. There is an existing titling of the maximum beam direction due to alignment uncertainties and variations in the uniform radiation pattern attributed to the measurement environment. Fig 7.6b presents the E_{RHCP} pattern for the antenna, where its measured radiation differs in magnitude but has similar behaviour; there is an existent lump at θ = -90 ° due to the anechoic chamber system. Next, ϕ = 90 ° was investigated to observe the antenna radiation. Fig. 7.6c shows good agreement with simulations and measurements, the previously mentioned lump remains presented for this case. Complementary, Fig. 7.6d illustrates a pattern closer to the simulated case for E_R. One interesting finding is that the direction of the rhombus-shaped aperture indicates the direction of the polarisation propagation. Hence, if the antenna is mirrored with the reference to its position, the propagation will be altered in the opposite direction. This consideration is crucial when designing MIMO systems of this kind. Simulated and measured results are in reasonable agreement.

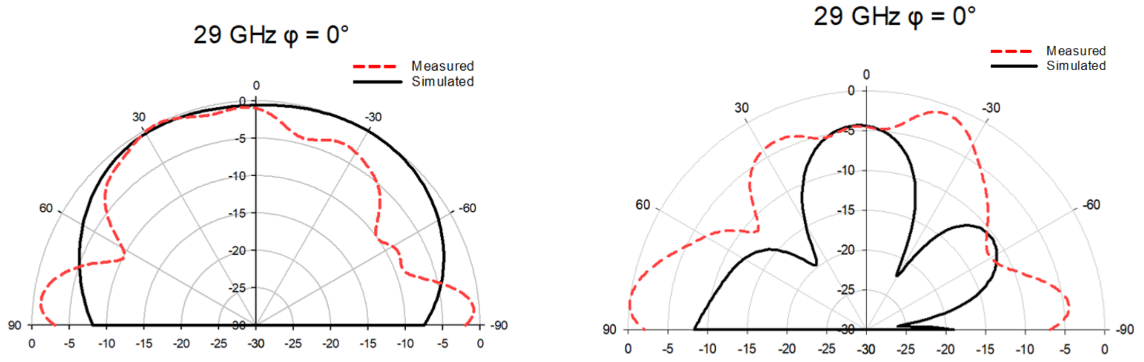

(a) E_L (b) E_R

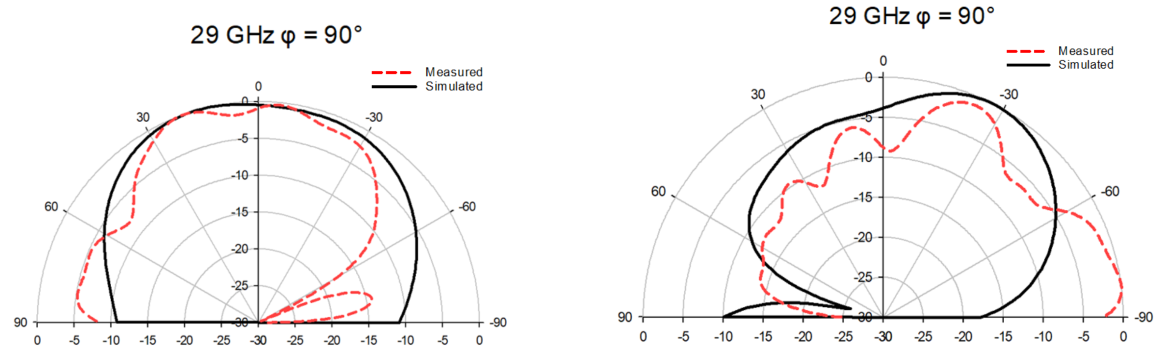

(c) E_L (d) E_R

Figure 7.6: Measured and simulated radiation patterns for single antenna

7.3.3 Antenna gain

The antenna realized gain was measured and compared with simulations as shown in Fig. 7.7. It was considered at the maximum radiation direction, $\phi = 0$ ° and $\theta =$ -30 °, according to Fig. 7.6. The tilting on the beam is attributed to the alignment in measurements within the transmitter and receiver antennas. A maximum gain of $\sim$ 5.05 dBi was observed. A maximum gain difference between simulations and measurements of 2 dBi is attributed to losses in adaptors, and connectors.

7.3.4 Axial ratio

Fig. 7.8 shows the comparisons between the simulated and measured axial ratio. The simulated case exposes a bandwidth of 6.33 % compared to measurements that show an increment of the axial ratio bandwidth to 10.63% which also considers the frequency shift and an increment in its bandwidth. This difference can be attributed to fabrication and scanning tolerances.

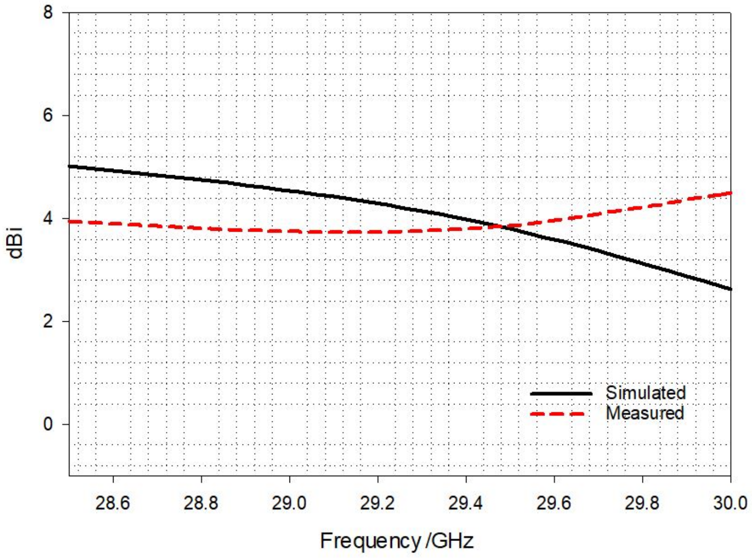

Figure 7.7: Realized gain for the single antenna

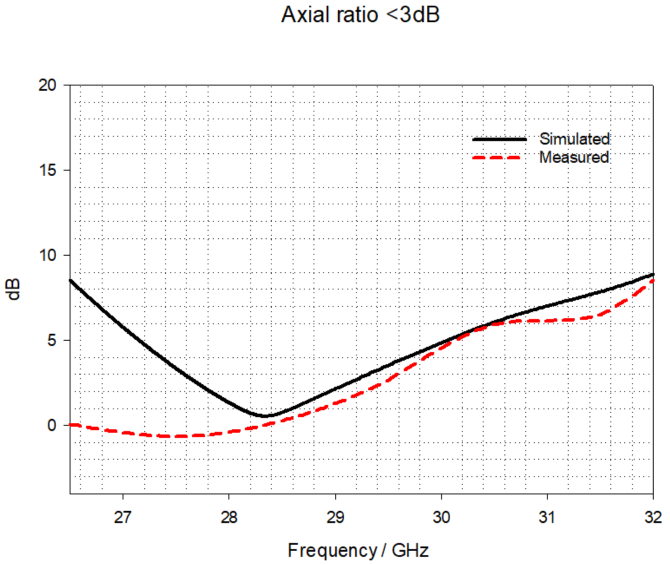

Figure 7.8: CP at the main lobe direction

7.4 Two RDRA mmWave CP MIMO

Two RDRA's with the same characteristics, as previously designed, were added to the design as a first iteration. RDRA positioning was employed to reduce the mutual coupling between the two elements due to the shared GP. In terms of design considerations, each antenna element was shifted 0.166 λ_0 to the *-x-axis* direction starting from the middle edge of the substrate according to Fig. 7.9. The second rhombus aperture was mirrored with the first antenna from the centre of the PCB. The distance from the middle to the middle point of each RDRA is approximately $0.55\lambda_0$ with the previously mentioned shift which complies with the minimum design distance consideration of $\frac{\lambda_0}{2}$ best practice.

Figure 7.9: Two MIMO element fabricated design

7.4.1 S-parameters

This section investigated the reflection coefficients of two RDRA's. The S-parameters for ports 1 and 2 simulated results show an impedance bandwidth of 11.82 %. In the case of measurements, S_{11} reflects an impedance bandwidth of 12.98 %. Complementary, S_{22} shows an impedance bandwidth of 13.62 %. A maximum difference of 1.8 % for both port measurements reflected in an increment of bandwidth. These differences can be attributed to standardized 50 Ω calibrated physical interfaces. A couple of resonant frequencies can be observed at 26 GHz and 28 GHz for both antenna ports. Fig. 7.10a and Fig. 7.10b illustrate the reflection coefficients of ports 1 and 2. Moreover, a frequency shift can be observed due to the fabrication and assembly tolerances.

For the case of transmission coefficients, port interactions are presented in Figs. 7.11a and 7.11b. Some observations refer to a similarity between S_{12} and S_{21} measured results with a frequency shift as expected. Moreover, in both cases, their level of coupling can initially be evaluated for its reflection coefficient value which is lower than -20dB which can be considered as a good reduction for the system. Despite the existence of a frequency shift, the impedance pattern is similar compared with its simulations.

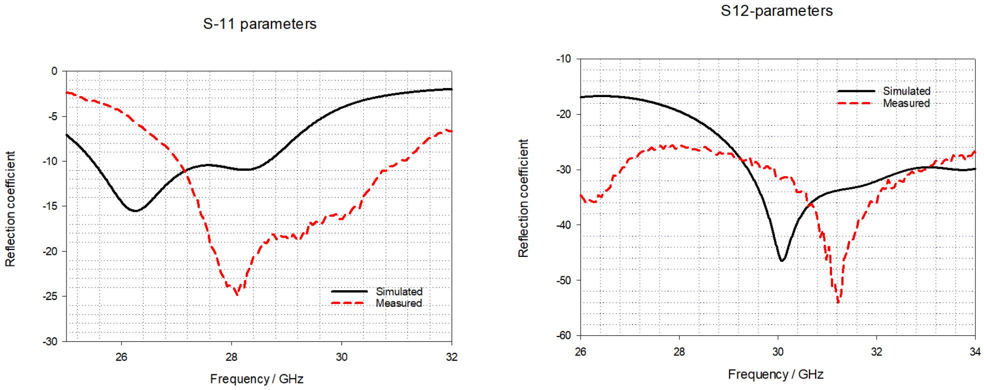

(a) S11 (b) S12

Figure 7.10: S-parameters for port 1

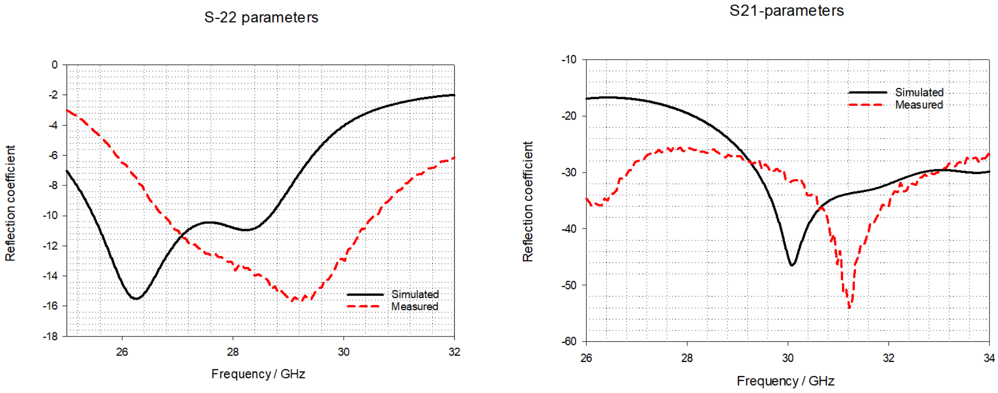

(a) S22 (b) S21

Figure 7.11: S-parameters for port 2

7.4.2 Radiation pattern

The two MIMO antennas were measured using a 4-way splitter, illustrated in Fig. 6.19a. The other two splitter ports were terminated with 50 Ω loads as illustrated in Fig. 7.12.

ϕ = 0 ° to ϕ = 90 ° have been considered to identify the degree where the maximum radiation point is to then find the beam maxima gain and evaluate if the circular polarisation is present on this direction. The maximum achieved realized gain is identified as ~6.34 dBi for simulations and measurements at approximately the direction θ= 35 °. Fig. 7.13a and Fig. 7.13c present the radiation pattern of a couple of left-hand sides circularly polarised antennas, where E_{LHCP} radiation patterns at $\phi = 0$ ° and $\phi = 90$ ° agree with the simulations. There is an evident null presented at $\phi = 0$ ° and $\theta = 0$ ° which represents the point where the main beam is split on the radiation pattern. Moreover, E_{RHCP} for both antennas show a similar pattern to the simulated case, it is noticeable that the θ = -90° lump is present for the measured results. Complementary, a tilting with E_{RHCP} is noticeable in Fig. 7.13b and

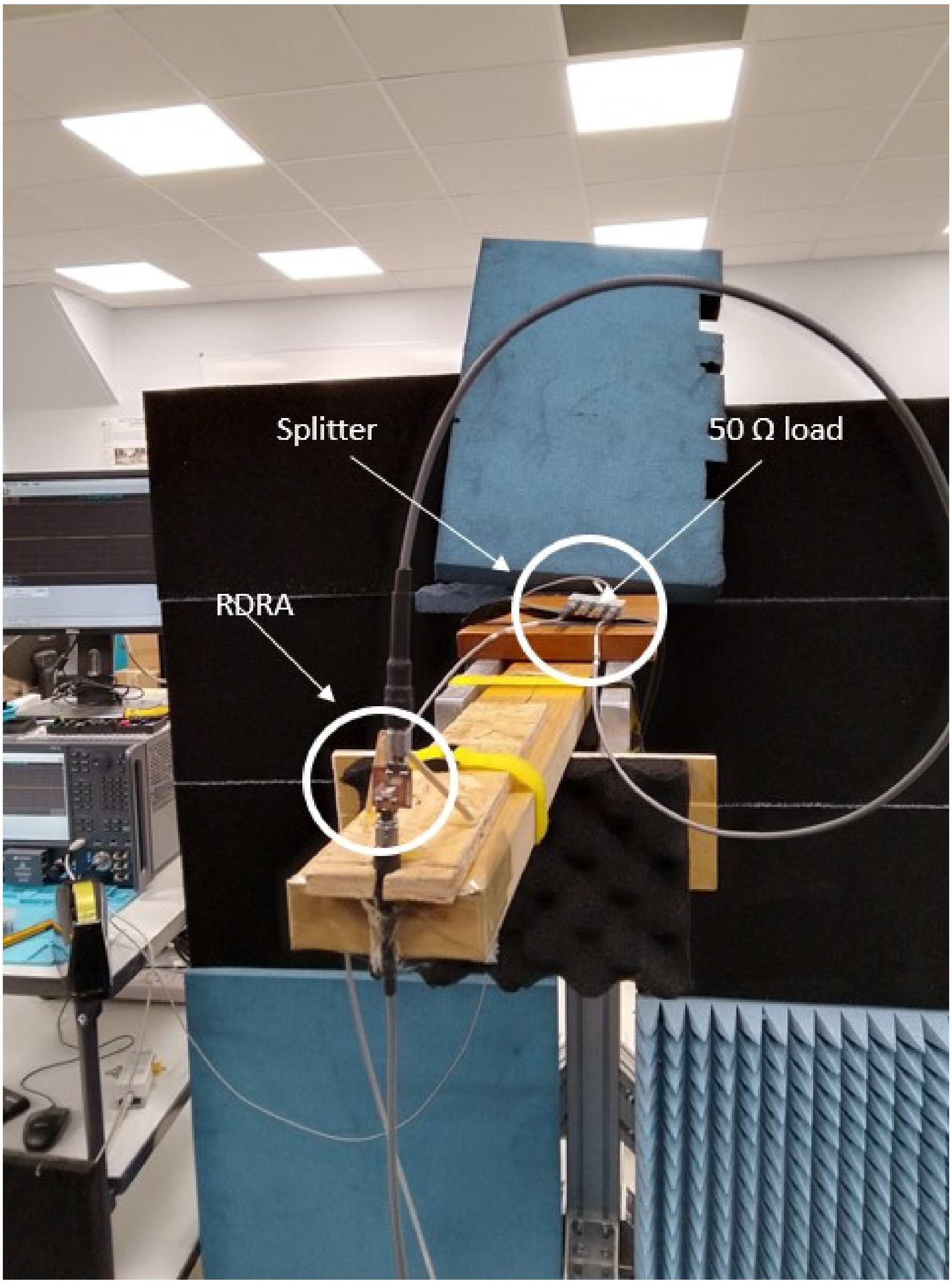

Figure 7.12: MIMO experiment set up

Fig. 7.13d which can be attributed to the scanning system alignment.

Once the maximum radiation point was identified, the Azimuth angle was investigated to identify if CP is preserved for each one of the cases. Fig. 7.14 shows the E_{LHCP} and E_{RHCP} radiation patterns, specifically at ϕ =50 ° and ϕ =-130 °, due to a frontal deviation on the radiation pattern when both antennas are radiating, resulting in an opposite direction splitting. It is relevant to mention that measurements were tested in a range of ϕ = -90 ° and ϕ = 90 ° which indicates half of the polar plane of Fig. 7.14. Fig. 7.14a illustrates

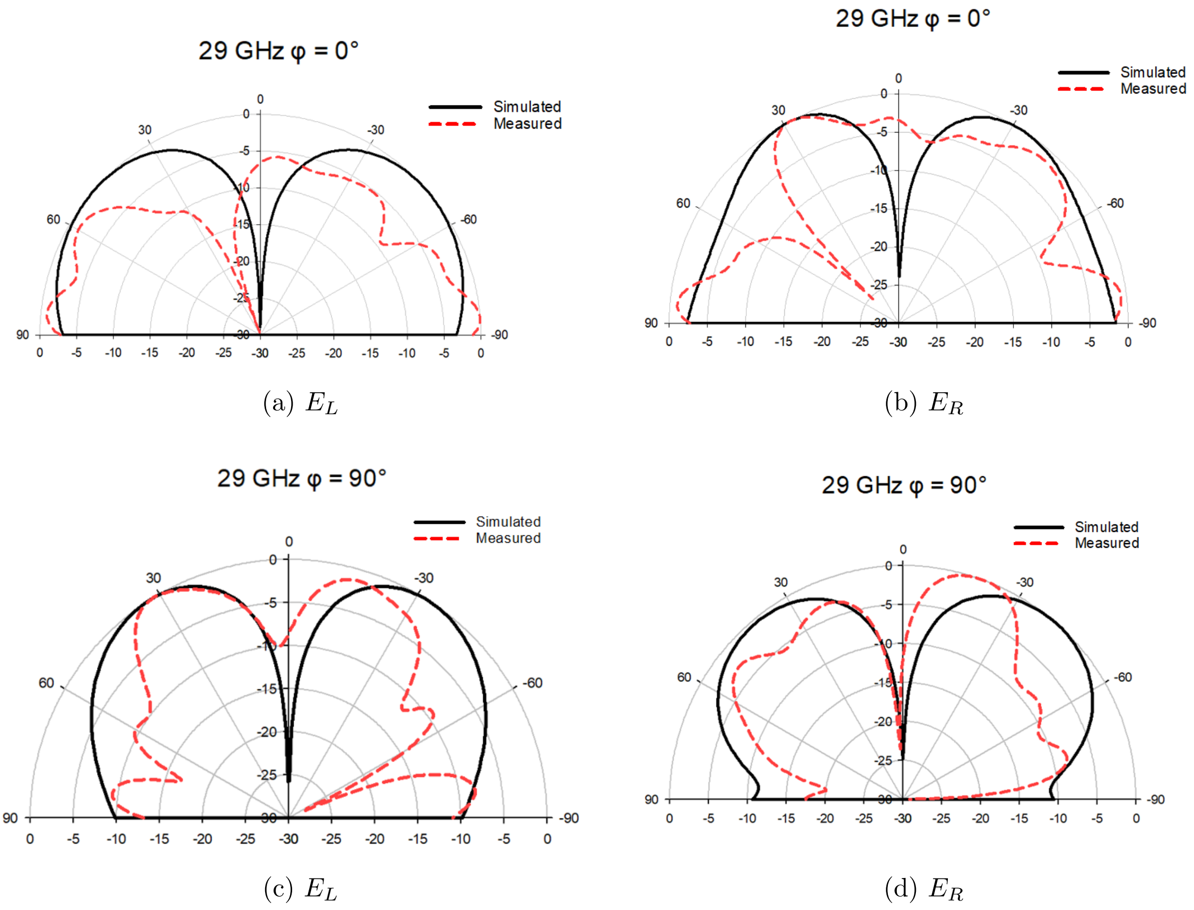

(a) E_L (b) E_R

(c) E_L (d) E_R

Figure 7.13: Measured and simulated radiation patterns for two MIMO antennas

a similarity between simulated and measured results where there is a slight rotation for approximately 20 ° - 30 ° attributed to the unwanted rotation of the antenna due to the connector assembly when positioning the antenna. Fig. 7.14b presents a similar behaviour. In both cases, there is a good agreement between simulated and measured results.

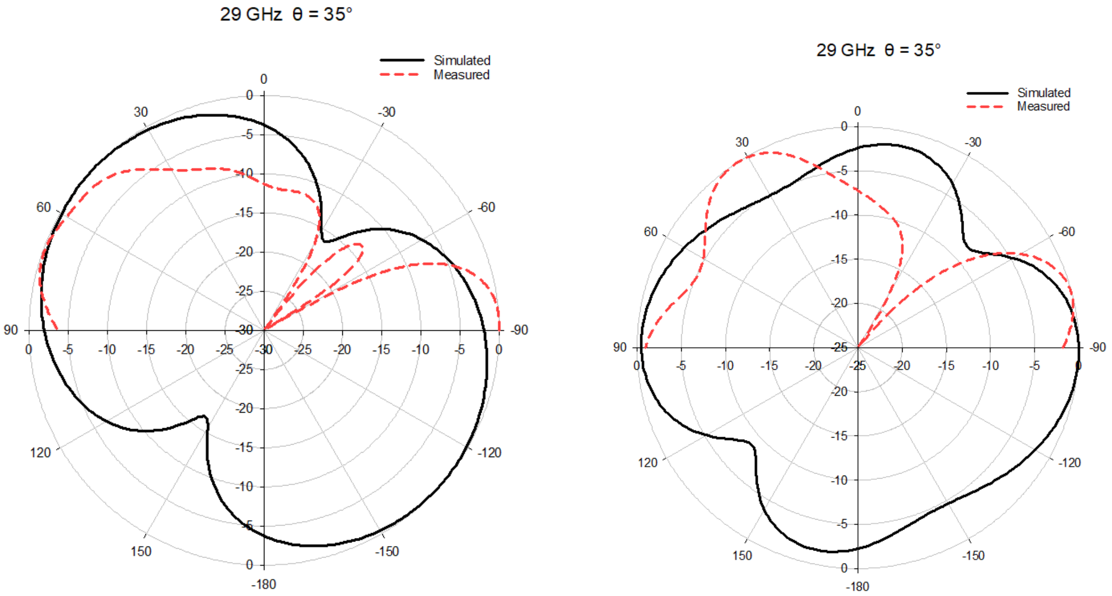

(a) E_{LHCP}

(b) E_{RHCP}

Figure 7.14: Two element MIMO radiation patterns

From a 3D perspective view, the CP MIMO can be illustrated in Fig. 7.15. Each antenna has a clear radiation null representing the split at $\phi = 0\ °$, $\theta = 0\ °$.

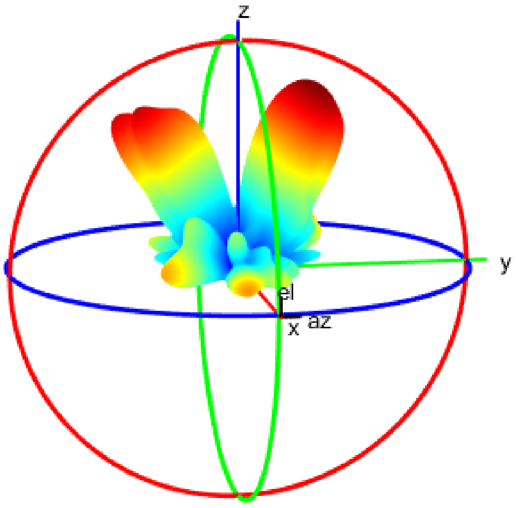

Figure 7.15: 3D radiation pattern of the two MIMO elements

7.4.3 Antenna gain

Two radiation beam maxima are considered for this case, the first one at ϕ = -89 ° illustrated in Fig. 7.16. It is relevant to consider that the measurements were scanned at an angle maxima of ϕ = -90 °. At the resonant frequency, the maximum antenna gain of the first antenna is ~ 6.20 dBi. Some differences are expressed between simulated and measured results which are attributed to physical connector losses.

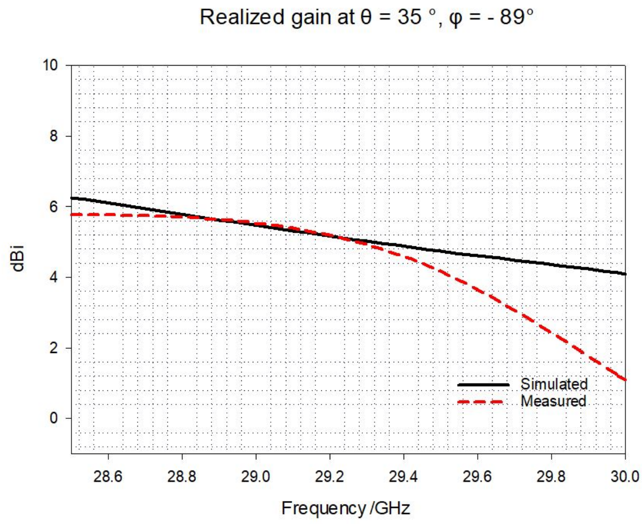

Figure 7.16: Realized gain at ϕ = -89 ° direction

The second maxima is indicated in simulations at ϕ = 50 °. A similar maximum gain of ~ 6.20 dBi is expected. Fig.7.17 illustrates the realized gain for the second case.

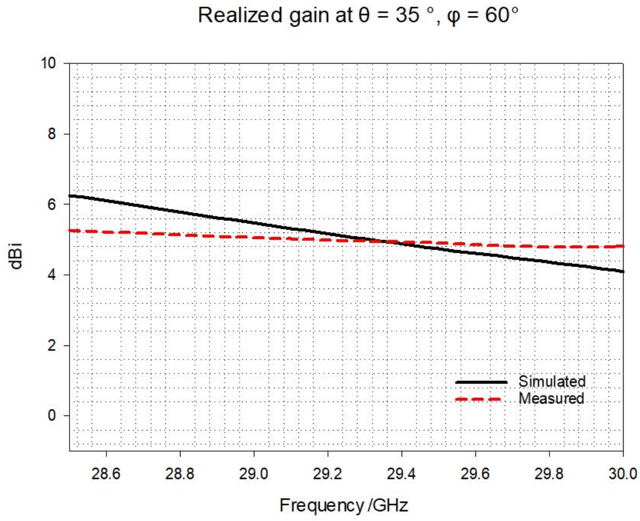

Figure 7.17: Realized gain at ϕ = 60 ° direction

7.4.4 Axial ratio

After determining the main lobe radiation directions, an investigation per antenna main radiation beam within frequency was conducted for determining the existence of axial ratio of < 3 dB. Fig. 7.18 presents the simulated and measured axial ratio for the first antenna at $\theta =$ 50 °. The antenna axial ratio, <3 dB bandwidth, is 8.16 % by simulation. The corresponding measured bandwidth exposes a 10.71 % for both directions. A similar behaviour as the axial ratio for the single element can be observed in terms of an increment in bandwidth, moreover a frequency shift. When comparing the results, the axial ratio overlaps the impedance bandwidth mentioned in section 5.5.1.

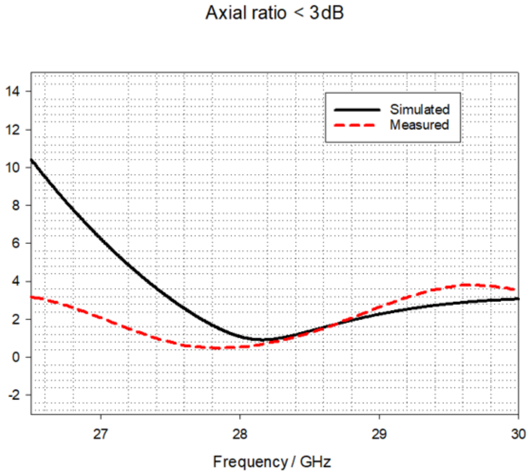

Figure 7.18: Axial ratio at θ = 50 °

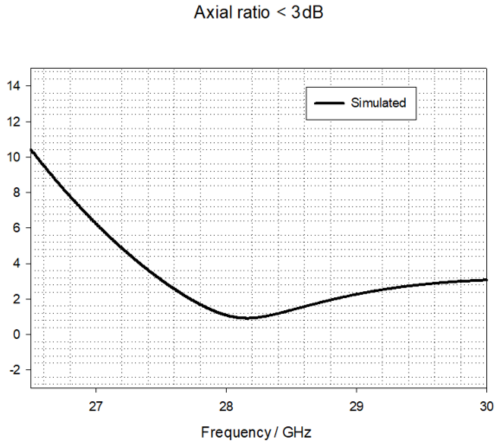

Figure 7.19: Axial ratio θ = -120 °

7.5 Four RDRA mmWave CP MIMO

7.5.1 S-parameters

Due to the potential of the two element design, the last iteration for the CP MIMO structure consisted of adding two more elements to the system as for the LP design, as the intention in this chapter is to design and investigate a 4 element MIMO with CP prototype working at mmWave demonstrating simplicity, size reduction, a radiation pattern control behaviour, as well as an acceptable level of mutual coupling between elements.
Firstly, and considering the addition of two more elements to the system, $1.308\lambda_0$ substrate size was considered, secondly $1.588\lambda_0$, thirdly $1.775\lambda_0$. The initial four element design is illustrated in Fig. 7.20.

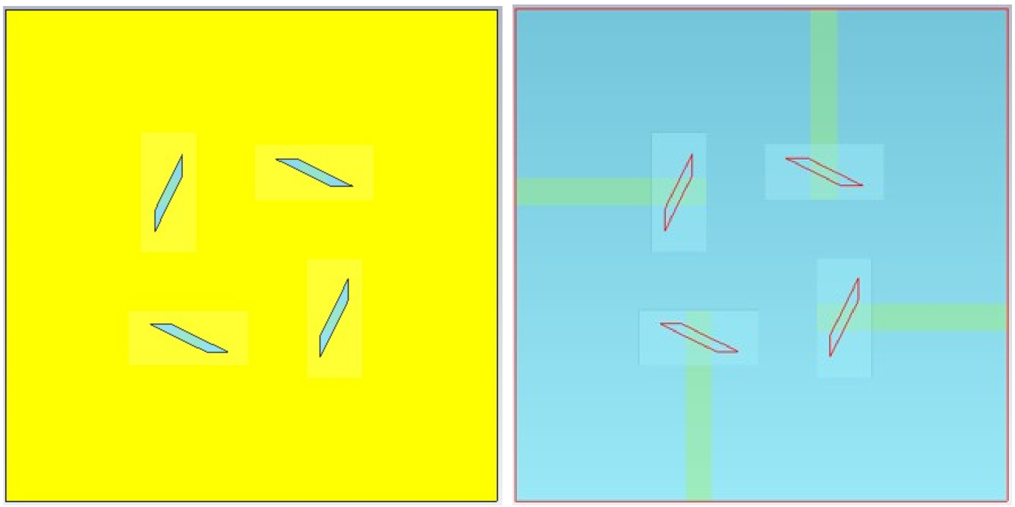

(a) Antenna front view without RDRA (b) Antenna transparent overview

Figure 7.20: 4 RDRAs CP MIMO

Next, reflection coefficients were investigated with different substrate sizes to determine the best performance for the MIMO in terms of the element's spacing.

Focusing on the antenna impedance bandwidth, the simulated S_{11} is 9.39 %. As soon as the antenna size was increased, the original impedance bandwidth had no significant change from 14.49 % to 14.03 % as illustrated in Fig.7.21a. After comparing the three cases, there is an important power reduction when increasing the antenna size which impacts the impedance matching reflected on the addition of a second resonant frequency to the system at 28.2 GHz. Three antenna size cases, 14, 17, and 19 mm, will be presented below to report the effect on the overall MIMO antenna system.

Moving on S_{12}, the increment in size reduced significantly the reflection coefficient by -12 dB on the frequency range. There is not a major noticeable effect once the antenna size is increased from $1.588\lambda_0$ to $1.775\lambda_0$, however, an improvement having a minimum reduction

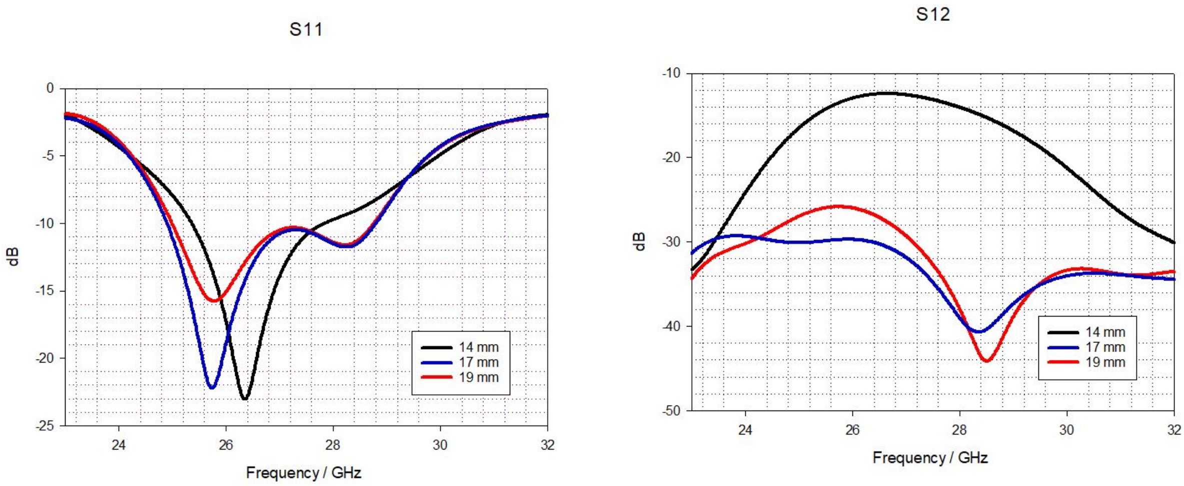

(a) S11 (b) S12

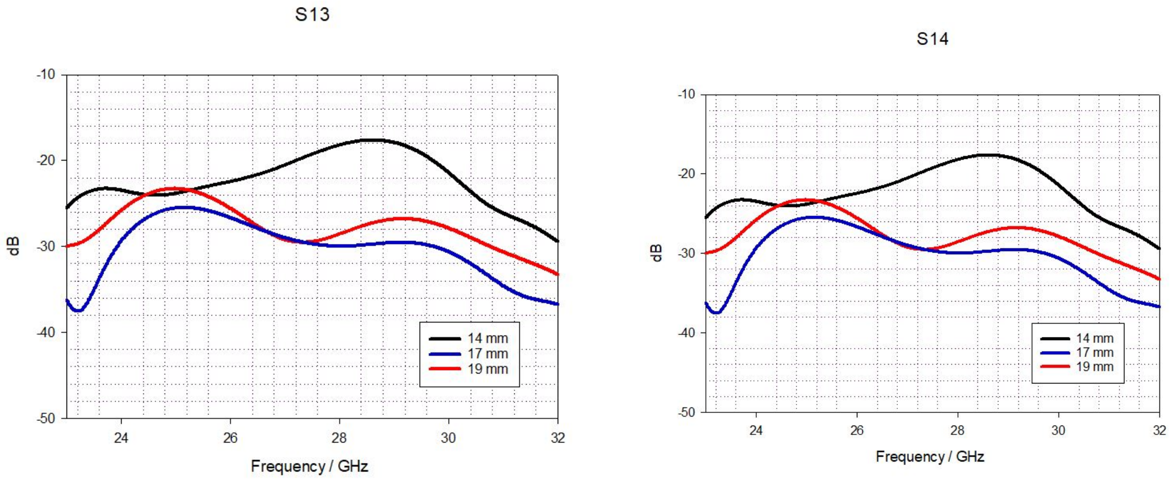

(c) S13 (d) S14

Figure 7.21: Scattering parameters when port 1 is fed.

level is -26 dB is present. Considering < -20 dB an acceptable threshold for achieving an adequate power loss level, approximately < 0.1 Watts in linear scale, the case of Fig.7.21b demonstrates a poor inter port reflection coefficient value for the first case.

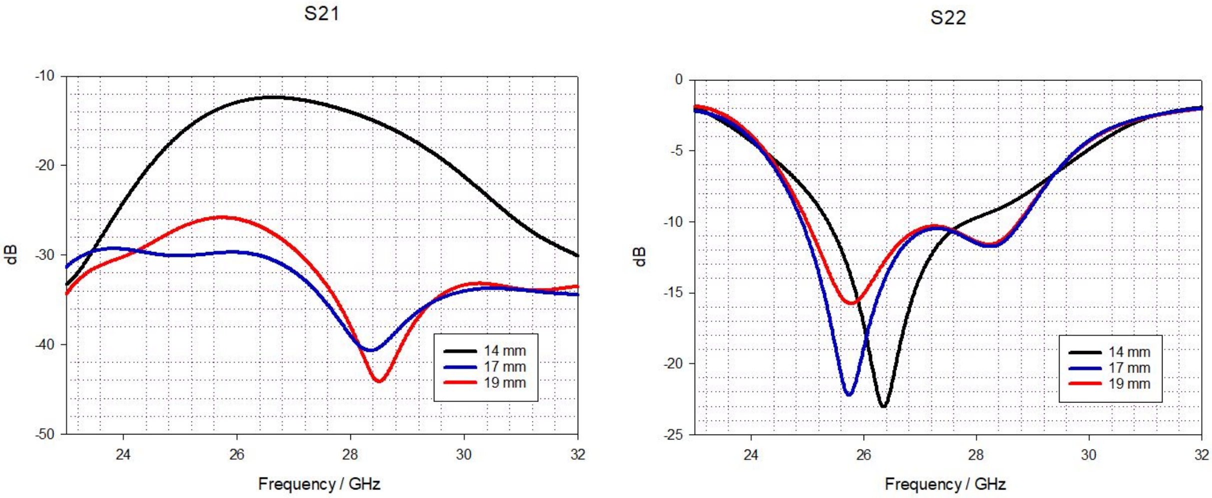

(a) S21 (b) S22

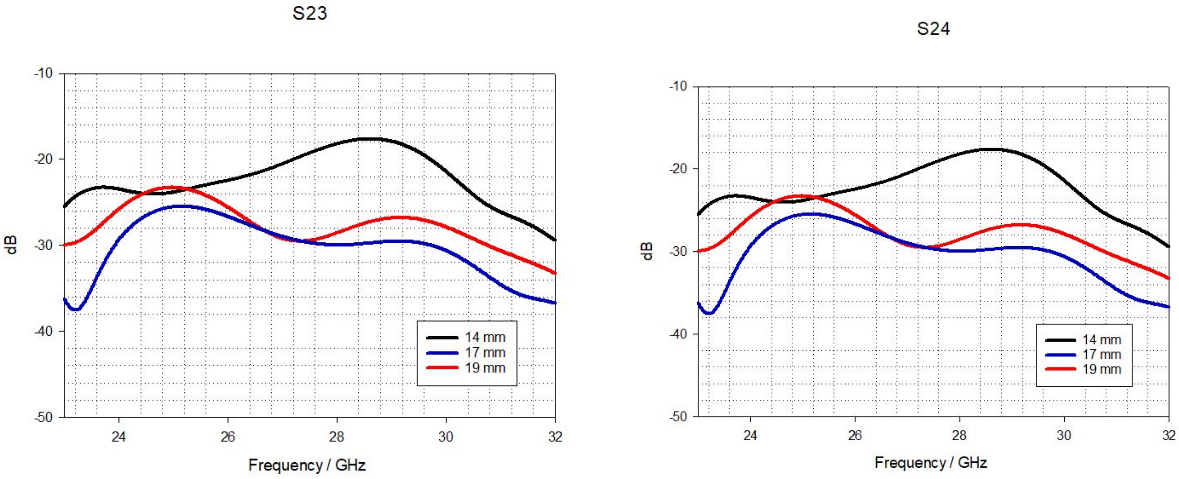

(c) S23 (d) S24

Figure 7.22: Scattering parameters when port 2 is fed.

Fig. 7.22b illustrates the secondary port impedance bandwidth, its percentage is the same as ports 1,3, and 4 by design. Fig. 7.22a exposes a maximum reduction in reflection coefficients of approximately -12 dB. Figs. 7.22c and 7.22d present a similar reduction of approximately <-10 dB on the frequency range.

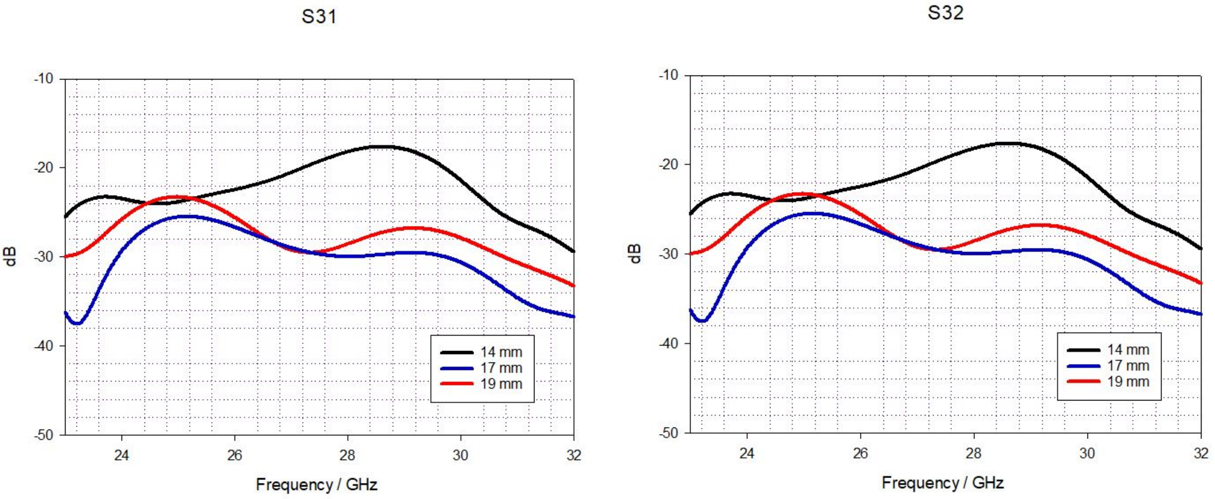

(a) S31 (b) S32

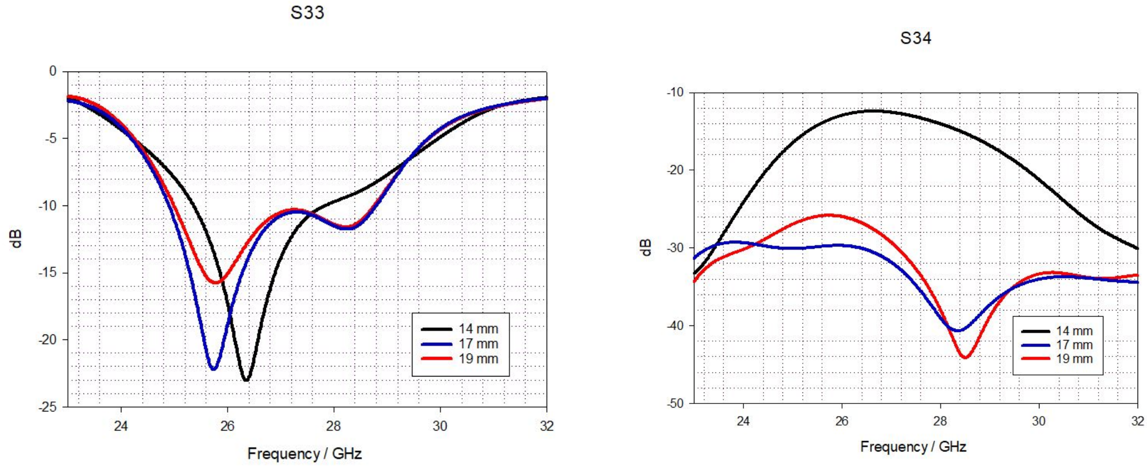

(c) S33 (d) S34

Figure 7.23: Scattering parameters when port 3 is fed.

Fig. 7.23 illustrates the reflection coefficients for the third antenna on the MIMO system. Figs. 7.23a and 7.23b present a similar reduction of approximately <-10 dB on the frequency range. Complementary, Fig. 7.23c shows the same impedance bandwidth as 7.22b, and Fig. 7.23d presents a maximum of -12 dB reduction due to the elements spacing.
Finally, reflection coefficients for port 4 are illustrated in Fig.7.24. Similarity between Fig. 7.24a and Fig. 7.24b is expected. An impedance bandwidth of 9.39 %,14.03 % and 14.49 % are present in Fig. 7.24d.

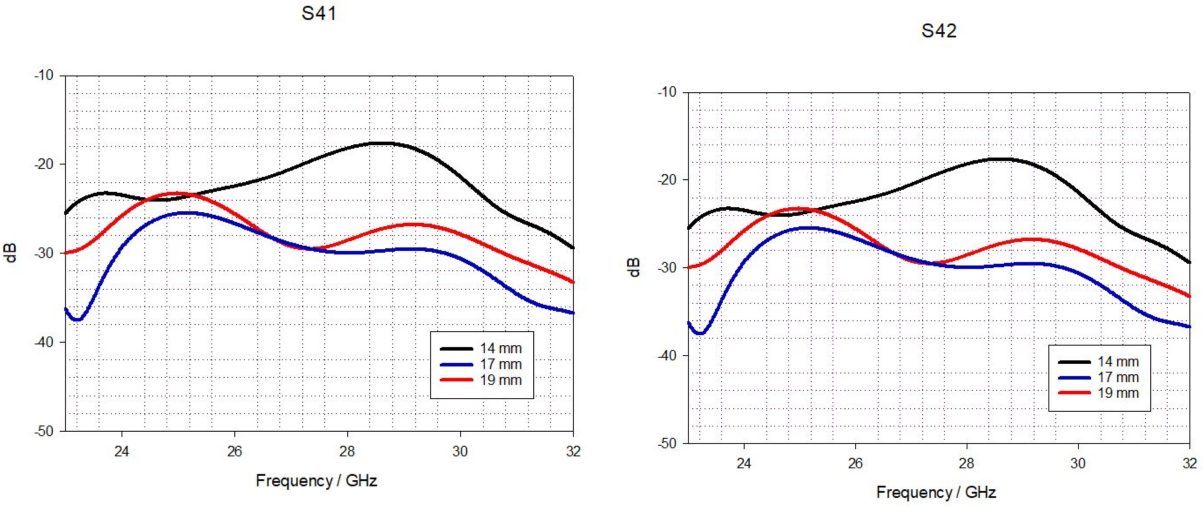

(a) S41 (b) S42

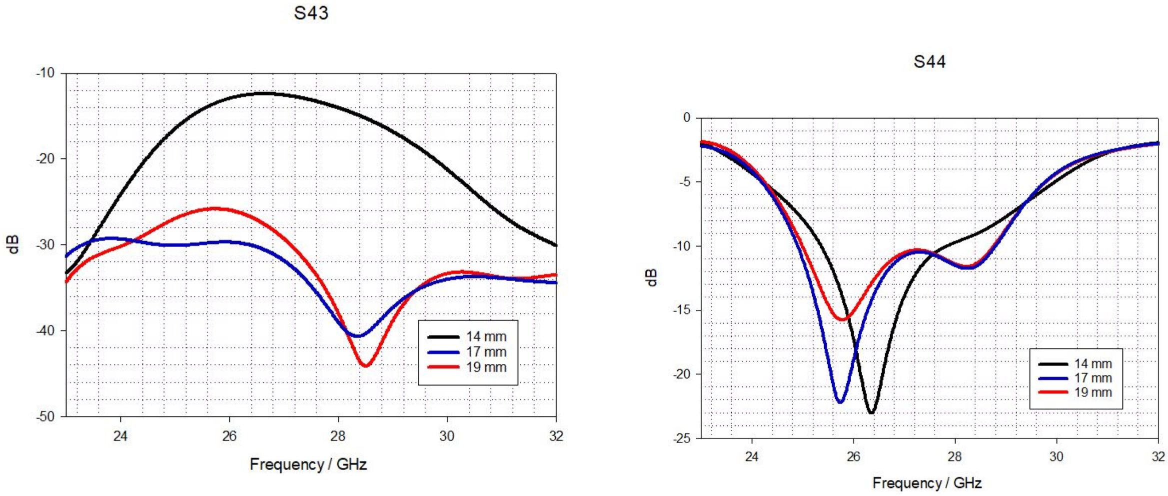

(c) S43 (d) S44

Figure 7.24: Scattering parameters when port 4 is fed.

Since the four antenna elements are positioned at 0 °, 90°, 180°, 270° on the system, the reflection coefficients present the same behaviour for the cases of S_{21}, S_{22}, S_{23}, S_{24} shown in Fig. 7.22. When considering the parallel elements for the MIMO system based on Fig. 6.10 labelling, S_{12}, S_{21}, S_{34}, S_{43} reflection coefficients will show a similar behaviour. Complementary, the perpendicular elements, S_{13}, S_{14}, S_{23}, S_{24}, S_{31}, S_{32}, S_{41} and S_{42}, present the same behaviour.

7.5.2 Radiation pattern

The MIMO antenna designs with $1.588\lambda_0$ and $1.775\lambda_0$ substrate size were investigated and compared below. The $1.308\lambda_0$ design will be discarded due to the poor reflection coefficient results.

The $1.588\lambda_0$ design radiation patterns will be discussed first. Fig. 7.27a illustrates an antenna with CP, with a predominant propagation direction E_{LHCP}. There is an existent null with a split at $\phi = 0°$ and $\theta = 0°$ as the previously presented two element design. When verifying radiation stability for the radiation pattern at $\phi = 90°$, a similar pattern is shown in Fig. 7.27b. Moreover, it can be noted in both cases that the main beam radiation is present approximately at $\theta = 37°$.

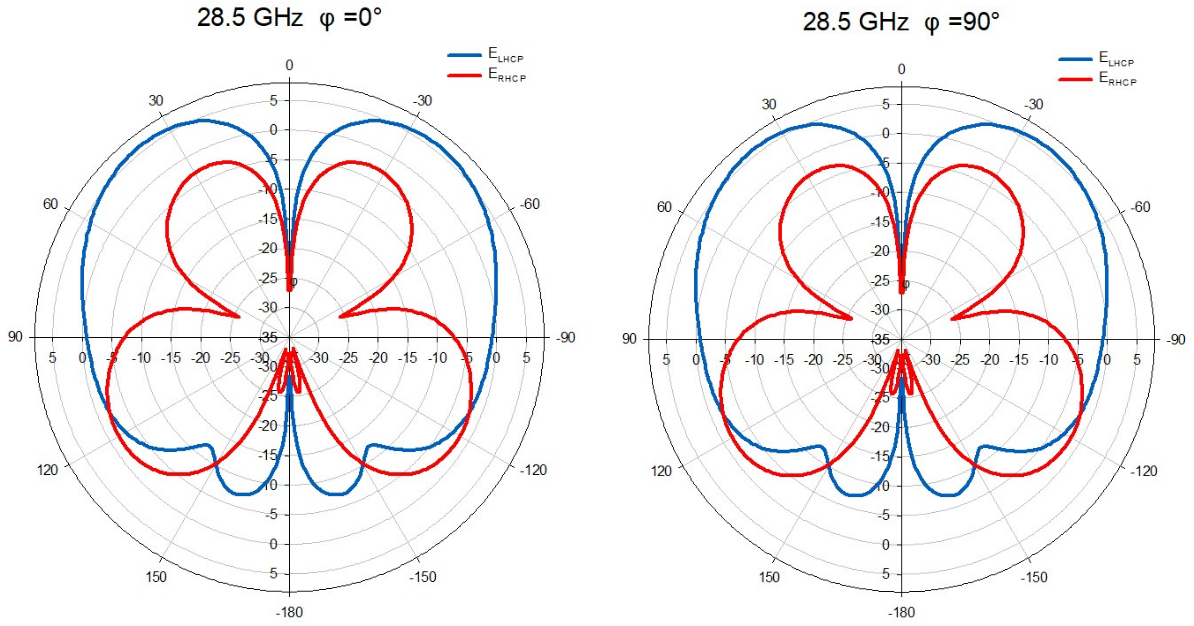

(a) $\phi = 0$ °   (b) $\phi = 90$ °

Figure 7.25: Four element MIMO radiation patterns for $1.588\lambda_0$ antenna size

The radiation pattern was analysed at $\theta = 37°$ to determine the maximum gain of each antenna, followed by its particular CP analysis. Fig. 7.26 illustrates the four simultaneous radiations of the MIMO. The main beams of the system are directed to $\theta = 7.5$ °, $\theta = 98.7$ °, $\theta =$ -82 °, $\theta =$ -172 °.

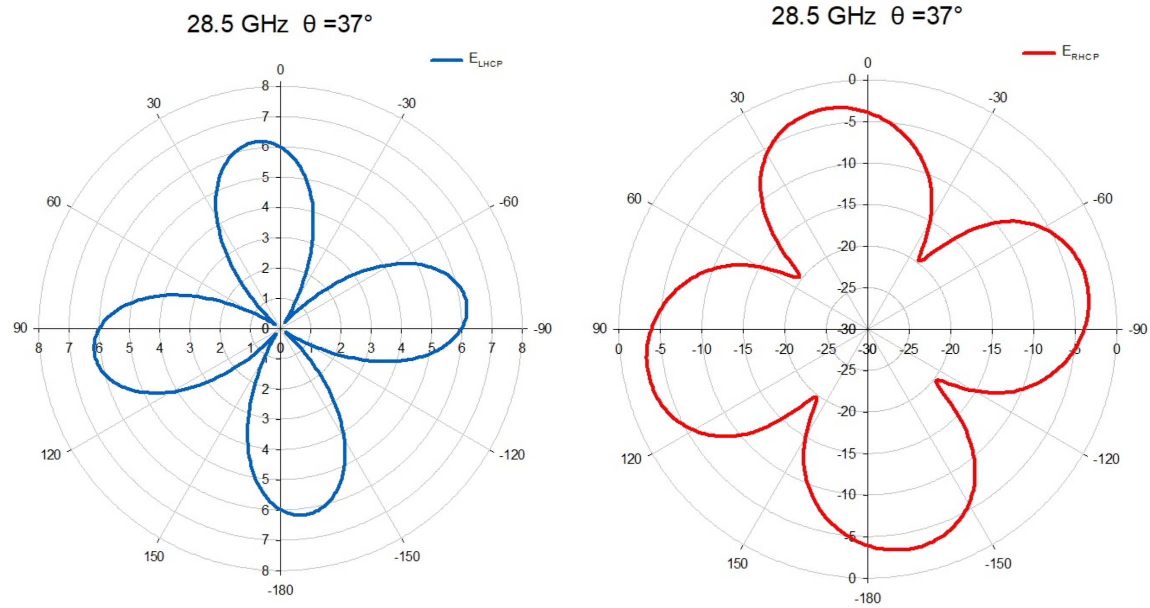

(a) E_{LHCP} (b) E_{RHCP}

Figure 7.26: Four element MIMO radiation patterns on Azimuth angle

Consequently, the $1.775\lambda_0$ design results are presented in Fig. 7.28. The left polarisation remains, but the antenna size increment resulted in a 2 ° shift of the main beam radiation direction. In contrast, the E_{RHCP} experiences a reduction of the upper beam width.

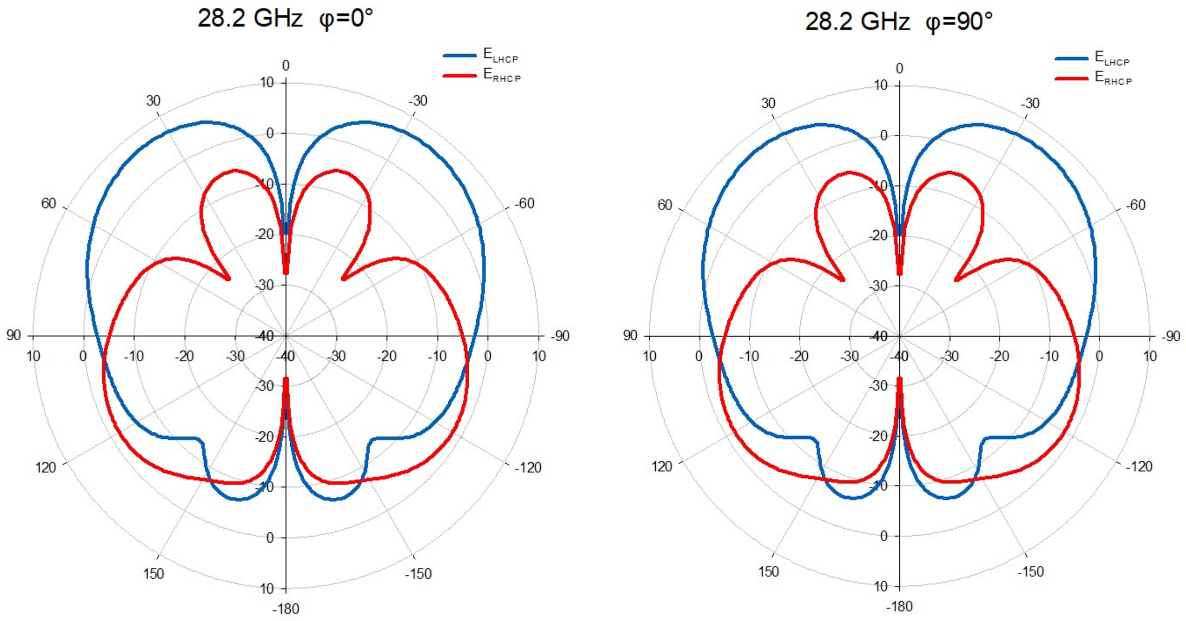

(a) $\phi = 0$ ° (b) $\phi = 90$ °

Figure 7.27: Four element MIMO radiation patterns for $1.775\lambda_0$ antenna size

Next, the corresponding radiation pattern was analysed at $\theta = 35°$ for determining the maximum gain of each antenna followed by its particular CP analysis. Fig. 7.26 illustrates the four simultaneous radiation of the MIMO. The main beams of the system are directed to θ = 11 °, θ = 100 °, θ = -79°, θ = -168 °.

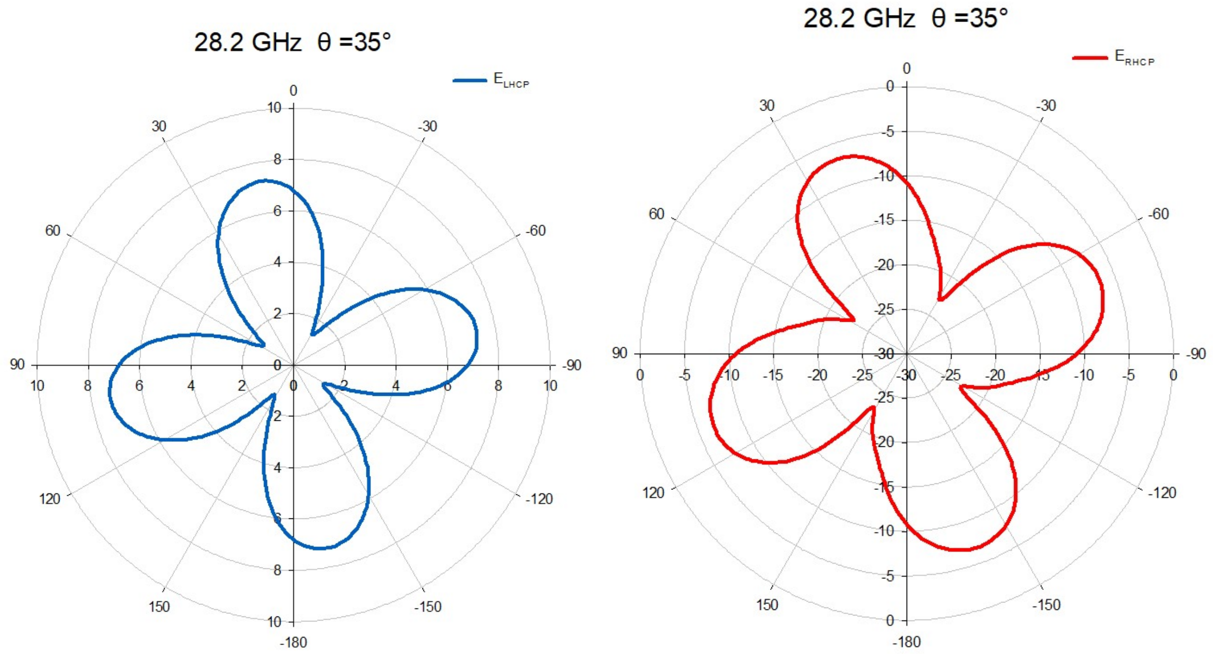

(a) E_{LHCP} (b) E_{RHCP}

Figure 7.28: Four element MIMO radiation patterns Azimuth angle

To complement the 2D plot of the radiation pattern, Fig. 7.29 illustrates the 3D plot for both cases.

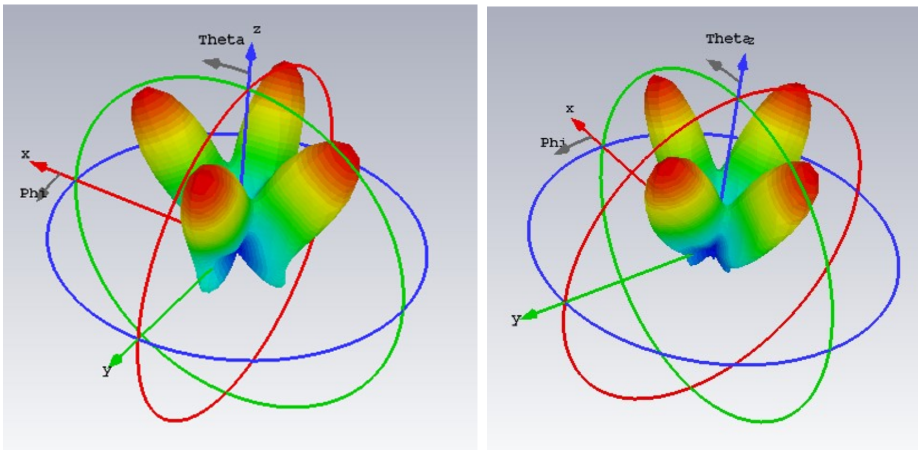

(a) 3D, $1.588\lambda_0$ radiation pattern (b) 3D, $1.775\lambda_0$ radiation pattern

Figure 7.29: 3D MIMO radiation patterns

7.5.3 Antenna gain

Fig. 7.26 illustrates the four radiation maxima direction beams concerning the antenna's overall realized gain. When referring to Fig. 7.26, the existence of four beams directed to ϕ = 7.5 °, ϕ = 99 °, θ = -82 ° and ϕ =-172° can be noted. A maximum realized gain on each demonstrates a 6.21 dBi for the E_{LHCP} field.

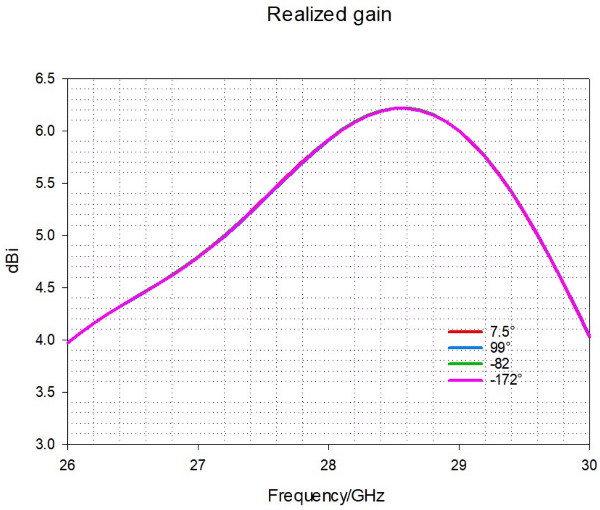

Figure 7.30: Four element antenna realized gain for 1.588λ_0 antenna size

After increasing the antenna size to 1.775λ_0, the four radiated beams experience a shift of approximately 3 ° and an increment of gain to 7.40 dBi. Fig. 7.33 illustrates the overall antenna realized gain which is the same for the four cases.

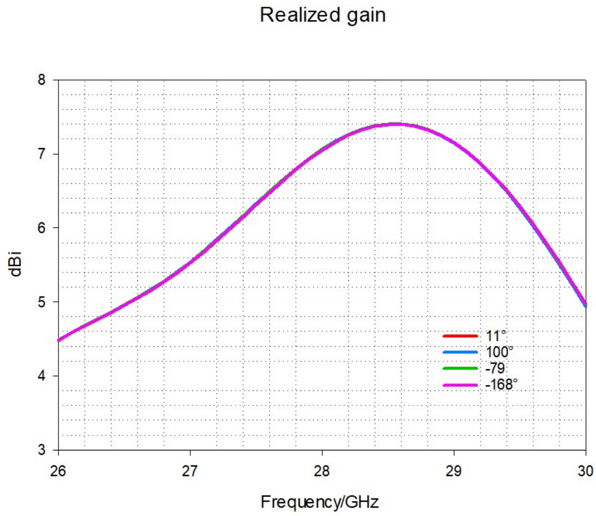

Figure 7.31: Four element antenna realized gain for 1.775λ_0 antenna size

7.5.4 Axial ratio

Axial ratio < 3dB for the case 1.588 λ_0 on each one of the four beams of radiation is illustrated in Fig. 7.32. A 3.58 % axial ratio < 3dB bandwidth is calculated. Compared with the simulated single and two element designs, a 2.75 % and 4.58 % reduction can be observed attributed to the positioning and shifting of RDRA's. It can be noted that there is an overlapping with the impedance bandwidth for both single and double designs.

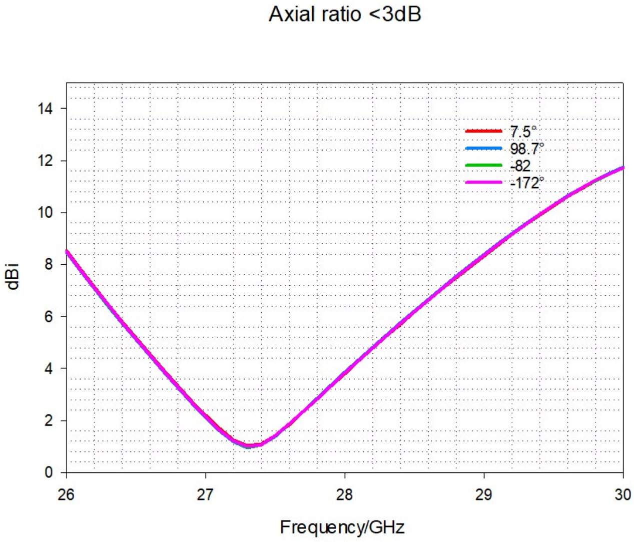

Figure 7.32: Axial ratio < 3dB for 1.588λ_0 antenna size

The 1.775λ_0 antenna design shows an Axial Ratio < 3dB of 4.57 %. In comparison with the single and double antenna elements, there is a 1.76% and 3.59% observed bandwidth difference which behaves similarly to the 1.588 λ_0 MIMO system.

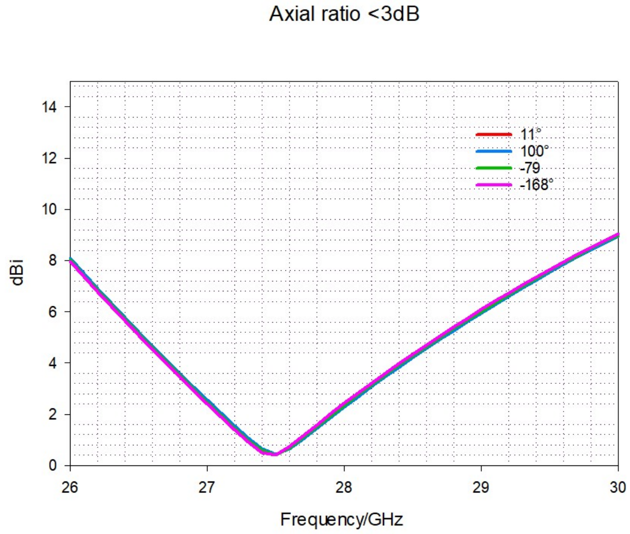

Figure 7.33: Axial ratio < 3dB for 1.775λ_0 antenna size

7.5.5 ECC and DG

Fig. 7.34 demonstrates clear independence between four antenna designs at $1.588\lambda_0$ and $1.775\lambda_0$. When observing the MIMO antenna system at the impedance bandwidth frequency range, the ECC for the 17 mm antenna size shown in Fig. 7.34a value is < 0.00078. On the contrary, the 19 mm antenna size ECC is shown in Fig. 7.34b maximum value is < 0.00028.

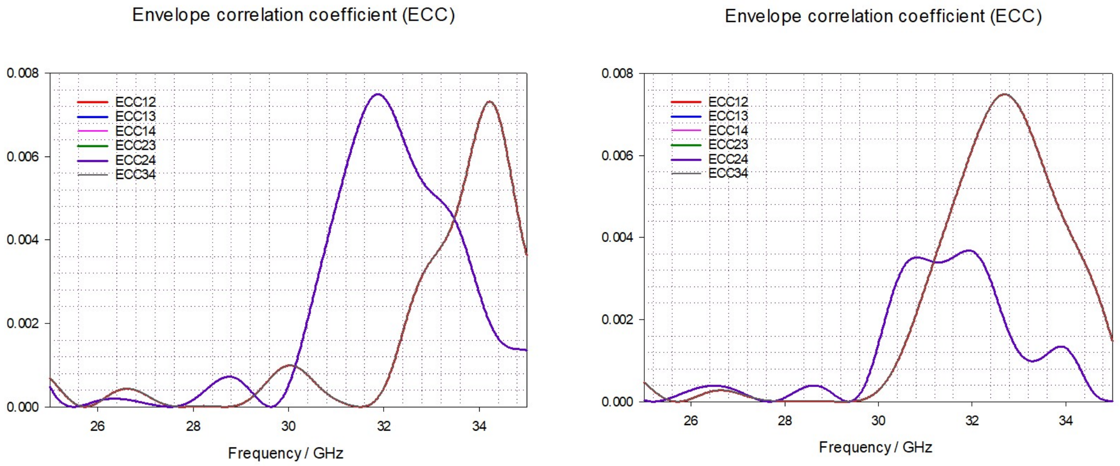

(a) ECC for $1.588\lambda_0$ antenna size

(b) ECC for $1.775\lambda_0$ antenna size

Figure 7.34: Simulated Envelope Correlation Coefficient (ECC)

As a result, Fig. 7.35a and Fig. 7.35b show an almost ideal value of DG. For the first case, an ~ 9.997 DG can be observed. For the second case, a ~ 9.998 DG was calculated. A negligible difference can be observed as an effect of the antenna size. The system is in good agreement with the theoretical thresholds described in Chapter 3.

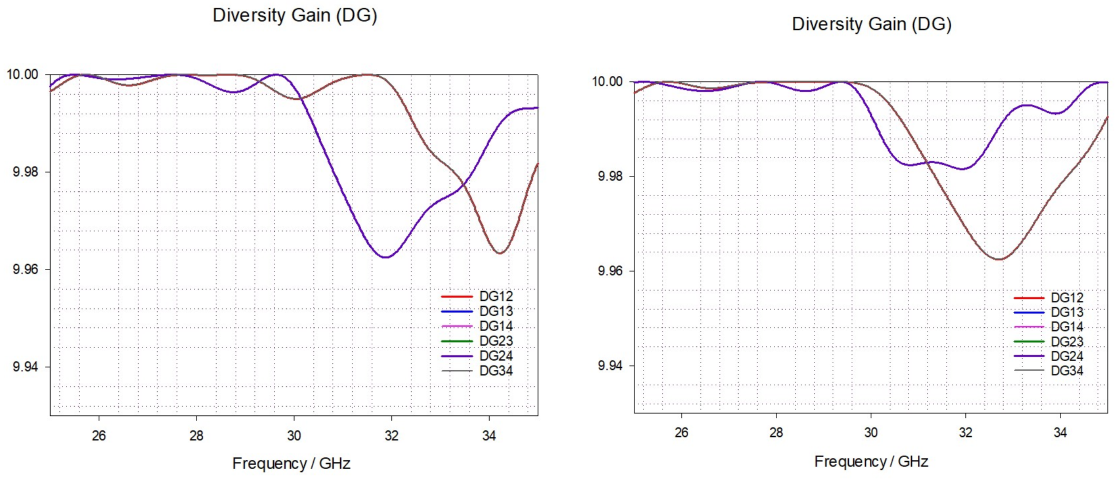

(a) DG for $1.588\lambda_0$

(b) DG for $1.775\lambda_0$

Figure 7.35: Simulated Diversity Gain (DG)

7.6 Conclusions

Firstly, a single element antenna at mmWave with CP was presented. The design offers a measured impedance bandwidth of 8.49 %, and exposes a unidirectional pattern radiating at θ = -30 ° and ϕ = 0 ° with a maximum gain of 5.05 dBi. The second iteration refers to a second MIMO system with two elements from the first case. Both elements were shifted from the middle edge of the board in the left direction to 0.166 λ_0. The distance from the middle to the middle of the radiators is 0.55 λ_0. S_{11} and S_{22} demonstrates an impedance bandwidth of 12.98 % and 13.62 % respectively. The antenna has a radiation pattern oriented to ϕ = 50 ° and ϕ = 130 °. Both maxima show axial ratio < 3 dB of 10.71 %. A 2 GHz shift in the measured results is attributed to the fabricated permittivity of the resonators regarding their manufacturing tolerance. A 500 MHz is expected due to DR positioning and gluing on the PCB. Finally, a four element MIMO system based on the previous chapters iterations was simulated and investigations were conducted. Due to the unsuccessful distancing of > 0.5 λ_0 between antennas for preserving CP and obtaining good antenna performance results, three cases have been presented with dimensions 1.308 λ_0, 1.588 λ_0 and 1.775 λ_0 for analysing its behaviour. The Azimuth angle cut at θ = 37 ° present a four beam maxima at ϕ = 11 °, ϕ = 100 ° , ϕ = -79 ° , ϕ = -168 ° directions. The maximum obtained realized gain for the four cases is 7.40 dBi. Four clear petals can be observed for the three different sizes for the anntena system. The major improvement in results appeared when the antenna size was increased from 14 to 17 mm. It is noticeable that in general when utilising an antenna size > 1.588 λ_0 there is an improvement in S-parameters which in general is less than < -20 dB. Additionally, the CP and realized gain of the original single design is preserved. Some additional mutual coupling reduction techniques are encouraged for adding to the design such as walling each RDRA to preserve the conception of a simple, compact, and optimal performance MIMO design. Similar to the application in Chapter 6, the antenna system described here is suitable for 5G/5GNR wireless modules in on-chip mobile hardware.

Chapter 8

Conclusions and Future Work

8.1 Conclusions

This thesis investigated a few MIMO architectures for various microstrip and RDRA aiming at compact, four beam splitting and low mutual reduction designs. The design methodology consisted of a sequence of iterations from the single antenna element investigation to achieving a compact, cost-effective and multibeam system at the same time preserving antennas high gain, wide impedance bandwidth in addition to circular polarisation. A microstrip loop antenna array design with a high gain, CP radiation capable of a MIMO was first proposed. When implementing the antenna array, an impedance bandwidth of 6.75 % has been achieved with a maximum realized gain of 14.4 dBi with an Axial Ratio $<$ 3 dB bandwidth of 10.16 %. Next, a 4 element MIMO system was considered due to its potential results. The design resulted in an unsuccessful antenna beam splitting for each of the four cases. This is attributed to the mutual coupling between the perpendicular and parallel positioning of the sub-arrays, meaning that the interport reflection coefficient was either increased or equivalent to the initial considerations of the system design. At this point, the strong coupling within each adjacent element on the system was observed on the two antenna layers, making it difficult to reduce with simple techniques such as antenna positioning. Due to the total width of the antenna array, the distance between the sub-arrays was bigger than $0.5\lambda_0$ by design which limited the antenna size reduction and the targeted splitting of the radiation pattern of the adjacent arrays. Moreover, the presence of CP ceased due to presence of strong coupling of elements. Some mutual coupling reduction techniques were applied such as the addition of square, circular slot etching on top of the substrate, and meandered lines, were utilised to reduce the mutual coupling unsuccessfully. Due to the unsuccessful results regarding the strong mutual coupling for the microstrip antenna array, a simpler design was proposed. This is looking to achieve an antenna with similar characteristics for achieving the same objectives. The fifth chapter explores a proof of concept RDRA antenna at the

C-band spectrum. These are for investigating the potential effect of the antenna positioning in addition to isolation techniques for a 5 GHz design. A single RDRA antenna resulted in 5.45 % impedance bandwidth, Axial ratio $<$ 3 dB of 26.05 % with a realized gain of 7.03 dBi. CP and impedance bandwidths presented an overlapping. Consequently, the four element MIMO system was designed and measured with a common GP. It was found that each antenna radiation beam was controlled with the positioning of each element of the design on the PCB, giving four radiation directions at ϕ = -33 °, ϕ = -124 °, ϕ = 55 ° and ϕ = 146 °. Additionally, CP was preserved, and scattering parameters S_{12}, S_{13}, S_{14}, S_{23}, S_{24}, S_{34} $<$ -20 dB were obtained. The maximum antenna gain was preserved on the four radiation points. A mutual coupling reduction of a maximum 27 dB was presented with slot etching on the MIMO GP. ECC and DG are in range according to the literature. Some important considerations regarding manufacturing were presented as potential factors for influencing agreement between simulations and measurements when comparing the designs. The design accomplished simplicity, performance preservation, and mutual coupling reduction. After proofing the potential of RDRA for MIMO systems at C-band, the antennas were considered next for mmWave for being investigated for the case of LP and next for CP. The next chapter considers an initial design of a RDRA antenna working at mmWave at a resonant frequency of 28 GHz. The antenna impedance bandwidth is 6 %, with a maximum realized gain of 7.07 dBi with LP. Next, the 4 MIMO was investigated presenting 4 beam radiation direction as studied in Chapter 3 at ϕ = 15 °, ϕ = 90 °, ϕ = -75 °, ϕ = -173 ° with a similar beam control behaviour as the C-band design. At this point, it is interesting to mention that the 4 beam splitting of the system happened naturally when moving to frequencies bigger than 28 GHz which at the same time affected the potential results of lower frequencies. The maximum antenna gain was preserved on the four radiation points. The design contemplated LP and a slot aperture feeding technique for preserving good efficiency on the design. The maximum mutual coupling reduction for this case was -14 dB with a higher perpendicular reduction due to the proximity of the antennas. ECC and DG are in range according to literature. Manufacturing and assembling tolerances are crucial for these frequencies and antennas. It is suggested to have a meticulous register of the tolerances on fabrication and assembling of the antenna parts, adding an ink/silkscreen on top of the resonator position, and avoid soldering in the connectors due to skin effect for optimal results. Due to the results obtained with the LP antenna, a novel RDRA design with CP was proposed. A similar rhombus radiator shape, to the one utilised in Chapter 7, was implemented for the slot aperture RDRA. The direction of the longer rhombus side will determine the dominant radiation pattern polarisation direction and consider the reflection of the GP. The single antenna element presented an 8.49 % impedance bandwidth with an axial ratio $<$ 3 dB of overlapped bandwidth 10.71 % with a maximum gain of 7 dBi. The two MIMO element design was considered for fabrication instead. The design demonstrated a natural beam splitting at ϕ = 60 ° and ϕ = -150 ° directions preserving the CP for each antenna. The antenna measured Scattering parameters are below < -20 dB within the frequency range. An important consideration is the antenna resonant frequency shift which is attributed to the assembly tolerances of the antenna components. ECC and DG are in range according to literature. Next, the 4 MIMO system was simulated to demonstrate the behaviour of the 4 CP antennas working simultaneously. The antenna size plays a key role in preserving the CP and maintaining the maximum realized gain for each component. Some mutual coupling reduction techniques were applied in addition to the components locating, for example, meandered lines, slot etching lines, and discontinuous lines unsuccessfully.

Table 8.1: Comparative table of the measured MIMO outlined designs

Design	Impedance BW	Gain	Polarisation	Size	Beam splitting	Max isolation
Chpt 4	6.75 %	13.7 dBi	Circular	20.54 mm^2	Unidirectional	N/A
Chpt 5	$\sim$ 7%	$\sim$ 7 dBi	Circular	123.50 mm^2	Four beam	20 dB
Chpt 6	$\sim$ 5 %	7 dBi	Linear	16.20 mm^2	Four beam	6 dB
Chpt 7	12.98 %	6.20 dBi	Circular	14 mm^2	Two beam	12 dB

From Table 8.1, it can be observed that the 4 proposed systems consist of a common, 4 element ground plane systems exhibiting an overall size smaller than $2\lambda_0$ fulfilling at the same time MIMO requirements as ECC and DG. Moreover, the presented antenna systems were achieved with high gain, circular polarisation and wide impedance bandwidth for the case of microstrip and rectangular dielectric resonator antennas at C-band and mmWave spectrums. In addition, a favourable beam splitting resulted from the combination of the mutual coupling reduction techniques such as spacing and antenna element positioning when adding from two element in the system. This novel feature results in a cost effective beam former solution for wireless communication links where a localised area scanning is needed, for example 5G mobile (User Equipments), body communications at human skin level scenarios. Conversely, a significant challenge remains for the presented mmWave RDRA antenna systems in maximizing antenna performance exploring alternative materials for the antenna radiator for both single and full-system configurations without the use of alternative techniques such as metamaterials or walls around each antenna component which eventually will make the design more complex in architecture and size.

8.2 Future Work

After evaluating the strengths and weaknesses of the 4 types of designs, each case has potential future work.

For the microstrip antenna array design, alternative summing networks are suggested to be explored to reduce the overall width of the single antenna design for preserving high gain. Also, a double sided investigation for slot etching and mechanical fit techniques for improving the MIMO prototype performance. A two-layer 2-D walling on each design is suggested firstly with simple slot etching techniques moving to more sophisticated patterns such as meandered lines, electromagnetic coupled shapes. In the case of the presented RDRA systems at mmWave frequencies, alternative reduction techniques are proposed to be explored as 2-D walling for preserving the circular polarisation for four elements. It is suggested to investigate several ceramic resonator shapes for the DRAs with the proposed slot etching and spacing techniques. Additionally, 3-D printing result as another investigation route in aras of preserving precision and proposing superlayers for enhancing antenna gain. Moreover, exploring a massive MIMO architecture with the proposed designs for these radiators sounds sensible for further investigation.

Bibliography

[1] S. Dahmen-Lhuissier, “5G,” 2024. https://www.etsi.org/technologies/5g?tmpl=component [Accessed: (15th January 2024)],.

[2] J. D. Preez and S. Sinha, *Millimeter-wave antennas: Configurations and applications.* Springer, 2016.

[3] *IEEE Std 521-1976 : IEEE Standard Letter Designations for Radar-Frequency Bands.* Piscataway, NJ, USA: IEEE, 1976.

[4] J. C. Wiltse, “History of millimeter and submillimeter waves,” *IEEE Transactions on microwave theory and techniques*, vol. 32, no. 9, pp. 1118–1127, 1984.

[5] M. A. Jensen, “A history of mimo wireless communications,” in *2016 IEEE International Symposium on Antennas and Propagation (APSURSI)*, pp. 681–682, 2016.

[6] G. J. Foschini, “Layered space-time architecture for wireless communication in a fading environment when using multi-element antennas,” *Bell Labs Technical Journal*, vol. 1, no. 2, pp. 41–59, 1996.

[7] G. Raleigh and J. Cioffi, “Spatio-temporal coding for wireless communications,” in *Proceedings of GLOBECOM’96. 1996 IEEE Global Telecommunications Conference*, vol. 3, pp. 1809–1814 vol.3, 1996.

[8] S. Alouini, “A simple transmitter diversity scheme for wireless communications,” *IEEE Journal on Selected Areas in Communications*, pp. 1451–1458, 1998.

[9] I. Ishteyaq and K. Muzaffar, “Multiple input multiple output (mimo) and fifth generation (5g): an indispensable technology for sub-6 ghz and millimeter wave future generation mobile terminal applications,” *International Journal of Microwave and Wireless Technologies*, vol. 14, no. 7, p. 932–948, 2022.

[10] R. Chataut and R. Akl, “Massive mimo systems for 5g and beyond networks—overview, recent trends, challenges, and future research direction,” *Sensors*, vol. 20, no. 10, p. 2753, 2020.

[11] T. Raj, R. Mishra, P. Kumar, and A. Kapoor, “Advances in mimo antenna design for 5g: A comprehensive review,” *Sensors*, vol. 23, no. 14, 2023.

[12] A. Gupta, M. Kumari, M. Sharma, M. H. Alsharif, P. Uthansakul, M. Uthansakul, and S. Bansal, “8-port mimo antenna at 27 ghz for n261 band and exploring for body centric communication,” *PLOS ONE*, vol. 19, pp. 1–20, 06 2024.

[13] C. A. Hofmann, R. T. Schwarz, and A. Knopp, “Multisatellite uhf mimo channel measurements,” *IEEE Antennas and Wireless Propagation Letters*, vol. 16, pp. 2481–2484, 2017.

[14] P. Tiwari, V. Gahlaut, M. Kaushik, P. Rani, A. Shastri, and B. Singh, “Advancing 5G connectivity: A comprehensive review of MIMO antennas for 5G applications,” *Int. J. Antennas Propag.*, vol. 2023, pp. 1–19, Aug. 2023.

[15] T. D. Emil Björnson, *Introduction to Multiple Antenna Communications and Reconfigurable Surfaces.* Boston-Delft: now publishers, 2024.

[16] Q. Spencer, C. Peel, A. Swindlehurst, and M. Haardt, “An introduction to the multiuser mimo downlink,” *IEEE Communications Magazine*, vol. 42, no. 10, pp. 60–67, 2004.

[17] J. Korhonen, *Introduction to 4G Mobile Communications.* Artech House mobile communications series, Artech House, 2014.

[18] N.-N. Dao, N. H. Tu, T.-D. Hoang, T.-H. Nguyen, L. V. Nguyen, K. Lee, L. Park, W. Na, and S. Cho, “A review on new technologies in 3gpp standards for 5g access and beyond,” *Computer Networks*, vol. 245, p. 110370, 2024.

[19] H. J. Visser, “Array and phased array antenna basics,” 2005.

[20] B. Toh, R. Cahill, and V. Fusco, “Understanding and measuring circular polarization,” *IEEE Transactions on Education*, vol. 46, no. 3, pp. 313–318, 2003.

[21] W. L. Stutzman and G. A. Thiele, *Antenna theory and design.* John Wiley ‘I&’ Sons, 1998.

[22] R.-L. Li, V. Fusco, and H. Nakano, “Circularly polarized open-loop antenna,” *IEEE Transactions on Antennas and Propagation*, vol. 51, no. 9, pp. 2475–2477, 2003.

[23] R. Johnson and H. Jasik, *Antenna Engineering Handbook.* Electronics Electrical Engineering, McGraw-Hill, 1993.

[24] H. Nakano, “C-figured loop antennas,” *Electronics Letters*, vol. 31, pp. 693–694(1), April 1995.

[25] A. Petosa, *Dielectric Resonator Antenna Handbook.* USA: Artech House, Inc., 2007.

[26] M. McAllister, S. A. Long, and G. Conway, “Rectangular dielectric resonator antenna,” *Electronics letters*, vol. 19, p. 218, 1983.

[27] S. Long, M. McAllister, and L. Shen, “The resonant cylindrical dielectric cavity antenna,” *IEEE Transactions on Antennas and Propagation*, vol. 31, no. 3, pp. 406–412, 1983.

[28] P. J. R. James, *Dielectric Resonator Antennas.* Research Studies Press Ltd., 2003.

[29] A. A. Abdulmajid, S. Khamas, and S. Zhang, “Wide bandwidth high gain circularly polarized millimetre-wave rectangular dielectric resonator antenna,” *Progress In Electromagnetics Research M*, vol. 89, pp. 171–177, 2020.

[30] A. A. Abdulmajid, Y. Khalil, and S. Khamas, “Higher-order-mode circularly polarized two-layer rectangular dielectric resonator antenna,” *IEEE Antennas and Wireless Propagation Letters*, vol. 17, no. 6, pp. 1114–1117, 2018.

[31] R. Kumar Mongia and A. Ittipiboon, “Theoretical and experimental investigations on rectangular dielectric resonator antennas,” *IEEE Transactions on Antennas and Propagation*, vol. 45, no. 9, pp. 1348–1356, 1997.

[32] G. Junker, A. Kishk, and A. Glisson, “Input impedance of dielectric resonator antennas excited by a coaxial probe,” *IEEE Transactions on Antennas and Propagation*, vol. 42, no. 7, pp. 960–966, 1994.

[33] M. S. Ibrahim, H. Attia, Q. Cheng, and A. Mahmoud, “Wideband circularly polarized aperture coupled dra array with sequential-phase feed at x-band,” *Alexandria Engineering Journal*, vol. 59, no. 6, pp. 4901–4908, 2020.

[34] S. Mohapatra, T. Badapanda, and S. N. Tripathy, “An investigation of microwave dielectric properties of bazr0. 25ti0. 75o3 and performance of dra for 5g application,” *Journal of Materials Science: Materials in Electronics*, vol. 35, no. 2, pp. 1–12, 2024.

[35] M. Suma, S. K. Menon, P. Bijumon, M. Sebastian, and P. Mohanan, “Rectangular dielectric resonator antenna on a conductor-backed co-planar waveguide,” *Microwave and Optical Technology Letters*, vol. 45, no. 2, pp. 154–156, 2005.

[36] T. Kumari, K. K. Suman, R. K. Gangwar, and R. K. Chaudhary, “An anisotropic prs for squinting the radiation pattern with gain improvement of mimo system,” *AEU - International Journal of Electronics and Communications*, vol. 176, p. 155150, 2024.

[37] A. Gaya, M. H. Jamaluddin, M. R. Kamarudin, R. Selvaraju, and I. Ali, “Performance analysis of a dielectric resonator antenna with different feeding technique for 5g communication,” in *2018 2nd International Conference on Electrical Engineering and Informatics (ICon EEI)*, pp. 92–97, 2018.

[38] K.-W. Leung, K.-M. Luk, K. Lai, and D. Lin, “Theory and experiment of an aperture-coupled hemispherical dielectric resonator antenna,” *IEEE Transactions on Antennas and Propagation*, vol. 43, no. 11, pp. 1192–1198, 1995.

[39] C. Kong, “A general maximum power transfer theorem,” *IEEE Transactions on Education*, vol. 38, no. 3, pp. 296–298, 1995.

[40] *MIMO-Based 5G FR1 Band Mobile Antenna*, ch. 5, pp. 125–165. John Wiley & Sons, Ltd, 2022.

[41] X. Chen, S. Zhang, and Q. Li, “A review of mutual coupling in mimo systems,” *IEEE Access*, vol. 6, pp. 24706–24719, 2018.

[42] M. T. Y.C., G. H. N.G., and R. T. Y.S., “A 2-by-2 sub-array for scalable 28ghz mmwave phased array horn antenna in 5g network,” in *2019 13th European Conference on Antennas and Propagation (EuCAP)*, pp. 1–5, 2019.

[43] Q. Zhu, K.-B. Ng, and C. H. Chan, “Printed circularly polarized spiral antenna array for millimeter-wave applications,” *IEEE Transactions on Antennas and Propagation*, vol. 65, no. 2, pp. 636–643, 2017.

[44] O. Kramer, T. Djerafi, and K. Wu, “Very small footprint 60 ghz stacked yagi antenna array,” *IEEE Transactions on Antennas and Propagation*, vol. 59, no. 9, pp. 3204–3210, 2011.

[45] W.-C. Hsiao, H.-S. Huang, C.-Y. Ho, S.-C. Hsieh, and C.-C. Wang, “A 2x2 broadband dual-polarized antenna array using aip techniques for 5g mmwave beamforming systems,” in *2022 17th International Microsystems, Packaging, Assembly and Circuits Technology Conference (IMPACT)*, pp. 1–4, 2022.

[46] X. Jiang, Z. Zhang, Y. Li, and Z. Feng, “A low-cost wideband circularly polarized slot array with integrated feeding network and reduced height,” *IEEE Antennas and Wireless Propagation Letters*, vol. 15, pp. 222–225, 2016.

[47] K. L. Chung, Y. Li, and C. Zhang, “Broadband artistic antenna array composed of circularly-polarized wang-shaped patch elements,” *AEU - International Journal of Electronics and Communications*, vol. 74, pp. 116–122, 2017.

[48] A. Siahcheshm, J. Nourinia, C. Ghobadi, M. Karamirad, and B. Mohammadi, “A broadband circularly polarized cavity-backed archimedean spiral array antenna for c-band applications,” *AEU - International Journal of Electronics and Communications*, vol. 81, pp. 218–226, 2017.

[49] Z. Muludi and B. Aswoyo, “Truncated microstrip square patch array antenna 2 × 2 elements with circular polarization for s-band microwave frequency,” in *2017 International Electronics Symposium on Engineering Technology and Applications (IES-ETA)*, pp. 87–92, 2017.

[50] G. A. Sarkar, S. Ballav, A. Chatterjee, S. Ranjit, and S. K. Parui, “Four element mimo dra with high isolation for wlan applications,” *Progress In Electromagnetics Research Letters*, vol. 84, pp. 99–106, 2019.

[51] G. Varshney, S. Gotra, S. Chaturvedi, V. S. Pandey, and R. S. Yaduvanshi, “Compact four-port mimo dielectric resonator antenna with pattern diversity,” *IET Microwaves, Antennas & Propagation*, vol. 13, no. 12, pp. 2193–2198, 2019.

[52] M. Mishra, S. Chaudhuri, and R. S. Kshetrimayum, “Four-port dra array for mimo applications,” in *2020 International Symposium on Antennas and Propagation (ISAP)*, pp. 765–766, IEEE, 2021.

[53] N. K. Sahu, G. Das, R. K. Gangwar, and K. Rambabu, “An arrangement for four-element mimo dra with complementary cp diversity,” *IEEE Antennas and Wireless Propagation Letters*, vol. 20, no. 9, pp. 1616–1620, 2021.

[54] M. Belazzoug, I. Messaoudene, S. Aidel, M. Nedil, and A. A. Kishk, “Ultra-compact 4-port dr antenna for multi-input multi-output standards,” *International Journal of RF and Microwave Computer-Aided Engineering*, vol. 30, no. 5, p. e22145, 2020.

[55] N. K. Sahu and R. K. Gangwar, “Mimo-dra with triple-band cp & low em coupling: a methodical design approach,” *Waves in Random and Complex Media*, vol. 0, no. 0, pp. 1–16, 2023.

[56] G. Das, N. K. Sahu, A. Sharma, R. K. Gangwar, and M. S. Sharawi, “Dielectric resonator-based four-element eight-port mimo antenna with multi-directional pattern diversity,” *IET Microwaves, Antennas & Propagation*, vol. 13, no. 1, pp. 16–22, 2019.

[57] P. Kumar, G. S. Sharma, and A. Gupta, “Four-port cylindrical dra based mimo antenna for wlan application,” in *2022 International Conference on Intelligent Innovations in Engineering and Technology (ICIIET)*, pp. 33–37, IEEE, 2022.

[58] V. Kumar, “Rectangular dr-based dual-band cp-mimo antenna with inverted z-shaped slot,” *International Journal of Electronics*, vol. 107, no. 10, pp. 1559–1573, 2020.

[59] A. K. Dwivedi, A. Sharma, A. K. Singh, and V. Singh, “Quad-port ring dielectric resonator based mimo radiator with polarization and space diversity,” *Microwave and Optical Technology Letters*, vol. 62, no. 6, pp. 2316–2327, 2020.

[60] A. A. Ibrahim, H. Zahra, S. M. Abbas, M. I. Ahmed, G. Varshney, S. Mukhopadhyay, and A. Mahmoud, “Compact four-port circularly polarized mimo x-band dra,” *Sensors*, vol. 22, no. 12, p. 4461, 2022.

[61] A. Iqbal, J. Nasir, M. B. Qureshi, A. A. Khan, J. U. Rehman, Owais, H. U. Rahman, M. A. Fayyaz, and R. Nawaz, “A cpw fed quad-port mimo dra for sub-6 ghz 5g applications,” *Plos one*, vol. 17, no. 6, p. e0268867, 2022.

[62] Q. X. Lai, Y. M. Pan, and S. Y. Zheng, “A self-decoupling method for mimo linear and planar dielectric resonator antenna arrays based on transmission characteristics of feeding structure,” *IEEE Transactions on Antennas and Propagation*, vol. 71, no. 7, pp. 5708–5716, 2023.

[63] P. R. Girjashankar, T. Upadhyaya, and A. Desai, “Multiband hybrid mimo dra for sub-6 ghz 5g and wifi-6 applications,” *International Journal of RF and Microwave Computer-Aided Engineering*, vol. 32, no. 12, p. e23479, 2022.

[64] A. K. Dwivedi, A. Sharma, A. K. Singh, and V. Singh, “Design of dual band four port circularly polarized mimo dra for wlan/wimax applications,” *Journal of Electromagnetic Waves and Applications*, vol. 34, no. 15, pp. 1990–2009, 2020.

[65] A. K. Dwivedi, A. Sharma, A. K. Singh, and V. Singh, “Circularly polarized two port mimo cylindrical dra for 5g applications,” in *2020 international conference on UK-China emerging technologies (UCET)*, pp. 1–4, IEEE, 2020.

[66] J. Albuquerque, “Satellite operators challenge mobiles’ use of C-band,” 2024. https://www.itu.int/itunews/manager/display.asp?lang=en&year=2007&issue=08&ipage=C-band [Accessed: (23th June 2024)],.

[67] P. R. Girjashankar and T. Upadhyaya, “Substrate integrated waveguide fed dual band quad-elements rectangular dielectric resonator mimo antenna for millimeter wave 5g

wireless communication systems," *AEU-international Journal of Electronics and Communications*, vol. 137, p. 153821, 2021.

[68] A. Sharma, J. K. Rai, H. Katiyar, *et al.*, "Design of a high gain mimo dielectric resonator antenna for 5g mm-wave applications," in *2023 International Conference on IoT, Communication and Automation Technology (ICICAT)*, pp. 1–5, IEEE, 2023.

[69] A. Sharma, A. Sarkar, A. Biswas, and M. J. Akhtar, "Millimeter-wave quad-port multiple-input multiple-output dielectric resonator antenna excited differentially by te 20 mode substrate integrated waveguide," in *2019 URSI Asia-Pacific Radio Science Conference (AP-RASC)*, pp. 1–4, IEEE, 2019.

[70] S. K. K. Dash, Q. S. Cheng, T. Khan, M. V. Yadav, and L. Wang, "5g millimeter-wave mimo dras with reduced mutual coupling," *Microwave and Optical Technology Letters*, vol. 66, no. 1, p. e33982, 2024.

[71] D. Sharma, R. Katiyar, A. K. Dwivedi, K. Nagesh, A. Sharma, and P. Ranjan, "Dielectric resonator-based two-port filtennas with pattern and space diversity for 5g iot applications," *International Journal of Microwave and Wireless Technologies*, vol. 15, no. 2, pp. 263–270, 2023.

[72] A. Dadgarpour, B. Zarghooni, B. S. Virdee, T. A. Denidni, and A. A. Kishk, "Mutual coupling reduction in dielectric resonator antennas using metasurface shield for 60-ghz mimo systems," *IEEE Antennas and Wireless Propagation Letters*, vol. 16, pp. 477–480, 2016.

[73] R. Karimian, A. Kesavan, M. Nedil, and T. A. Denidni, "Low-mutual-coupling 60-ghz mimo antenna system with frequency selective surface wall," *IEEE Antennas and Wireless Propagation Letters*, vol. 16, pp. 373–376, 2016.

[74] A. Muhammad, M. U. Khan, R. S. Malfajani, M. S. Sharawi, and M. Alathbah, "An integrated dra-based large frequency ratio antenna system consisting of a mm-wave array and a mimo antenna for 5g applications," *IEEE Open Journal of Antennas and Propagation*, 2024.

[75] M. T. Hussain, M. S. Sharawi, S. Podilchack, and Y. M. M. Antar, "Closely packed millimeter-wave mimo antenna arrays with dielectric resonator elements," in *2016 10th European Conference on Antennas and Propagation (EuCAP)*, pp. 1–4, 2016.

[76] Y. M. Pan, X. Qin, Y. X. Sun, and S. Y. Zheng, "A simple decoupling method for 5g millimeter-wave mimo dielectric resonator antennas," *IEEE Transactions on Antennas and Propagation*, vol. 67, no. 4, pp. 2224–2234, 2019.

[77] Y. Zhang, J.-Y. Deng, M.-J. Li, D. Sun, and L.-X. Guo, "A mimo dielectric resonator antenna with improved isolation for 5g mm-wave applications," *IEEE Antennas and Wireless Propagation Letters*, vol. 18, no. 4, pp. 747–751, 2019.

[78] N. Murthy, "Improved isolation metamaterial inspired mm-wave mimo dielectric resonator antenna for 5g application," *Progress In Electromagnetics Research C*, vol. 100, pp. 247–261, 2020.

[79] A. Sharma, A. Sarkar, A. Biswas, and M. J. Akhtar, "Millimeter-wave quad-port multiple-input multiple-output dielectric resonator antenna excited differentially by te20 mode substrate integrated waveguide," in *2019 URSI Asia-Pacific Radio Science Conference (AP-RASC)*, pp. 1–4, 2019.

[80] M. Xu and J. Zhang, "Circularly polarized multiple-input multiple-output dielectric resonator antenna for meter-wave application," *Electronics*, vol. 12, no. 20, p. 4258, 2023.

[81] H. A. Malhat, S. H. Zainud-Deen, H. El-Hemaily, H. A. Hamed, and A. A. AIbrahim, "Reconfigurable circularly polarized hemispherical dra using plasmonic graphene strips for mimo communications," *Plasmonics*, pp. 1–10, 2022.

[82] H. Ahmad, M. H. Jamaluddin, F. C. Seman, and M. Rahman, "Mimo dielectric resonator antennas for 5g applications: A review," *Electronics*, vol. 12, no. 16, p. 3469, 2023.

[83] R. H. Elabd and A. J. A. Al-Gburi, "Super-compact 28/38 ghz 4-port mimo antenna using metamaterial-inspired ebg structure with sar analysis for 5g cellular devices," *Journal of Infrared, Millimeter, and Terahertz Waves*, vol. 45, no. 1, pp. 35–65, 2024.

[84] A. Iqbal, A. Basir, A. Smida, N. K. Mallat, I. Elfergani, J. Rodriguez, and S. Kim, "Electromagnetic bandgap backed millimeter-wave mimo antenna for wearable applications," *IEEE Access*, vol. 7, pp. 111135–111144, 2019.

[85] M. J. Al-Hasan, T. A. Denidni, and A. R. Sebak, "Millimeter-wave compact ebg structure for mutual coupling reduction applications," *IEEE Transactions on Antennas and Propagation*, vol. 63, no. 2, pp. 823–828, 2015.

[86] C. Ma, S. Y. Zheng, Y. M. Pan, and Z. Chen, "Millimeter-wave fully integrated dielectric resonator antenna and its multi-beam application," *IEEE Transactions on Antennas and Propagation*, vol. 70, no. 8, pp. 6571–6580, 2022.

[87] B. Ali Esmail and S. Koziel, “High isolation metamaterial-based dual-band mimo antenna for 5g millimeter-wave applications,” *AEU - International Journal of Electronics and Communications*, vol. 158, p. 154470, 2023.

[88] S. S. Al-Bawri, M. T. Islam, T. Shabbir, G. Muhammad, M. S. Islam, and H. Y. Wong, “Hexagonal shaped near zero index (nzi) metamaterial based mimo antenna for millimeter-wave application,” *IEEE Access*, vol. 8, pp. 181003–181013, 2020.

[89] M. Farahani, J. Pourahmadazar, M. Akbari, M. Nedil, A. R. Sebak, and T. A. Denidni, “Mutual coupling reduction in millimeter-wave mimo antenna array using a metamaterial polarization-rotator wall,” *IEEE Antennas and Wireless Propagation Letters*, vol. 16, pp. 2324–2327, 2017.

[90] S. Tariq, S. I. Naqvi, N. Hussain, and Y. Amin, “A metasurface-based mimo antenna for 5g millimeter-wave applications,” *IEEE Access*, vol. 9, pp. 51805–51817, 2021.

[91] T. N. Cao, M. T. Nguyen, H. L. Phan, D. D. Nguyen, D. L. Vu, T. Q. H. Nguyen, J.-M. Kim, *et al.*, “Millimeter-wave broadband mimo antenna using metasurfaces for 5g cellular networks,” *International Journal of RF and Microwave Computer-Aided Engineering*, vol. 2023, 2023.

[92] I. Ud Din, M. Alibakhshikenari, B. S. Virdee, R. K. R. Jayanthi, S. Ullah, S. Khan, C. H. See, L. Golunski, and S. Koziel, “Frequency-selective surface-based mimo antenna array for 5g millimeter-wave applications,” *Sensors*, vol. 23, no. 15, 2023.

[93] H. A. Mohamed, M. Edries, M. A. Abdelghany, and A. A. Ibrahim, “Millimeter-wave antenna with gain improvement utilizing reflection fss for 5g networks,” *IEEE Access*, vol. 10, pp. 73601–73609, 2022.

[94] N. Khiabani, C.-W. Chiang, N.-C. Liu, P.-Y. Chen, Y.-C. Kuan, and C.-T. M. Wu, “Metamaterial-enabled ultrawideband mmwave antenna-in-package using heterogeneously-integrated silicon ipd and hdi-pcb for b5g/ 6g applications,” *IEEE Journal on Emerging and Selected Topics in Circuits and Systems*, vol. 14, no. 1, pp. 7–18, 2024.

[95] A. Kesavan, M. Mantash, J. Zaid, and T. A. Denidni, “A dual-plane beam-sweeping millimeter-wave antenna using reconfigurable frequency selective surfaces,” *IEEE Antennas and Wireless Propagation Letters*, vol. 17, no. 10, pp. 1832–1836, 2018.

[96] S. Luo, Y. Zhang, P. Mei, G. F. Pedersen, and S. Zhang, “Decoupling for millimeter-wave array antennas using near-field shrinking dielectric superstrate,” *IEEE Open Journal of Antennas and Propagation*, vol. 4, pp. 1187–1194, 2023.

[97] M. Li and S. Cheung, “Isolation enhancement for mimo dielectric resonator antennas using dielectric superstrate,” *IEEE Transactions on Antennas and Propagation*, vol. 69, no. 7, pp. 4154–4159, 2021.

[98] B. Bahreini, H. Oraizi, N. Noori, and P. Mousavi, “Optimum design of a beam-forming array of s-shaped dra elements with a superstrate on an siw feed for 5g mobile systems,” *IEEE Antennas and Wireless Propagation Letters*, vol. 18, no. 7, pp. 1410–1414, 2019.

[99] J. Iqbal, U. Illahi, M. I. Sulaiman, M. M. Alam, M. M. Su’ud, and M. N. M. Yasin, “Mutual coupling reduction using hybrid technique in wideband circularly polarized mimo antenna for wimax applications,” *IEEE Access*, vol. 7, pp. 40951–40958, 2019.

[100] M. T. Abhimanyu Yadav, Deepak Sigroha and A. Sharma, “Quad-portmimo dielectric resonatorantenna with filtering response for iot application,” *Electromagnetics*, vol. 44, no. 1, pp. 32–45, 2024.

[101] Y. Zhang, J.-Y. Deng, M.-J. Li, D. Sun, and L.-X. Guo, “A mimo dielectric resonator antenna with improved isolation for 5g mm-wave applications,” *IEEE Antennas and Wireless Propagation Letters*, vol. 18, no. 4, pp. 747–751, 2019.

[102] P. K. Shukla, Sikandar, V. S. Tripathi, and A. Sharma, “Dual band circularly polarized partially reflecting surface-loaded dielectric resonator-based mimo antenna for mm-wave 5g applications,” *International Journal of Microwave and Wireless Technologies*, p. 1–10, 2024.

[103] Vishwanath, R. Babu, V. Sharma, B. C. Sahana, and G. Varshney, “Controlling the resonant modes/bandwidth using graphene strip and isolation enhancement in a two-port thz mimo dra,” *Optical and Quantum Electronics*, vol. 55, no. 7, p. 659, 2023.

[104] Y.-T. Liu and K. W. Leung, “28 ghz substrate-integrated filtering dielectric resonator antenna array,” *IEEE Transactions on Antennas and Propagation*, vol. 70, no. 10, pp. 9900–9905, 2022.

[105] M. Khalid, S. Iffat Naqvi, N. Hussain, M. Rahman, Fawad, S. S. Mirjavadi, M. J. Khan, and Y. Amin, “4-port mimo antenna with defected ground structure for 5g millimeter wave applications,” *Electronics*, vol. 9, no. 1, 2020.

[106] M. E. Munir, M. M. Nasralla, and M. A. Esmail, “Four port tri-circular ring mimo antenna with wide-band characteristics for future 5g and mmwave applications,” *Heliyon*, vol. 10, no. 8, 2024.

[107] A. D. Nesic and D. A. Nesic, “Printed planar 8 × 8 array antenna with circular polarization for millimeter-wave application,” *IEEE Antennas and Wireless Propagation Letters*, vol. 11, pp. 744–747, 2012.

[108] L. Fang and R. Henderson, “Broadband conductor-backed coplanar waveguide to double-sided parallel strip line transition at millimeter wave,” in *2017 Texas Symposium on Wireless and Microwave Circuits and Systems (WMCS)*, pp. 1–4, IEEE, 2017.

[109] H. Wheeler, “Transmission-line properties of parallel strips separated by a dielectric sheet,” *IEEE Transactions on Microwave Theory and Techniques*, vol. 13, no. 2, pp. 172–185, 1965.

[110] V. Rodriguez, “Comparing predicted performance of anechoic chambers to free space vswr measurements,” in *2017 Antenna Measurement Techniques Association Symposium (AMTA)*, pp. 1–6, IEEE, 2017.

[111] P. Schatz and A. McCaffery, “The faraday effect,” *Quarterly Reviews, Chemical Society*, vol. 23, no. 4, pp. 552–584, 1969.

[112] A. Nesic and D. Nesic, “Millimeter wave antenna array with circular polarization,” in *The 40th European Microwave Conference*, pp. 204–207, 2010.

[113] H. Morishita and K. Hirasawa, “Wideband circularly-polarized loop antenna,” *Proceedings of IEEE Antennas and Propagation Society International Symposium and URSI National Radio Science Meeting*, vol. 2, pp. 1286–1289 vol.2, 1994.

[114] M. Alibakhshikenari, B. S. Virdee, H. Benetatos, E. M. Ali, M. Soruri, M. Dalarsson, M. Naser-Moghadasi, C. H. See, A. Pietrenko-Dabrowska, S. Koziel, *et al.*, “An innovative antenna array with high inter element isolation for sub-6 ghz 5g mimo communication systems,” *Scientific Reports*, vol. 12, no. 1, p. 7907, 2022.

[115] S. Hwangbo, H. Y. Yang, and Y.-K. Yoon, “Mutual coupling reduction using micromachined complementary meander-line slots for a patch array antenna,” *IEEE Antennas and Wireless Propagation Letters*, vol. 16, pp. 1667–1670, 2017.

[116] A. Olver, “Millimetrewave systems—past, present and future,” in *IEE Proceedings F (Radar and Signal Processing)*, vol. 136, pp. 35–52, IET, 1989.

[117] Hirose Electric Co. LTD, *2.4mm Coaxial Connectors MIL Standard Compliant*, 2002.

[118] Fairview Microwave, *FMDV1069 Datasheet*, 2020. Rev. 1.

[119] Fairview Microwave, *FMAD1028 Datasheet*, 2020. Rev. 1.6.

[120] M. Moharana and B. Dwivedy, "Circularly polarized planar antennas with enhanced characteristics for contemporary wireless communication use cases: A review," *IEEE Access*, pp. 1–1, 2024.